ABSTRACT

Title of dissertation: GUST ENCOUNTER FLOW PHYSICS WITH APPLICATIONS TO FLOW SENSING AND CONTROL

Antonios Gementzopoulos, Doctor of Philosophy, 2024

Dissertation directed by: Professor Anya Jones
University of Maryland Department of Aerospace Engineering

Systems such as aircraft and wind turbines frequently operate in highly unsteady flow environments and are subject to large flow disturbances, such as gusts. Gust encounters can lead to severe performance degradation and, in extreme cases, catastrophic failure. This dissertation investigates the fundamental flow physics underlying wing-gust encounter aerodynamics and explores strategies for effective flow sensing and gust mitigation. Emphasis is placed on the development and use of inviscid methods to facilitate the detection, prediction, and alleviation of incident gusts.

The first part of the dissertation experimentally investigates the unsteady loads and flowfields produced during transverse gust encounters and evaluates the effectiveness of inviscid aerodynamics theory. In particular, experimental lift transients and shed vorticity distributions are compared with those predicted by Küssner's transverse gust model. The results show that in the early stages of the gust encounter Küssner's inviscid model captures the circulation production of the separated, viscous flow which produces favorable agreement between experimental and theoretical

lift transients. The performance of Küssner's model deteriorates during the wing's exit from the gust due to contrasting shed vorticity distributions between the model and the experiments, resulting in fundamentally different lift reduction mechanisms.

Building on these findings, the dissertation investigates how vorticity in the flow affects the wing's surface pressure distribution during a gust encounter. Simultaneous surface pressure, load, and flow measurements are presented, and their concurrent analysis details the events leading to flow separation and leading-edge vortex (LEV) formation. In particular, surface pressure-derived quantities—such as leading-edge suction and the leading-edge pressure gradient—are examined in their ability to sense key flow structures and detect gusts.

The final part of the dissertation centers on the development and application of inviscid modeling methods to explore the physics of flow separation and to design effective strategies for flow sensing and control. Three key applications are addressed: (1) A numerical inviscid method incorporating the effects of leading-edge separation is developed to compute unsteady surface pressure distributions during gust encounters; (2) an analytical vortex sheet model is introduced, relating the growth of the leading-edge vortex sheet to the pressure coefficient at the leading edge, enabling LEV detection and strength estimation, and (3) Theodorsen's inviscid model is combined with an iterative optimization method developed by collaborators, to experimentally identify optimal gust-mitigating pitch and plunge maneuvers.

GUST ENCOUNTER FLOW PHYSICS WITH APPLICATIONS TO FLOW SENSING AND CONTROL

by

Antonios Gementzopoulos

Dissertation submitted to the Faculty of the Graduate School of the
University of Maryland, College Park in partial fulfillment
of the requirements for the degree of
Doctor of Philosophy
2024

Advisory Committee:
Professor Anya Jones, Chair/Advisor
Professor Kenneth Kiger, Dean's Representative
Professor James Baeder
Professor Robert Sanner
Professor Johan Larsson

Acknowledgments

First and foremost, I would like to express my heartfelt gratitude to my advisor, Dr. Anya Jones. Her exceptional mentorship, unwavering guidance, and steadfast support have been invaluable throughout my PhD journey. Her ability to inspire, challenge, and encourage me has not only shaped my research but also profoundly influenced my growth as an engineer and a thinker. I am also deeply grateful to Dr. Frank Lagor, whose insight and guidance were instrumental in helping me navigate the many research challenges along the way.

I am also deeply thankful to my incredible labmates, past and present, with whom I had the privilege to overlap: Hülya Biler, Jonathan Lefebvre, Alex Goldberg, Assaf Krupnik, Girguis Sedky, and Oliver Wild, along with his wife, Caroline. Each of you brought unique perspectives, and your contributions, both to this work and to my journey, are deeply appreciated. A special thank you goes to Oliver, who joined this journey alongside me–we started and finished together, defending just two days apart. Sharing this milestone with you has been an incredible experience, and I'm so grateful for your friendship and support along the way. I am also deeply thankful to Girguis, who not only mentored me and provided invaluable guidance throughout this journey but also became a wonderful friend. Your support, wisdom, and humor made all the difference, and I'm so grateful for the bond we've built.

I would also like to thank my collaborators: Xianzhang Xu, Michael Mongin, Ignacio Andreu-Angulo, and many others too numerous to list. Working with you was a truly enriching experience, and your insights and expertise were invaluable in advancing my research. I deeply appreciate the time, effort, and thoughtful discussions you brought to our work together. I would also like to thank the National Science Foundation, whose funding made this research possible through awards #2437344

and #2003951. Their support has been instrumental in enabling this work, and I am deeply grateful.

To my parents, I owe everything. Your sacrifices, perseverance, and unwavering support have been the foundation of every success I have achieved. You instilled in me the values of hard work, resilience, and the importance of education. This is as much yours as it is mine. To my brothers, thank you for your encouragement, belief in me, and the countless ways you've supported me along the way.

To my wife, Alexandra, you have been my anchor and my greatest source of strength throughout this journey. Your love, patience, and unwavering belief in me have carried me through the most challenging times. You celebrated my victories, supported me in moments of doubt, and reminded me of the bigger picture when I lost sight of it. Thank you for being my partner in every sense of the word and for making this journey not just possible but meaningful.

This accomplishment would not have been possible without all of you. Thank you from the bottom of my heart.

Χάριτι δὲ Θεοῦ εἰμι ὅ εἰμι

Δόξα τῷ Θεῷ πάντων ἕνεκεν

Table of Contents

Acknowledgements ii

1 Introduction 1
- 1.1 Motivation . . . 1
- 1.2 Background . . . 2
  - 1.2.1 Unsteady force production . . . 2
  - 1.2.2 Gust encounters and gust mitigation . . . 8
- 1.3 Dissertation outline . . . 11

2 Physics of unsteady aerodynamics 13
- 2.1 Fundamentals of viscous, incompressible aerodynamics . . . 13
  - 2.1.1 Equations of motion . . . 13
  - 2.1.2 Vorticity and circulation . . . 14
  - 2.1.3 Aerodynamic impulse . . . 16
- 2.2 Potential flows and inviscid aerodynamics . . . 17
  - 2.2.1 Governing equations . . . 17
  - 2.2.2 Vortices and vortex sheets . . . 18
  - 2.2.3 Circulation conservation . . . 21
  - 2.2.4 Equivalent inviscid flows . . . 22
  - 2.2.5 Thin-airfoil theory . . . 24
- 2.3 Decomposition of aerodynamic loading . . . 26
  - 2.3.1 Steady loads . . . 27
  - 2.3.2 Quasi-steady loads . . . 28
  - 2.3.3 Unsteady circulatory loads . . . 29
  - 2.3.4 Non-circulatory loads . . . 31
  - 2.3.5 Indicial response aerodynamics . . . 33
  - 2.3.6 Load decomposition . . . 37
- 2.4 Viscous flow physics . . . 40
  - 2.4.1 Leading-edge vorticity flux . . . 40
- 2.5 Chapter summary . . . 44

3 Experimental methodology 45
3.1 Towing tank facility . . . 45
3.2 Gust generator . . . 46
3.3 Gust characterization . . . 48
3.4 Particle Image Velocimetry and load measurements . . . 48
3.4.1 Configuration I: Static PIV . . . 50
3.4.2 Configuration II: Tow PIV . . . 51
3.5 Pressure sensor wing model . . . 52
3.6 Measurement uncertainty and error propagation . . . 58
3.7 Data postprocessing and analysis . . . 59
3.7.1 Data synchronization and taring . . . 59
3.7.2 Isolation of aerodynamic pressure . . . 61
3.7.3 Pressure integration . . . 62
3.7.4 Vortex tracking . . . 63
3.7.5 Finite wing effects . . . 65
3.8 Chapter summary . . . 68

4 Evaluation of linear gust-encounter dynamics 69
4.1 Flow morphology and Reynolds number effects . . . 69
4.1.1 High gust ratio regime . . . 71
4.1.2 Low gust ratio regime . . . 73
4.1.3 Force measurements . . . 74
4.2 LEV growth . . . 76
4.3 Comparison of experimental and theoretical circulations . . . 77
4.4 Vortex detachment . . . 83
4.5 Chapter summary . . . 87

5 Unsteady surface pressure measurements in a gust 88
5.1 Steady measurements . . . 88
5.2 Unsteady measurements . . . 91
5.3 Transverse gust encounters . . . 93
5.3.1 Pressure-flowfield analysis . . . 93
5.3.2 Effect of gust ratio . . . 96
5.4 Pressure sensing . . . 98
5.4.1 Integrated pressure distributions . . . 98
5.4.2 Leading-edge suction and pressure gradient . . . 100
5.5 Chapter summary . . . 105

6 Inviscid modeling applications 106
6.1 Application I: Low-order unsteady pressure computation . . . 106
6.1.1 Computing inviscid, unsteady pressure . . . 106
6.1.2 Effect of gust model . . . 110
6.1.3 Effect of leading-edge separation . . . 113

6.2 Application II: Leading-edge vortex sensing 119
6.2.1 Attached vortex sheet model 120
6.2.2 Resolution of the leading-edge singularity 121
6.2.3 LEV strength estimation 124
6.3 Application III: Optimal gust mitigation kinematics 127
6.3.1 Iterative maneuver optimization 127
6.3.2 Optimal kinematics 130
6.4 Chapter summary 133

7 Conclusions 135
7.1 Summary and conclusions 135
7.1.1 Role of shed vorticity in lift production 135
7.1.2 Unsteady pressure distributions 137
7.1.3 Inviscid modeling applications 139
7.2 Original contributions 141
7.3 Suggestions for future work 142

Bibliography 144

Chapter 1: Introduction

1.1 Motivation

The operation of systems in unsteady flow environments is a central challenge across disciplines such as renewable energy, aerospace, and maritime engineering. Examples include aircraft flying through highly unsteady conditions, wind turbines subjected to turbulent fluctuations in the atmospheric boundary layer, and robotic fish navigating complex flowfields [27, 52, 62]. Addressing these challenges requires a fundamental understanding of unsteady flows, particularly those dominated by vorticity, as well as the development of sensing and control methods that enable engineered systems to operate effectively within such environments [5, 10, 48, 60, 71, 78, 90, 98].

An important class of unsteady flows relevant to flight vehicles are wing-gust encounters. Large force transients produced during wing-gust encounters can lead to permanent structural damage or catastrophic loss of control [112]. While gusts have been studied since the 1930's, early work was restricted to the use of potential flow modeling due to the limited experimental and computational tools available at the time [59]. The exact physics of gust encounters are to this day not well understood and have only recently gained widespread attention from the aerodynamics community [51].

Unsteady flows present significant challenges in the sensing and control of vehicles, beyond the lack of understanding of the underlying physics. These challenges

arise from the intrinsic nonlinearities associated with unsteady flow dynamics. For instance, accurately predicting forces and flowfields during a gust encounter requires understanding the complex relationship between vortical structures and the corresponding pressure signatures on a lifting surface. This underscores the need for physically grounded models and methods that enable systems to sense, predict, and adapt to unsteady flows in real time.

This dissertation addresses these challenges by advancing the understanding of gust encounter physics and exploring applications in flow sensing and control. Spefically, the goals of this dissertation are

1. Experimentally investigate the unsteady aerodynamics of wing-gust encounters using flowfield, load, and surface pressure measurements.

2. Develop flow sensing and control techniques that aid in the estimation of unsteady flowfields and forces produced during wing-gust encounters, as well as in the mitigation of undesirable gust loads.

1.2 Background

1.2.1 Unsteady force production

Calculating the forces on a body immersed in a fluid is a fundamental problem in fluid mechanics with important engineering applications. In aeronautics, calculation of the static and dynamic loads produced by an aircraft flight surface is an essential aspect of flight vehicle design. The governing equations of fluid motion are, in general, extremely difficult to solve. Aerodynamicists have instead resorted to either numerical simulations of the governing equations, also known as Computational Fluid Dynamics (CFD), or to simplified fluid flow models that can be solved analytically

or numerically. Specifically, the use of potential flow, which assumes an inviscid, irrotational, incompressible fluid, has been successful at predicting the aerodynamic lift on wings at low angles of attack, serving as the foundation of what is known as classical aerodynamics [53]. Its success can be traced to the observations of Prandtl [86] who postulated that viscous forces are negligible except close to solid boundaries, where the no-slip condition needs to be satisfied. Through a simplification of the governing equations, Prandtl showed that the pressure is approximately uniform across a boundary layer, and thus, for attached flows at high Reynolds numbers, potential flow is able to approximate the pressure distribution on a lifting surface [55]. Experimental data has shown that this holds true for both steady and unsteady flows, as long as the flow remains attached, and the vorticity shed from the trailing edge is accounted for [55, 102, 106, 107].

At high angles of attack, lifting surfaces exhibit trailing edge or leading edge separation, and the boundary layer arguments which justified the use of potential flow are no longer valid. This is manifested in the inability of potential flow to predict the reduction in the steady-state lift slope that occurs at high angles of attack. Unsteady potential flow lift predictions suffer the same shortcomings several convective times after an initial unsteady forcing - say a large step change in the angle of attack [70]. However, during the initial transient, researchers have observed that wings are able to sustain lift values close to the potential flow prediction [7, 37, 54, 70, 72, 77, 81]. This phenomenon, often called delayed stall, is a well-known characteristic of separated flows, and is facilitated by the formation of a leading-edge vortex (LEV). As described in McCroskey [74], a growing LEV attached to the wing delays stall at high angles of attack, which allows for higher instantaneous lift coefficients than would otherwise be possible under steady conditions. The LEV detachment process marks the end of lift enhancement and the inception of stall. Flows encompassing LEVs have been

studied extensively due to their prevalence in the unsteady locomotion of biological fliers and swimmers [32, 34].

The accuracy of unsteady potential flow models outside the domain of their validity can be perhaps explained through the concept of fluid impulse. In the absence of non-conservative forces, the fluid impulse is an invariant of the flow, despite any unsteadiness [91]. Thus, any forces on an immersed body can be calculated from the change in fluid impulse, which can be computed as a moment of the flow vorticity field [111],

$$\boldsymbol{I} = \frac{1}{n_d - 1}\left(\int_{V_f} \boldsymbol{x} \times \boldsymbol{\omega} \mathrm{d}V + \int_{S_b} \boldsymbol{x} \times (\hat{\boldsymbol{n}} \times \boldsymbol{u}) \mathrm{d}S\right) \tag{1.1}$$

$$\boldsymbol{F} = -\rho \frac{\mathrm{d}\boldsymbol{I}}{\mathrm{d}t} \tag{1.2}$$

where n_d denotes the number of dimensions, V_f is the fluid volume, S_b is the solid surface with unit normal vector $\hat{\boldsymbol{n}}$, $\boldsymbol{x}$ is the spatial coordinate, and $\boldsymbol{u}$ and $\boldsymbol{\omega}$ are velocity and vorticity vector fields, respectively. The second integral in (1.1) vanishes under the conditions that the reference frame is fixed to the body, and that this body frame is inertial. Lift can then be expressed as the change in vertical fluid impulse,

$$L = -\rho \frac{\mathrm{d}}{\mathrm{d}t} \int_{V_f} x \omega_z \mathrm{d}V \tag{1.3}$$

Equation (1.3) shows that lift can be explicitly computed from the generation of vorticity and its streamwise movement. It has been recently demonstrated that, in many cases, potential theory correctly predicts the development of both circulatory and non-circulatory vortex sheets [38, 39], which can be experimentally isolated using standard results of potential theory [22]. Hence, even if potential flow models require the use

of erroneous assumptions, they can still approximate lift transients by capturing the hydrodynamic impulse of viscous separated flows. Furthermore, vortex-impulse can be used to augment models using data from experiments or simulations. Notably, Babinsky et al. [7] used the above ideas to develop a low order model for pitching and surging wings. They found that Wagner's model [106] accurately predicted the lift of pitching and surging wings when the relative advection of vortices is properly accounted for. Polet et al. [84] used similar ideas to estimate the force on a wing undergoing a perching maneuver. Ōtomo et al. [82] found that Theodorsen's pitch model performs remarkably well despite the formation of a LEV, and the discrepancy in lift after the LEV detaches can be accounted for using the relative advection of the LEV with the circulation in the wake. Stevens and Babinsky [99] found that the LEV circulation as calculated from experimental measurements of a pitching wing closely follows the bound circulation predicted by Wagner's model, suggesting that the lift is dominated by the circulatory component regardless of whether a leading-edge vortex is formed or not. Furthermore, the work of Ford and Babinsky [37] showed that, for an impulsively started airfoil at high angle of incidence, most of the vorticity in the flow is not in the bound vortex but shed in the wake.

Küssner's transverse gust encounter model has also been reported to agree with experimental data for a wide range of gust ratios and gust profiles [9, 14, 21]. In the past, models of varying fidelity have been used to predict force transients produced during gust encounters, including unsteady potential flow [6], state-space formulations [95], and experimental, data-driven models [48]. However, Küssner's model has several enticing properties. Its computational simplicity makes it a great candidate for online control applications. Moreover, Küssner's model is based on well-understood physics, and its agreement with data suggests that it can be used to understand the different force producing mechanisms during a gust encounter [18]. Defining the gust ratio to

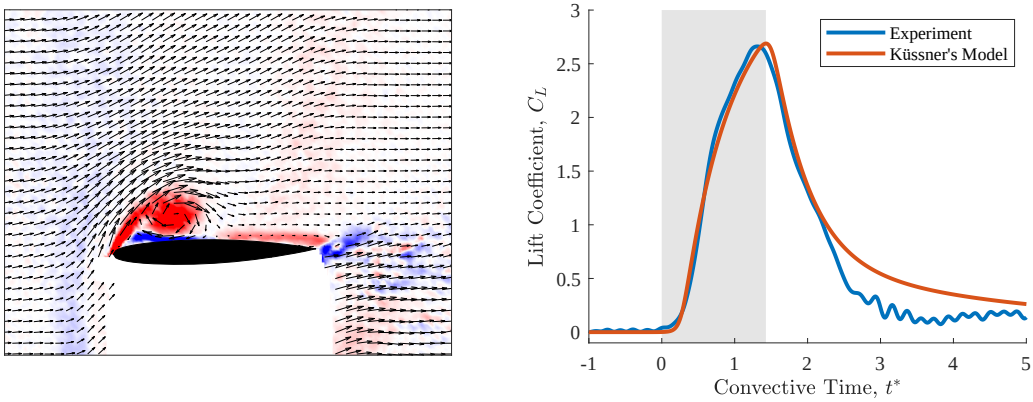

(a) (b)

Figure 1.1: Example experimental transverse gust encounter measurements: (a) Vorticity and velocity field and (b) experimental lift transient compared to Küssner's model

be the ratio of peak gust velocity to freestream velocity, i.e., $GR = V/U_\infty$, and the gust-width-to-chord ratio (w/c) to be the streamwise width of the gust divided by the chord, figure 1.1 depicts an example flowfield and lift transient for a transverse gust encounter with a trapezoidal gust profile, $GR = 0.75$, and $w/c = 1.4$. The grey area denotes the convective times that the leading edge is in the gust. The flow is massively separated at the leading edge (and therefore not potential), the wake is deflected due to the gust velocity, and the gust vorticity is deformed. However, the predictive ability of Küssner's model shown in figure 1.1b, suggests that the model is able to capture some essential aspects of the encounter. One of the goals of this dissertation is to identify the mechanisms by which this inviscid model is able to predict the lift transients of viscous, separated flows, and explore its limitations.

All unsteady potential flow models mentioned above have a known limitation: They overpredict force transients after LEV detachment. The concept of the optimal vortex formation introduced by Gharib et al. [42] and extended to unsteady airfoil kinematics by Dabiri [23], can be used to estimate the timescale of LEV detachment. It describes the non-dimensional period of time over which a single vortex created

by a vortex generator grows. Its maximal value denotes the time that the vortex stops entraining fluid from the shear layer and detaches. Optimal vortex formation is defined as $\hat{T} = C\Gamma/(D\Delta U)$ where Γ is the instantaneous circulation of the vortex, C is a constant depending on the configuration, D is the characteristic length scale of the flow, and ΔU is the velocity difference across the shear layer feeding the vortex. Dabiri [23] showed evidence that there is a universal optimal formation time $\hat{T} \approx 4$ in vorticity-driven lift and propulsion. However, subsequent research revealed that this is not always true [10, 89]. The variation in optimal vortex formation time has been attributed to differing LEV detachment mechanisms. Two competing mechanisms governing LEV detachment have been identified: the bluff body detachment mechanism and the boundary layer eruption mechanism [108]. The former is associated with the interaction of the LEV with the trailing edge of the wing. The latter is associated with the vortex-wall interaction between the LEV and the airfoil surface. A characterization of the relevant vortex detachment parameters can be found in Kissing et al. [57].

Given the demonstrated importance of the LEV, another goal of this dissertation is to analytically investigate its growth during a gust encounter. The seminal work of Didden [28] expressed the growth rate of a vortex by integrating the vorticity flux over the shear layer. By assuming a linear velocity profile across the shear layer, the vorticity can be approximated by,

$$\omega_z \approx \frac{\mathrm{d}u}{\mathrm{d}y} \approx \frac{\Delta U}{\delta} \tag{1.4}$$

where δ is the thickness of the shear layer feeding the vortex. The approximation is shown in equation (1.5). Similarly, the size of the LEV can be approximated by the mass flux from the shear layer into the vortex. Written in terms of non-dimensional

quantities, the results for circulation and area of a vortex are shown in equations (1.6) and (1.9), respectively, where $t^* = tU_\infty/c$ is the convective time.

$$\Gamma(t) = \int_0^t \int_0^\delta u\omega_z \mathrm{d}y\mathrm{d}\tau = \int_0^t \int_0^\delta u\frac{\mathrm{d}u}{\mathrm{d}y}\mathrm{d}y\mathrm{d}\tau \approx \frac{1}{2}U_\infty^2 t \tag{1.5}$$

$$\frac{\Gamma(t^*)}{cU_\infty} = \frac{t^*}{2} \tag{1.6}$$

$$\tag{1.7}$$

$$A(t) = \int_0^t \int_0^\delta u\mathrm{d}y\mathrm{d}\tau \approx \frac{1}{2}U_\infty \delta t \tag{1.8}$$

$$\frac{A(t^*)}{c^2} = \frac{\delta t^*}{2c} \tag{1.9}$$

Widmann and Tropea [108] used the above results along with a Falkner-Skan approximation for the boundary layer thickness, δ, to investigate the vortex detachment mechanisms of a plunging airfoil. Rival et al. [90] and Sattari et al. [92] used a similar approximation to study the growth of starting vortices and the effects of leading-edge geometry on LEV growth and detachment.

1.2.2 Gust encounters and gust mitigation

To first order, simple, discrete gust encounters can be approximated by forced wing kinematics. For example, the flow seen by the leading-edge of an airfoil during a transverse gust encounter is identical to that of a plunging airfoil. However, transverse gusts are parameterized by a different set of dimensionless numbers, namely, the gust ratio $GR = V/U_\infty$, where V is the maximum gust velocity, the chord to gust width ratio, c/w, and the gust profile (or effective angle of attack history at the leading-edge). Nevertheless, there are strong relationships across the two parameter spaces. The reduced frequency defined as $k = \pi f c/U_\infty$ where f is the oscillation frequency

of an aerodynamic profile, can be defined for gusts if the period of the interaction is defined to be the amount of time the wing spends in the gust, i.e., w/U_∞. By this definition the reduced frequency of the gust simply becomes $k = \pi(c/w)$, a scaled version of the chord to gust width ratio. Similarly, for canonical top-hat gusts the Strouhal number which is defined as the ratio between a forcing velocity and the freestream velocity, is analogous to the gust ratio. This is in agreement with findings that the Strouhal number and the gust ratio are the main parameters governing force production in their respective areas of application [6, 80]. Using these relations, it becomes clear that the discrete gusts of interest currently being studied are well within the region of Strouhal numbers previously studied by the aerodynamics community, but at reduced frequencies an order of magnitude higher. This has implications relating to the evolution of force-producing flow characteristics such as the LEV, which at higher reduced frequencies will have less time to develop before the wing exits the gust.

Gust encounters have been studied theoretically and experimentally since the 1930s [58, 59]. These studies identified the gust ratio ($GR = V'/U_\infty$), the ratio of the disturbance velocity to the freestream velocity, as a key parameter governing the associated dynamics. Due to the limitations of the experimental and analytical tools available at the time, early investigations were constrained to small gust ratios ($GR \sim 0.1$), where linear approximations of the governing equations provided an adequate description of the dynamics. Recent advances in experimental and computational methods have enabled the exploration of high gust ratios ($GR \sim 1$), where nonlinear effects such as flow separation, vortex dynamics, and gust deformation play a significant role [6, 8, 14, 40]. Experimental towing tank facilities equipped with gust generator hardware have proved to be a valuable tool in the investigation of transverse gust encounters. In towing tanks, generated gusts need not convect with

the freestream, thus allowing a large parameter space involving gust profile, width and strength, as well as model kinematics to be explored [6, 8, 21, 41, 83, 97].These studies have yielded critical insights into the aerodynamics of large-amplitude gust encounters, and particularly, on the formation and shedding of leading-edge vortices, which dominate the unsteady aerodynamic response.

Building on this foundational work, recent gust encounter research has focused on gust mitigation through kinematic actuation. In these studies, wings are actively controlled to achieve desirable load responses during gust encounters [5, 48, 85, 98]. Recent work has shown that active wing pitching based on feedback from lift measurements can significantly reduce undesirable load transients during wing-gust interactions [5, 98]. Similar techniques have been applied to wind energy systems, where active blade pitch control of vertical-axis wind turbines has been demonstrated to achieve a threefold increase in power generation [63]. While effective, such control strategies depend on direct load measurements, which are typically not available outside of the laboratory. This limitation underscores the need for alternative sensing methods capable of providing flow information to controllers. To address this, this dissertation explores the use of surface pressure measurements as a practical means of inferring aerodynamic loads and capturing key flow phenomena during large-amplitude transverse wing-gust encounters. The aim of this work is to study the flow physics of transverse gust-encounters using simultaneous surface pressure, load, and flowfield measurements, and also to investigate various flow sensing methods that can provide valuable information about the state of the unsteady flow.

For unsteady flow investigations, surface pressures have been historically used to provide important connections between the structures in the flow, model loads, and vorticity generation mechanisms on surfaces [1, 16, 32, 77]. Surface pressures are also commonly used in conjunction with physics-driven or data-driven modeling,

to estimate and control loads and flowfields in real time [2, 17, 43, 47]. Recently, progress in the low-order modeling of unsteady flows has highlighted the importance of airfoil leading-edge suction, a phenomenon tied to the surface pressure distribution near the leading edge [88, 101]. Hence, surface pressure measurements can also aid in the investigation of leading-edge separation [24, 46]. Unfortunately, surface pressure measurement in towing tanks is considered a laborious task, and require considerable manufacturing and post-processing efforts. Jentzsch et al. [50] recently outlined many of the challenges associated with towing tank pressure measurements. Notably, towing tank models experience relatively low dynamic pressures, and thus, small pressure differences that are hard to measure. The use of tubing, which connect pressure taps on the model surface with pressure transducers located away from the model also create complications. When measuring water pressure, tubing introduces alterations in pressure amplitude and phase, which are especially detrimental for unsteady measurements [13]. Trapped air in the tubing can also contribute to the error through its inertia (as the tubing is often accelerated with the model) as well as through the impedance mismatch on the air-water interface. As part of this study, an instrumented wing model was developed to overcome some of measurement complications discussed above. A secondary objective of this dissertation is to present and validate the design methodology for the instrumented wing model, with the aim of providing a useful framework for researchers seeking to acquire dense surface pressure distribution data in towing tank experiments.

1.3 Dissertation outline

This dissertation is organized as follows: Chapter 2 reviews the relevant inviscid and viscous physics underlying wing-gust encounters. Chapter 3 details the experi-

mental methods employed in this study. Chapter 4 presents load and flowfield measurements of transverse wing-gust encounters across varying gust ratios and Reynolds numbers, evaluating the applicability of linear aerodynamic theory to fully separated gust encounter flows. Chapter 5 examines simultaneous pressure, load, and flowfield measurements, investigating the potential of pressure sensors for flow sensing applications. Chapter 6 explores the use of inviscid modeling to address challenges related to flow sensing and gust mitigation. Finally, Chapter 7 summarizes the findings, highlights key contributions, and offers suggestions for future research.

Chapter 2: Physics of unsteady aerodynamics

This chapter presents the fundamental principles of unsteady aerodynamics in the context of wing-gust encounters, emphasizing the physical mechanisms that govern time-dependent fluid flows and the forces they generate. It begins with an overview of viscous, incompressible aerodynamics, exploring the equations of motion, vorticity dynamics, and their relevance to unsteady flows. The discussion extends to potential flow theory, offering insights into inviscid approximations and their applicability to modeling unsteady aerodynamic phenomena. By combining these perspectives, the chapter establishes a comprehensive framework for analyzing the aerodynamic loading experienced by wings during gust encounters and the underlying flow physics driving these interactions.

2.1 Fundamentals of viscous, incompressible aerodynamics

2.1.1 Equations of motion

An important non-dimensional parameter that governs the motion of fluids is the Mach number, which is defined as the ratio of flow velocity to the speed of sound. If the Mach number of a particular flow is small, then dynamic density variations become negligible and the fluid is said to be incompressible. The dynamics of incompressible fluids are governed by the incompressible Navier-Stokes equations, which are mathematical statements of the fluid's mass and momentum conservation. Conservation of

mass for an incompressible fluid necessitates that its velocity field is divergence-free,

$$\nabla \cdot \mathbf{u} = 0 \tag{2.1}$$

where $\mathbf{u}$ is the velocity vector field of the flow. Conservation of momentum for an incompressible fluid relates the acceleration of the flow to internal and external forces acting on the fluid. In the absence of gravity and other body forces, the conservation of momentum reads,

$$\frac{\partial \mathbf{u}}{\partial t} + \mathbf{u} \cdot \nabla \mathbf{u} = -\frac{1}{\rho}\nabla p + \nu \nabla^2 \mathbf{u} \tag{2.2}$$

where p is the pressure of the flow and ν is the kinematic viscosity of the medium. The first term on the left-hand-sight of equation (2.2) represents acceleration due to the local time evolution of the velocity field. Any flow for which this term is non-zero is called *unsteady*. The second term on the left-hand-side represents the spatial acceleration of the velocity field while the right-hand-side terms represent the pressure and shear forces in the flow. If an immersed body exists within the flow domain – as is typical for aerodynamic flows – the governing equations need to be supplemented with appropriate boundary conditions. For viscous flows, the appropriate boundary condition is the no-slip condition, which states that the flow velocity on the body's surface is equal to that of the body, $\mathbf{u} = \mathbf{U}$. In other words, in a body-fixed reference frame, all the components of velocity are equal to zero.

2.1.2 Vorticity and circulation

An important concept in the study of aerodynamics is that of flow *vorticity*. Vorticty is defined to be the curl of a velocity field, $\boldsymbol{\omega} = \nabla \times \mathbf{u}$, and is equivalent to twice the angular velocity of a local fluid element [66]. Its evolution equation can be

obtained by taking the curl of the mass and momentum conservation equations and combining them to yield,

$$\frac{\partial \boldsymbol{\omega}}{\partial t} + \mathbf{u} \cdot \nabla \boldsymbol{\omega} = \boldsymbol{\omega} \cdot \nabla \mathbf{u} + \nu \nabla^2 \boldsymbol{\omega} \tag{2.3}$$

This equation is often called the vorticity transport equation and states that vorticity dynamics are driven by two mechanisms: tilting and stretching of vorticity due to flow velocity gradients ($\boldsymbol{\omega} \cdot \nabla \mathbf{u}$) and viscous diffusion ($\nu \nabla^2 \boldsymbol{\omega}$). In two-dimensional flows, the velocity and vorticity vector fields are necessarily perpendicular, and the vortex tilting and stretching term vanishes [91]. Hence, in two dimensions the vorticity tranport equation can be written as

$$\frac{\mathrm{D}\boldsymbol{\omega}}{\mathrm{D}t} = \nu \nabla^2 \boldsymbol{\omega} \tag{2.4}$$

where we have used the definition of the substantial derivative, $\frac{\mathrm{D}()}{\mathrm{D}t} = \frac{\partial()}{\partial t} + \mathbf{u} \cdot \nabla()$.

A related and equally important quantity is the flow *circulation*. Circulation in a flow is defined as a line integral of velocity around a closed curve,

$$\Gamma = \oint_{\partial S} \mathbf{u} \cdot \, d\mathbf{l}. \tag{2.5}$$

By Stoke's theorem, the circulation can be related to the flux of vorticity through the surface bounded by the line integral contour [91],

$$\Gamma = \oint_{\partial S} \mathbf{u} \cdot \, \mathbf{dl} = \iint_S \nabla \times \mathbf{u} \cdot \, d\mathbf{S} = \iint_S \boldsymbol{\omega} \cdot \, d\mathbf{S}. \tag{2.6}$$

In two-dimensions, the vorticity field and vector area element are parallel, and equa-

tion (2.6) reduces to

$$\Gamma = \iint_S \omega_z \, dS \tag{2.7}$$

where ω_z is the out-of-plane vorticity component. Thus, circulation is a measure of the total vorticity in a given area and characterizes the angular momentum enclosed by the bounding curve. Its conservation properties will be used to provide a convenient formulation to understanding unsteady aerodynamic loading.

2.1.3 Aerodynamic impulse

An immersed body experiences pressure and shear forces everywhere on its surface. Integrating these quantities results in the total aerodynamic loading experienced by the body [3],

$$\mathbf{F} = \oiint p\hat{\mathbf{n}} \, dS + \oiint \overline{\overline{\boldsymbol{\tau}}}_w \cdot \hat{\mathbf{n}} \, dS \tag{2.8}$$

where $\overline{\overline{\boldsymbol{\tau}}}_w$ is the viscous stress tensor. An indirect method to compute aerodynamic loading is through the rate of change of impulse of the flow [111]. The reasoning is as follows: In the absence of any immersed bodies and non-conservative forces, fluid impulse is an invariant of the flow, despite any unsteadiness [91]. Thus, any change in fluid impulse can be attributed to the force imparted on the fluid by an immersed body. Specifically, the force on an immersed body can be calculated from the rate of change in fluid impulse, which can be computed as a moment of the flow vorticity field [111],

$$\mathbf{I} = \frac{1}{n_d - 1} \left(\int_{V_f} \boldsymbol{x} \times \boldsymbol{\omega} \, dV + \int_{S_b} \boldsymbol{x} \times (\hat{\boldsymbol{n}} \times \boldsymbol{u}) \, dS \right) \tag{2.9}$$

$$\mathbf{F} = -\rho \frac{\mathrm{d}\boldsymbol{I}}{\mathrm{d}t} \tag{2.10}$$

where $\mathbf{I}$ is the fluid impulse, n_d denotes the number of dimensions, V_f is the fluid volume, S_b is the solid surface with unit normal vector $\hat{\boldsymbol{n}}$, and $\boldsymbol{x}$ is the spatial coordinate. This is a very useful theoretical and computational tool in the study of unsteady flows. To see why, we can evaluate the expression for a two-dimensional flow in a reference frame which is fixed to the body and for which the freestream velocity vector is parallel to the x-axis. The second integral in (2.9) vanishes and the lift can be expressed as a change in vertical fluid impulse,

$$L = -\rho \frac{\mathrm{d}}{\mathrm{d}t} \int_{V_f} x\omega_z \mathrm{d}V. \tag{2.11}$$

Equation (2.11) shows that lift can be explicitly computed from the generation of vorticity and its streamwise movement. In unsteady flows – and particularly those associated with wing-gust encounters – the background flowfield is inherently vortical while the wing is shedding its own vorticity. Thus, equation (2.11) provides a path to study the impact of gust vorticity, shed vorticity, and their cross-interaction on the aerodynamic loading.

2.2 Potential flows and inviscid aerodynamics

2.2.1 Governing equations

A flow is said to be potential if it is inviscid ($\nu = 0$) and irrotational ($\boldsymbol{\omega} = \nabla \times \mathbf{u} = 0$). These two assumptions imply that velocity field can be written as a the gradient of a scalar potential, $\mathbf{u} = \nabla\phi$ [11]. Conservation of mass further implies that this potential satisfies Laplace's equation,

$$\nabla^2 \phi = 0. \tag{2.12}$$

The absence of viscosity in inviscid flows means that there is no mechanism to enforce the no-slip boundary condition on solid walls. Thus, for inviscid flows the boundary condition becomes a statement of equivalence of the *normal* velocity components between the body and flow, $\hat{\mathbf{n}} \cdot \nabla\phi = \mathbf{U} \cdot \hat{\mathbf{n}}$, where $\hat{\mathbf{n}}$ is the surface unit normal vector. In other words, there is no requirement for the tangential velocity in the flow to be continuous. Areas of tangential velocity discontinuity are called *vortex sheets* [91]. In inviscid flows, vortex sheets can be found on the surfaces of immersed bodies but can also be found convecting freely in the flow. They are important objects in this dissertation and their properties will be analyzed in some detail.

Potential flows can also be described through their streamfunction, ψ. The streamfunction is orthogonal to the potential and is constant along streamlines of the flow. Defining the vector potential $\boldsymbol{\psi} = [0, 0, \psi]^T$, the velocity can be computed from the streamfunction as $\mathbf{u} = \nabla \times \boldsymbol{\psi}$. Plugging this into $\boldsymbol{\omega} = \nabla \times \mathbf{u} = 0$ implies that the streamfunction also satisfies Laplace's equation, $\nabla^2\psi = 0$.

The potential flow formulation is convenient for several reasons. First, the fundamental solutions to Laplace's equations are mathematically very well understood and can be used to construct simple potential flows. Second, Laplace's equation is *linear*, meaning that we can use the principle of superposition to build up complicated flows from simple ones. We will use this fact to our advantage to model the complicated flows associated with gust encounters.

2.2.2 Vortices and vortex sheets

While potential flows are defined to be irrotational, they allow vorticity in the form of isolated singularities [91]. Singular flow elements can be understood through the fundamental solution of Laplace's equation, $G(\mathbf{x})$, which satisfies $\nabla^2 G(\mathbf{x}) = \delta(\mathbf{x})$,

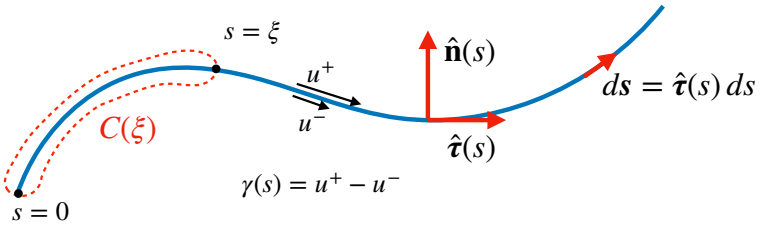

Figure 2.1: Depiction of a vortex sheet and its properties

and in two dimensions reads $G(\mathbf{x}) = \frac{1}{2\pi}\log|\mathbf{x}|$. $G(\mathbf{x})$ is also called the Green's function of the Laplace operator. Singularities based on the fundamental solution satisfy the potential flow assumptions everywhere except at isolated points in the flow. The simplest of these singular solutions is the *point vortex*, whose streamfunction can be written in terms of the Green's function as $\psi = \Gamma G(\mathbf{x})$, where Γ is a measure of the strength of the vortex and is defined as the circulation of a contour encompassing the vortex. The induced velocity of the point vortex can be computed from the streamfunction or through the *Biot-Savart law*, which inverts the curl operator and computes the velocity field from the vorticity field. Recognizing that the vorticity field of the point vortex is the dirac-delta function, $\boldsymbol{\omega} = \Gamma\delta(\mathbf{x})\hat{\mathbf{e}}_3$, where $\hat{\mathbf{e}}_3$ is the out-of-plane unit vector, the velocity can be computed from Biot-Savart (2.13)as,

$$\mathbf{u}(\mathbf{x}) = \int_{V_f} \nabla G(\mathbf{x}-\mathbf{y}) \times \boldsymbol{\omega}(\mathbf{y})\, dV(\mathbf{y}) \tag{2.13}$$

$$\mathbf{u}(\mathbf{x}) = \nabla G(\mathbf{x}) \times \Gamma\hat{\mathbf{e}}_3 \tag{2.14}$$

.

Another important singular element is the vortex sheet, depicted in figure 2.1. In a two-dimensional flow, a vortex sheet is a surface across which there exists a discon-

tinuity of tangential velocity. The jump in tangential velocity is the local strength of the vortex sheet, $\gamma(s) = u^+ - u^-$. Its velocity contribution to the flowfield can be computed through the use of the Biot-Savart law and by recognizing that its differential lengths, ds, can be regarded as point vortices with strength $\gamma(s)\,ds$.

The local jump in tangential velocity implies a local jump in potential across the vortex sheet, $\Delta\phi = \phi^+ - \phi^-$. For reasons that will become clear in later sections, we are interested in calculating that potential jump. First, we recognize that the jump in potential is related to the strength of the vortex sheet through its tangential gradient,

$$\gamma(s) = -\hat{\boldsymbol{\tau}}(s) \cdot \nabla(\phi^+(s) - \phi^-(s)) = -\frac{\partial \Delta\phi}{\partial s}. \tag{2.15}$$

Second, we define the local circulation for the sheet by computing the circulation integral with a contour that crosses the sheet at location $s = \xi$, as shown in figure 2.1. Since the flow is potential, the loop can be deformed to wrap the vortex sheet tightly, leading to the following,

$$\Gamma(\xi) = \oint_{C(\xi)} \mathbf{u} \cdot d\boldsymbol{\ell} \tag{2.16}$$

$$= \int_0^\xi \left(u^+(s) - u^-(s)\right)\, ds \tag{2.17}$$

$$= \int_0^\xi \gamma(s)\, ds. \tag{2.18}$$

Taking derivative of (2.18) with respect to ξ and setting equal to (2.15) leads to,

$$\frac{\mathrm{d}\Gamma}{\mathrm{d}s} = -\frac{\partial \Delta\phi}{\partial s}. \tag{2.19}$$

This is a useful relationship that allows us to compute the potential jump using the definition of circulation. Finally, to compute the integration constant we need one

boundary condition. For the sheet in figure 2.1, $\Delta\phi(s=0)=0$ so integration yields, $\Delta\phi(s)=-\Gamma(s)$, which allows us to compute the potential jump of a vortex sheet at an integral of its strength, $\gamma(s)$. Namely,

$$\Delta\phi(\xi) = -\int_0^{\xi} \gamma(s)\, ds. \tag{2.20}$$

2.2.3 Circulation conservation

A useful observation is that for potential flows, the 2D vorticity transport equation (2.4) simplifies to $D\boldsymbol{\omega}/\,Dt = 0$, which implies that the vorticity of a material volume – or a volume that follows the same fluid particles in time - remain constant. The equivalent result in terms of circulation is called *Kelvin's circulation theorem* [103] and reads,

$$\frac{\mathrm{D}\Gamma}{\mathrm{D}t} = 0. \tag{2.21}$$

For unbounded flows, we can choose the material volume to be the whole flowfield, leading us to the conclusion that the overall circulation in an unbounded flow must be constant in time. Note that if a body exists within that volume, the circulation about the body must be accounted for in the integral. This can be seen from the following calculation which starts from (2.7) and uses Stoke's theorem to replace the volume integral inside the body with a line integral on its bounding surface,

$$\Gamma = \iint_{S_f \cup S_b} \nabla \times \mathbf{u}\, dS \tag{2.22}$$

$$= \iint_{S_f} \nabla \times \mathbf{u}\, dV + \oint_{C_b} \mathbf{u} \cdot\, d\mathbf{l} \tag{2.23}$$

$$= \iint_{S_f} \boldsymbol{\omega}_z\, dV + \Gamma_b \tag{2.24}$$

where S_f is the planar fluid region, S_b is the region occupied by the body, C_b is its bounding contour, and Γ_b is the circulation of a contour wrapped tightly around the body. For a non-rotating body in a viscous fluid, Γ_b as defined here is 0 by virtue of the boundary conditions, and all of the circulation is contained within the fluid (a rotating body contributes a factor of twice its angular velocity to the overall vorticity). However, a body immersed in an inviscid flow will have a vortex sheet on its surface and the overall circulation of the vortex sheet must be included in the circulation budget.

An important observation came from Wu [111], who explains that the conservation of circulation is also true for viscous flows, if the contour is drawn through regions with negligible shear stress. This is because there can be no advective vorticity transport across the material contour as it moves with the fluid, and only viscous diffusion can allow for vorticity to cross the boundary. Again, for unbounded flows the contour can be drawn to contain the whole flowfield, far away from any immersed bodies, and this guarantees negligible viscous diffusion at the contour for any finite amount of time. The conservation of circulation will be applied to both viscous and inviscid domains and will play an important role in the understanding of wing-gust encounter flows.

2.2.4 Equivalent inviscid flows

Potential flow theory provides a convenient modeling platform for analyzing and computing aerodynamic flows. However, its use requires some justification since it is necessitates an idealization of the flowfield. There is also some ambiguity in deriving relevant potential flows from viscous flows. To address these issues, we utilize the concept of an equivalent inviscid flow [30]. Equivalent inviscid flows are derived by lumping vorticity in the viscous layers into singular vortical elements. The procedure

is demonstrated in figure 2.2. Figure 2.2a depicts a viscous representation of a gust encounter flow. The wing's boundary layers have nonzero thickness and merge at the trailing edge to form the wake shear layer. Further, there exists ambient flow vorticity which interacts with the wing and its shed vorticity – a distinctive characteristic of wing-gust encounter flows. Figure 2.2b shows an equivalent inviscid flow to the one shown in figure 2.2a. The boundary layers and wake shear layers have been aggregated into vortex sheets of appropriate strengths, and the ambient flow vorticity into a collection of point vortices. Another important equivalent inviscid flow can be obtained by merging the top and bottom segments of the airfoil vortex sheet. This is depicted in figure 2.2c and is called the thin airfoil representation of the airfoil [3]. Thin-airfoil modeling has allowed important analytical results in both steady and unsteady aerodynamics, some of which will be discussed in the coming sections.

A justification for neglecting the effects of viscosity can be made based on the impulse perspective presented in section 2.1.3. Aerodynamic impulse states that aerodynamic loads can be calculated solely from the generation and movement of vorticity relative to the wing [111]. While the presence of vorticity in boundary layers is restricted to viscous flows, the generation of vorticity on solid surfaces is understood to be an inviscid process, and the action of viscosity is simply to diffuse the vorticity away from the body [76]. Furthermore, the movement of vorticity for unsteady aerodynamics flows in the Reynolds number range being investigated in this dissertation ($\mathrm{Re} = \mathcal{O}(10^5)$) can be considered to be *convection-dominated*. This is because diffusion timescales are typically much longer than convection timescales for moderately high Reynolds numbers. These two observations help classify the action of viscosity as having a secondary role on aerodynamic loads. This allows us to justify the use of potential flow dynamics and replace the boundary layers and other flow vorticity with vortex sheets and point vortices, as shown in figure 2.2b. One obvious

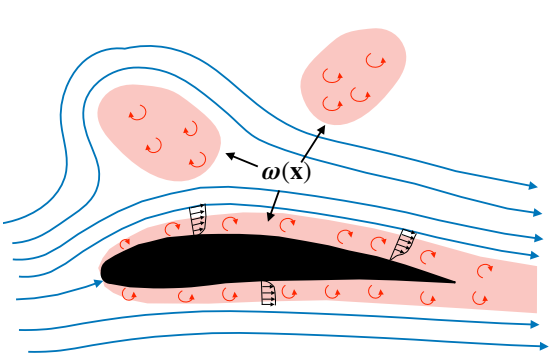

(a) Viscous aerodynamic flow containing vortical disturbances and boundary layers.

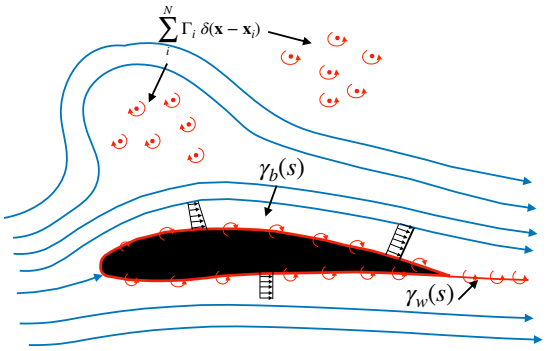

(b) Equivalent potential flow with singular vorticity elements replacing locations of flow shear.

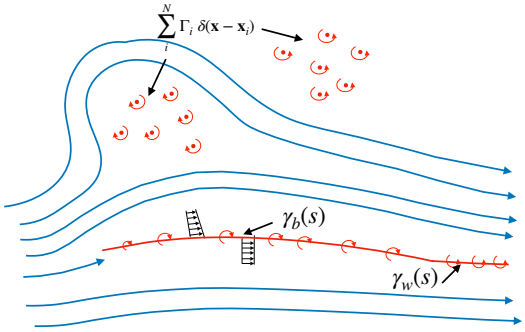

(c) Representation of the body as a thin airfoil.

Figure 2.2: Correspondence between viscous aerodynamic flow and equivalent potential flows with thick and thin airfoils.

weakness of this analysis is its omission of boundary layer separation, a phenomenon which will play a critical role in wing-gust encounter dynamics. In this dissertation, separation will be modeled heuristically and will be discussed in some detail later on in the text.

2.2.5 Thin-airfoil theory

The representation of a wing as a thin airfoil, as in figure 2.2c, along with the use of potential flow physics has led to a variety of useful aerodynamics concepts.

The thin-airfoil problem seeks to find the strength of the bound vortex sheet, γ_b, which satisfies the problem boundary conditions. The first boundary condition states that the flow induced by the vortex sheet, as described by the Biot-Savart law, must ensure that there are no normal velocities on the airfoil, turning the camber line of the airfoil into a streamline of the flow. The second condition, called the Kutta condition, requires the flow to leave tangentially at trailing edge. The solution for this vortex sheet strength, γ_b and its overall circulation Γ_b can be famously written as a Fourier series using the transform $x = c/2(1 - \cos\theta)$, where c denotes the chord length [3],

$$\gamma_b(\theta, t) = 2U_\infty\Big(A_0(t)\frac{1+\cos(\theta)}{\sin(\theta)} + \sum_{n=1}^{\infty} A_n(t)\sin(n\theta)\Big) \tag{2.25}$$

$$\Gamma_b(t) = \int_0^c \gamma_b(x,t)\,dx = U_\infty c\pi\Big(A_0(t) + \frac{A_1(t)}{2}\Big). \tag{2.26}$$

A_n are the Fourier coefficients which can be expressed in terms of the wing downwash distribution, $W(x,t)$, defined to be the local normal velocity on the wing induced from all flow elements *except the bound vortex sheet*,

$$A_0(t) = -\frac{1}{\pi}\int_0^\pi \frac{W(x,t)}{U_\infty}\,d\theta \tag{2.27}$$

$$A_n(t) = \frac{2}{\pi}\int_0^\pi \frac{W(x,t)}{U_\infty}\cos(n\theta)\,d\theta. \tag{2.28}$$

The downwash distribution includes the induced velocity from wing kinematics as well as from flow vorticity. For example, it can include the induced normal velocity of due to a wing pitching or due to the vorticity from a gust. This formulation will help us analyze different aerodynamic loads experienced by wings in a variety of unsteady flows useful to this dissertation.

2.3 Decomposition of aerodynamic loading

In this section we use models of aerodynamic flows and understand the various contributions to unsteady aerodynamic loading. The discussion will be based on flows produced from unsteady wing kinematics, gust encounters, as well as their combination. An important non-dimensional number that parameterizes unsteady wing kinematics is the reduced frequency,

$$k = \frac{\pi f c}{U_\infty} \tag{2.29}$$

where f is the characteristic unsteady frequency. For example, f can be the frequency of oscillation of a flapping wing. A high reduced frequency implies high degree of unsteadiness. While gust encounter flows are typically not associated with a reduced frequency, we can define an analogous parameter. Instead of frequency, we can think about the *period* of the gust encounter, or the amount of time a wing spends inside a gust. For wings moving with constant velocity U_∞, the gust period is defined as $T = w/U_\infty$, where w is the gust width. Plugging in $f = 1/T$ to the definition of reduced frequency results in,

$$k_{gust} = \frac{\pi c}{w} \tag{2.30}$$

which is proportional to the inverse of the gust-width-to-chord ratio, w/c. Thus, we can expect gusts that are long compared to the chord to induce less unsteadiness as flow variations take place over large time intervals.

2.3.1 Steady loads

For $k = 0$ the flow is steady and the aerodynamic loading is solely due to the wing's circulation. This is evident from the well-known Kutta–Joukowski theorem which relates the circulation of a wing to its lift through $L = \rho U_\infty \Gamma_b$ [3]. Consider a thin airfoil with no camber, and at a small angle of attack. The downwash distribution can be written as $W(x) = U_\infty \sin(\alpha) \approx U_\infty \alpha$, where α is the geometric angle of attack of the airfoil. Each of the Fourier coefficients vanish except for A_0 which evaluates to $A_0 = \alpha$. The bound vortex sheet, its circulation, and the lift coefficient, $C_l = 2L/(\rho U_\infty^2 c)$ evaluate to,

$$\gamma_b(x) = -2\alpha U_\infty \frac{\sqrt{c-x}}{\sqrt{x}} \tag{2.31}$$

$$\Gamma_b = U_\infty c \pi \alpha \tag{2.32}$$

$$C_l = 2\pi\alpha \tag{2.33}$$

In this case, the lift coefficient is proportional to the wing's angle of attack. If we now consider a camber distribution $z(x)$, then the local downwash distribution becomes $W(x) = U_\infty \left(\sin(\alpha) + \tan^{-1}(-\frac{\mathrm{d}z}{\mathrm{d}x})\right) \approx U_\infty \left(\alpha - \frac{\mathrm{d}z}{\mathrm{d}x}\right)$. Evaluating the Fourier integrals of thin-airfoil theory and using the Kutta–Joukowski theorem results in the following lift coefficient,

$$C_l = 2\pi \left(\alpha + \frac{1}{\pi} \int_0^\pi \frac{\mathrm{d}z}{\mathrm{d}x} (\cos(\theta) - 1)\, d\theta \right) = 2\pi \alpha_{\text{eff}} \tag{2.34}$$

In this case, the lift coefficient is proportional to the *effective angle of attack*, α_{eff}, defined as the quantity inside the parenthesis. The effective angle of attack adjusts the geometric angle of attack to to the varying flow incidence along the chord. Note

that camber is not weighted equally along the chord, and points near the trailing edge have a larger influence on the effective angle of attack.

2.3.2 Quasi-steady loads

Unsteady flows exhibiting low reduced frequencies (typically $0 < k < 0.05$) are classified as quasi-steady [65]. Quasi-steady flows exhibit time-varying loads and inevitably time-varying wing circulation. Kelvin circulation theorem necessitates that vorticity be shed from the wing to balance this change in body circulation. However, even though shed vorticity is theoretically present in quasi-steady flows, it is quickly convected away by the freestream and does not contribute to the loads over meaningful timescales. Instead, the unsteady loading is dominated by the change in incidence induced by the kinematics or a gust. This can be theoretically quantified as a change in the wing's effective angle of attack. Figure 2.3 shows different types of unsteady flows and their quasi-steady representation. Pitching motion is defined by its pitch rate, $\dot{\alpha}$, and its pitch axis location, $a \in [-0.5, 0.5]$. The induced velocity varies linearly across the wing and this induces *virtual camber*, shown on the right of figure 2.3. Plunging motion is characterized by its plunge velocity, $\dot{h}$, and induces a constant change in angle of attack across the wing chord. Transverse gusts are characterized by their gust velocity profile, v_g, and also induce virtual camber as shown in figure 2.3. The overall quasi-steady lift coefficient in terms of the unsteady parameters is,

$$C_l = 2\pi \left(\alpha + \frac{\dot{h}}{U_\infty} + b\left(\frac{1}{2} - a\right)\frac{\dot{\alpha}}{U_\infty} + \int_0^\pi \frac{v_g(x)}{U_\infty}(\cos(\theta) - 1)\, d\theta \right). \tag{2.35}$$

Note that in this regime, the loads are still an algebraic function of the unsteady parameters and their instantaneous values fully define the instantaneous loads. In other words, no information about the history of the flow is necessary.

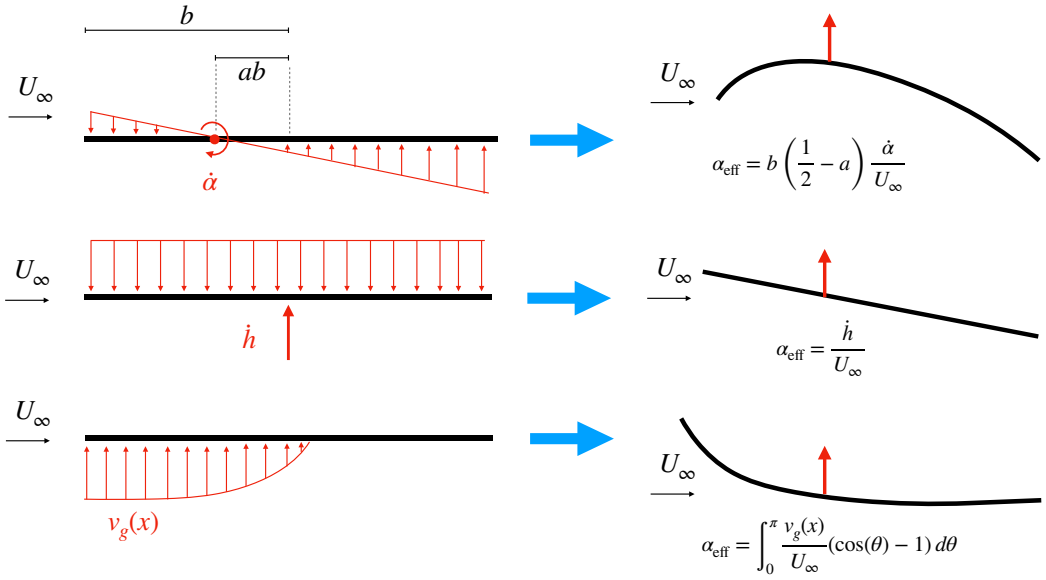

Figure 2.3: Schematic of the quasi-steady lift generation of wings in motion or wings exposed to gusts.

2.3.3 Unsteady circulatory loads

Flows with $k > 0.05$ are typically classified as fully unsteady [65]. In this regime, the influence of shed vorticity on the loads cannot be ignored. As a result, the instantaneous unsteady parameters no longer prescribe the instantaneous loads, and information about the history of the flow is necessary. Related to this is the fact that the use of the Kutta–Joukowski theorem is no longer appropriate. In the unsteady regime, the rates of change of circulations also appear in circulatory load components. To demonstrate this, consider a wing at some angle of attack, impulsively accelerated to a velocity U_∞ from rest. While the wing is at rest, the overall circulation of the flow

is 0. At some time instance after the wing has been accelerated, it has circulation Γ_b, which means that up to that point it must have shed vorticity with circulation $-\Gamma_b$ so that overall circulation is conserved. The simplest way to model this flow is to lump the bound vorticity to a single point vortex of strength Γ_b, and the wake vorticity to another point vortex of strength $-\Gamma_b$. The two point vortices are a distance d apart and are moving away from each other at velocity U_∞. The flow is depicted in figure 2.4. To compute the lift of this system we can evaluate the change in aerodynamic impulse described in section 2.1.3. Starting from equation (2.11), and recognizing that vorticity field of this flow is $\omega_z = \Gamma_b\delta(x_1) - \Gamma_b\delta(x_2)$, the change in aerodynamic impulse evaluates to,

$$L = -\rho\frac{\mathrm{d}}{\mathrm{d}t}\int_{V_f} x\omega_z \, dV \tag{2.36}$$

$$= -\rho\frac{\mathrm{d}}{\mathrm{d}t}\int_{V_f} x\Big(\Gamma_b\delta(x_1) - \Gamma_b\delta(x_2)\Big) \, dV \tag{2.37}$$

$$= \rho\frac{\mathrm{d}}{\mathrm{d}t}\Big(\Gamma_b d\Big) \tag{2.38}$$

$$= \rho U_\infty\Gamma_b + \rho d\dot{\Gamma}_b \tag{2.39}$$

The calculated lift of this two vortex system has a term equivalent to the steady Kutta–Joukowski lift but also a term proportional to the rate of change of circulation, $\dot{\Gamma}_b$ multiplied by the distance between the two vortices. Thus, for fully unsteady flows ($k > 0.05$), unsteady terms in the governing equations cannot be routinely neglected and the rates of change of flow circulations need to be accounted for.

When attempting to model more complex systems such as those discussed in section 2.2.4 and shown in figure 2.2c, the impulse of individual vortex sheets needs to be evaluated. For example, applying the integral (2.11) to a flow with a single

vortex sheet leads to,

$$L = -\rho \left(\int_{C_b} \frac{\mathrm{d}\gamma_b(s)}{\mathrm{d}t} s \, ds + \int_{C_b} \gamma_b(s) U(s) \, ds \right) \tag{2.40}$$

where $U(s)$ is the local streamwise velocity of the vortex sheet (not necessarily constant if the vortex sheet is deforming). The second integral is tied to the overall circulation of the vortex sheet. For example, for a rigid vortex sheet convecting at U_∞ it evaluates to $U_\infty \Gamma_b$, where Γ_b is the overall circulation of the vortex sheet. The first integral reflects the contribution of the rate of change of the local vortex sheet strength (the unsteady contribution). However, upon inspection of the term it is clear that a vortex sheet can generate forces even without any net circulation. That is, even if the total vortex sheet strength integrates to zero, $\Gamma_b = 0$, the time-dependent variation of the vortex sheet strength can still produce a non-zero force. These forces, referred to as non-circulatory forces, are explored further in the next section.

2.3.4 Non-circulatory loads

At high reduced frequencies $k > 0.05$, non-circulatory aerodynamic loads need to be accounted for along with unsteady circulatory loads. The terms non-circulatory loads and added-mass loads are often used interchangeably. "Added mass" refers to the effective mass of the fluid that must be accelerated along with the body during unsteady motion, leading to forces that scale with the body's acceleration. While the equivalence of added-mass and non-circulatory loads is true for many flows, in the context of gust encounter it is not accurate. Non-circulatory forces and moments arise from changes in the strength of the vortex sheet that do not contribute to the net circulation around the body. Following the seminal work of von Karman and Sears [105], the lift produced in unsteady aerodynamics can be decomposed into

three components: The quasi-steady lift, the added-mass lift (non-circulatory), and the lift due to the presence of the wake. The first component corresponds to the results of steady thin-airfoil theory, where wake vorticity is assumed to be infinitely far downstream of the wing. The second component corresponds to the vortex sheet that develops in order to enforce no flow through the wing during wing accelerations, and the last component corresponds to the vortex sheet that develops to counteract the downwash (or upwash) due to the wake. A paradox arises in the case of a gust encounter, as there is an added-mass force according to the definition of von Karman and Sears [105] but with no body accelerations. Corkery and Babinsky [19] showed that this force arises due to the change in the vortex sheet induced by the gust vorticity on the wing. In accordance with Kelvin's circulation theorem, all vorticity in the flow not shed by a body must sum to zero. Therefore, this induced vortex sheet must have no total circulation and is appropriately called 'non-circulatory'. It is worth noting that researchers have identified these vortex sheets even in the presence of flow separation and external vorticity [19, 22, 40]. In light of this evidence, in this dissertation we assume that non-circulatory effects approximately superimpose with circulatory effects. The quasi-steady lift and the lift due to the wake make up what is called circulatory lift, as they are associated with the build-up of bound circulation. Further discussion on the resolution of this apparent paradox for the general case of a body immersed in a viscous flow can be found in Limacher et al. [68].

It is possible to derive analytical expressions of non-circulatory forces for a variety of unsteady flows. For pitching and plunging thin-airfoils such as those shown in figure 2.3, the non-circulatory forces are

$$C_L^{NC} = \pi b \left(\frac{\dot{\alpha}}{U_\infty} + \frac{\ddot{h}}{U_\infty^2} - \frac{ba\,\ddot{\alpha}}{U_\infty^2} \right) \tag{2.41}$$

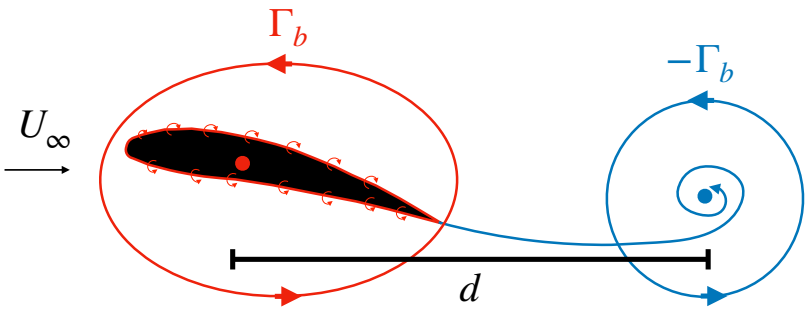

Figure 2.4: Schematic of the flow produced by an impulsively started wing.

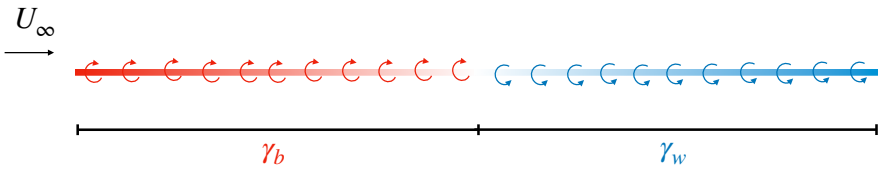

Figure 2.5: Schematic of an inviscid model for unsteady flows consisting of a bound vortex sheet and a wake vortex sheet.

where $\dot{\alpha}$, $\ddot{\alpha}$ and $\ddot{h}$ are the pitch rate and pitch acceleration, and plunge acceleration respectively, b is the semi-chord, and $a \in [-0.5, 0.5]$ is the non-dimensional pitch axis location. For gust encounters, no such simple expression exists for the non-circulatory loads, but we will discuss how it can be computed from Kussner's transverse gust model to be discussed in the next section.

2.3.5 Indicial response aerodynamics

Most unsteady aerodynamics flows evolve in ways that cannot be described analytically, and thus, general closed-form expressions do not exist for their load evolution. However, progress can be made making simplifications on the assumed generated flowfield. Classical unsteady aerodynamics theory uses a set of simplifying assumptions to derive analytic or semi-analytic expressions for the loads on a wing section. Typically, the wing is modeled as a thin airfoil with a vortex sheet placed on its cam-

ber line. The wake is also modeled as a vortex sheet starting at the trailing edge and is assumed to be flat and frozen in the flow. Using the above simplifying assumptions along with the enforcement of no flow through the wing, as well as the Kutta condition and Kelvin's circulation theorem, load coefficients can be derived as a function of the unsteady operating conditions and wing kinematics.

The theory of indicial aerodynamics is a framework used to describe the aerodynamic response of a lifting surface to sudden changes in flow conditions. By characterizing the time-dependent aerodynamic loads due to step inputs in angle of attack, gust velocity, or other perturbations, indicial aerodynamic models form the basis for understanding and predicting unsteady aerodynamic behavior in both canonical and complex flow scenarios. The formulation of indicial aerodynamic models involves several important assumptions and approximations:

- **Inviscid Flow**: The majority of models are derived under the assumption of inviscid flow, neglecting viscous effects to focus on the dominant unsteady aerodynamic phenomena.

- **Thin Airfoil Theory**: Indicial models are based on thin airfoil theory, which assumes small wing thickness, camber, and angle of attack.

- **Linearization**: Indicial models assume small perturbations, allowing the aerodynamic response to be described using linear theories. This simplification facilitates analytical solutions and integration into broader linear dynamical systems frameworks.

- **Flat wake**: Indicial response models assume a simplified wake to allow analytical tractability. In most theories, the wake is assumed to be flat and aligned with the freestream.

The linear nature of these models allows the use of superposition to predict the response to arbitrary time-dependent inputs by convolving the step response with the input history. Below is a description of some important unsteady aerodynamics models relevant to this dissertation.

Wagner's Model

Wagner's model Wagner [106] describes the time-dependent lift response of a thin airfoil to a sudden change in angle of attack, or more generally, to any step change in the quasi-steady bound circulation of an airfoil. The Wagner function, $\Phi(t)$, depicted in figure 2.6, captures the delayed build-up of lift due to the vorticity shed from the wing's trailing edge. Mathematically, the lift coefficient C_L is expressed as:

$$C_L(t) = 2\pi\alpha\Phi(t), \tag{2.42}$$

where α is the step change in angle of attack and $\Phi(t)$ is a function that asymptotically approaches unity as time progresses. Notably, its initial value is exactly half of its final value. This means that, at the moment of the step change, the wing generates half of the total lift it will ultimately achieve as time progresses.

Theodorsen's Model

Theodorsen's model extends Wagner's framework to harmonic oscillations in wing motion. Using a frequency-domain approach, Theodorsen developed a transfer function, $C(k)$, that relates the unsteady lift and moment to the motion of the airfoil:

$$C(k) = \frac{H_1^{(2)}(k)}{H_1^{(2)}(k) + iH_0^{(2)}(k)}, \tag{2.43}$$

where $H_n^{(2)}$ are Hankel functions of the second kind and k is the reduced frequency.

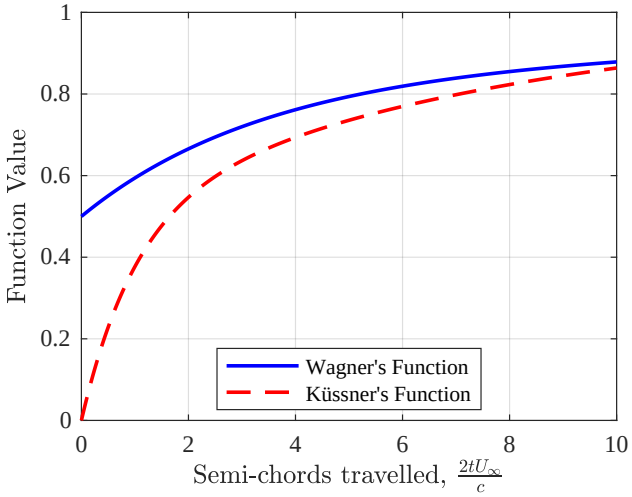

Figure 2.6: Comparison of Wagner's and Kussner's functions

The lift coefficient can then be written as,

$$C_L = \pi b \left(\frac{\dot{\alpha}}{U_\infty} + \frac{\ddot{h}}{U_\infty^2} - \frac{ba\,\ddot{\alpha}}{U_\infty^2} \right) + 2\pi C(k) \left[\frac{\dot{h}}{U_\infty} + \alpha + b\left(\frac{1}{2} - a\right) \frac{\dot{\alpha}}{U_\infty} \right]. \tag{2.44}$$

The first term in equation (2.44) represents the non-circulatory forces, while the second term represrents the circulatory forces. Notably, the circulatory forces are modulted by the transfer function $C(k)$, which introduces unsteady delay effects.

Küssner's Model

Küssner [59] used Wagner's result to to extend indicial response theory to transverse gusts. He modeled the wing as a broken-line airfoil, whose local angle of attack and quasi-steady bound circulation are computed from the gust velocity. The modeled flowfield is shown in figure 2.7. For a detailed derivation of Küssner's model the interested reader is pointed to Leishman [65, Chapter 8.1].

The Küssner function, $\Psi(t)$, plotted in figure 2.6, captures the gradual development of lift as an airfoil enters a sharp, transverse gust. The lift coefficient due to a

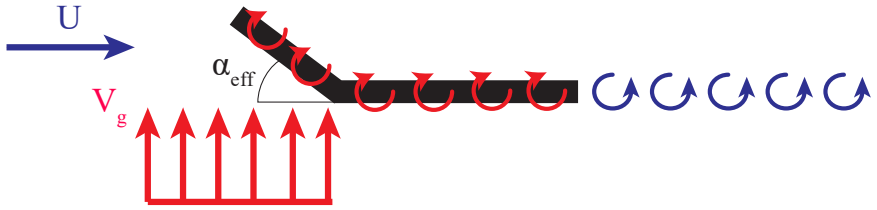

Figure 2.7: The flowfield in Küssner's gust encounter model. The wing and wake are represented as vortex sheets and the local angle of attack of the airfoil changes according to the local gust velocity V_g.

step gust of velocity V_g is given by:

$$C_L(t) = \frac{2\pi V_g}{U_\infty}\Psi(t) \tag{2.45}$$

where U_∞ is the freestream velocity. Like Wagner's function, $\Psi(t)$ approaches unity at steady-state, but unlike Wagner's function its initial value is zero.

2.3.6 Load decomposition

As discussed, the linearity of indicial aerodynamics models makes them particularly valuable for integration into linear dynamical systems frameworks. For example, lift responses to arbitrary gust profiles can be computed using a superposition integral with Kussner's function,

$$C_L(t) = \frac{2\pi}{U_\infty}\int_0^t \Psi(t-\tau)\frac{\mathrm{d}v_g(\tau)}{\mathrm{d}\tau}\,\mathrm{d}\tau \tag{2.46}$$

where $v_g(t)$ is the gust velocity at the leading-edge of the airfoil. This can be applied to realistic atmospheric gusts or gust generated in a laboratory for experimentation. Figure 2.8 displays time-averaged gust velocity profiles generated in the University of Maryland towing tank gust generator [96]. These profiles can be used as input into

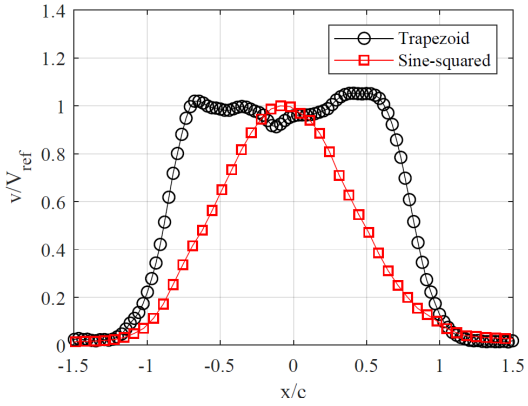

Figure 2.8: Time-averaged gust velocity profiles generated by the UMD towing tank gust generator. Figure obtained from Ref. [96] with permission.

this dynamical systems framework. The output is the lift response to each of these gust profiles.

As discussed earlier, the lift produced in unsteady aerodynamics can be decomposed into three components: The quasi-steady lift, the added-mass lift (non-circulatory), and the lift due to the presence of the wake von Karman and Sears [105]. Each of the lift contributions are shown figure 2.9 for a trapezoidal gust profile with gust width of 1.4 chords and a sine-squared gust profile with a gust width of 2.6 chords [96]. These forces have been obtained as part of this dissertation using unsteady vortex simulations which explicitly enforce the frozen wake and attached flow assumptions. Epps and Roesler [35] showed that this method accurately extracts the forces and circulations from classical unsteady theories, which often do not have closed-form time domain solutions. These forces are extracted numerically from the vortex model in the following way: At each timestep, the bound vorticity distribution can be determined by solving the linear system $A\Gamma = RHS$, where A is a matrix containing the influence coefficients of the bound vortices, Γ is a vector containing the circulation of the bound vortices, and RHS is a vector containing the induced velocities from the flowfield. The circulatory and non-circulatory bound vor-

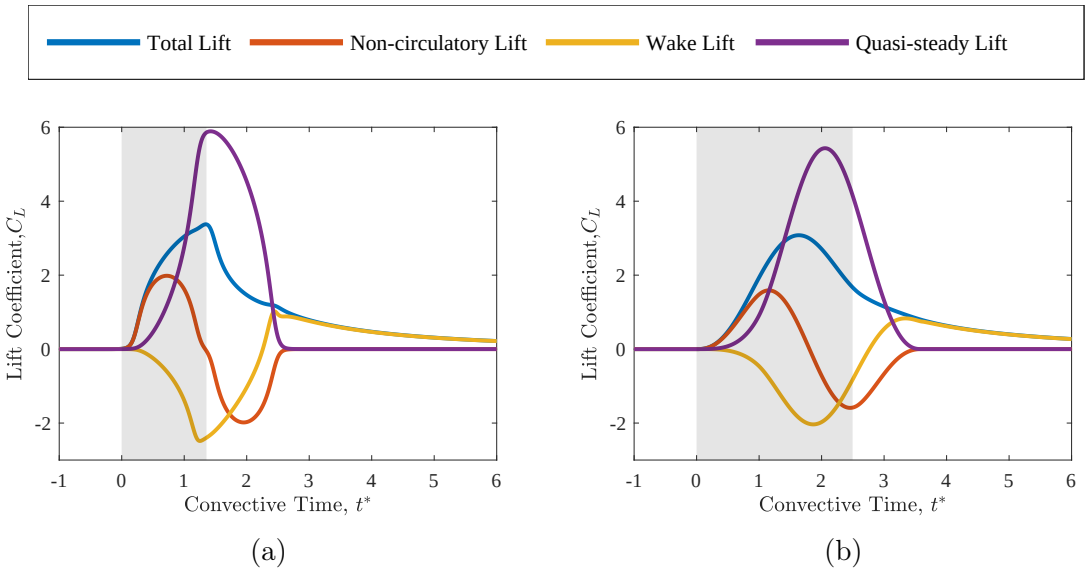

Figure 2.9: Lift decomposition in Küssner's model for (a) Trapezoidal gust profiles and (b) sine-squared gust profiles

ticity distributions are extracted by decomposing RHS into contributions from the shed vorticity and the gust, $RHS = RHS_{gust} + RHS_{shed}$, and then solving the two linear systems for Γ^{nc} and Γ^{c}. The corresponding circulatory and non-circulatory lift is then calculated using equation (2.11). The quasi-steady lift, L^{qs}, is obtained by integration of the effective angle of attack induced by the gust along the chord of the wing. The lift induced by the wake, L^{w}, is calculated by subtracting the quasi-steady lift from the total circulatory lift.

Figures 2.9a and 2.9b show that during the early phases of the gust encounter, most of the force is non-circulatory. As the effective angle of attack increases, the quasi-steady lift increases accordingly and there is a (delayed) build-up in bound circulation following Wagner's theory [106], which is balanced by opposite sign vorticity shed in the wake. This negative wake vorticity induces downwash on the wing and therefore has a negative contribution to the overall lift as shown in figure 2.9. Similarly, as the effective angle of attack decreases in the later stages of the gust encounter,

the quasi-steady bound circulation also decreases. Consequently, the vorticity that is shed in the wake is positive and induces upwash on the wing and therefore has a positive contribution to lift. This positive wake-induced lift is the sole contributor to lift after the gust exit and persists for several chord lengths in accordance with Wagner's indicial response.

2.4 Viscous flow physics

While the inviscid physics discussed in this chapter capture important characteristics of wing-gust encounters, they neglect viscous effects, which can be significant in certain cases. Notably, the formation of a leading-edge vortex (LEV) is only possible in the presence of viscosity and plays a critical role in large-amplitude gust encounters. In this section, we explore key characteristics of LEV flows and discuss their heuristic modeling.

2.4.1 Leading-edge vorticity flux

The seminal work of Didden [28] expressed the growth rate of a vortex by integrating the vorticity flux over the shear layer. By assuming a linear velocity profile across the shear layer, the vorticity can be approximated by,

$$\omega_z \approx \frac{\mathrm{d}u}{\mathrm{d}y} \approx \frac{\Delta U}{\delta} \tag{2.47}$$

where δ is the thickness of the shear layer feeding the vortex. Similarly, the size of the LEV can be approximated by the mass flux from the shear layer into the vortex. In this section we use these vorticity flux methods to predict the general scaling between LEV growth and the relevant transverse gust encounter parameters.

We follow the treatments of Widmann and Tropea [108] as well as other studies of unsteady aerodynamics flows [90, 92] The goal can be stated as follows: Given some fixed geometry, what are the effects of the experimental parameters such as Reynolds number and gust ratio on the leading-edge vortex.

The problem at hand is depicted in figure 2.10. A control volume can be drawn around the LEV, shown in figure 2.10a. The LEV circulation can be determined by integrating the fluxes on the boundary of the control volume. The LEV vorticity flux equation is derived in Eldredge and Jones [32] and in two dimenions it reads,

$$\frac{\mathrm{d}\Gamma}{\mathrm{d}t} = \int_B \omega_z \, \mathbf{u} \cdot \hat{\mathbf{n}} \, \mathrm{d}B + \int_B \nu \frac{\mathrm{d}\omega_z}{\mathrm{d}\hat{n}} \, \mathrm{d}B \tag{2.48}$$

where $\hat{\mathbf{n}}$ is the normal vector along B. The first term represents the convective flux and the second term represents the diffusive flux through the control volume boundary, B. All of the vorticity of the LEV originates from the leading edge shear layer and therefore the integral in equation (2.48) is only non-zero along the part of the control volume boundary intersecting the shear layer, C. Furthermore, as noted in [32] the diffusive flux is likely to be small when compared to the convective flux through the shear layer. Therefore the integral can be simplified to,

$$\frac{\mathrm{d}\Gamma}{\mathrm{d}t} = \int_C \omega_z \, \mathbf{u} \cdot \hat{\mathbf{n}} \, \mathrm{d}C \tag{2.49}$$

The angle of curve C is fixed by the effective angle of attack seen at the leading edge, α_{eff}, shown in figure 2.10b. Assuming a linear profile for the two velocity components across the shear layer, the vorticity can be written as the total velocity over the shear

layer thickness,

$$\omega_z = \left(\frac{\mathrm{d}u}{\mathrm{d}y} - \frac{\mathrm{d}v}{\mathrm{d}x}\right) \approx \left(\frac{\sqrt{U_\infty^2 + V^2}}{\delta}\right) \tag{2.50}$$

where V is the local vertical velocity induced by the gust. The assumptions stated above and shown in figure 2.10b imply that the velocity vector in the integral in equation (2.49) is always normal to curve C, i.e. $\mathbf{u} \cdot \hat{\mathbf{n}} = \sqrt{u^2 + v^2}$. Introducing a parametric variable $r \in [0, 1]$, the equation (2.49) can be written and evaluated as shown below,

$$\frac{\mathrm{d}\Gamma}{\mathrm{d}t} = \int_C \omega_z \, \mathbf{u} \cdot \hat{\mathbf{n}} \, \mathrm{d}C \tag{2.51}$$

$$\propto \int_0^1 \left(\frac{\sqrt{U_\infty^2 + V^2}}{\delta}\right) \sqrt{U_\infty^2 + V^2} \, r\delta \, \mathrm{d}r \tag{2.52}$$

$$\propto \frac{1}{2} U_\infty^2 (GR^2 + 1) \tag{2.53}$$

The proportionality symbol has been used to emphasize that this is not an exact relationship as the flow acceleration effects around the leading edge have been ignored. For example, Fage and Johansen [36], found that for an airfoil at a high angle of attack, the velocity of the shear layer, U_{SL}, is about 35-50% higher than the freestream velocity, depending on the angle of attack. Furthermore, induced velocities by the bound vorticity and LEV will also change the shear layer velocity. This will inevitably lead to errors, but the elementary scaling effects of the experimental parameters can still be captured. An identical calculation can be carried out for the size of the LEV

by integrating the mass flux across curve C.

$$\frac{\mathrm{d}A_{\mathrm{LEV}}}{\mathrm{d}t} = \int_C \mathbf{u} \cdot \hat{\mathbf{n}} \, \mathrm{d}C \tag{2.54}$$

$$\propto \int_0^1 \sqrt{U_\infty^2 + V^2} \, r\delta \, \mathrm{d}r \tag{2.55}$$

$$\propto \frac{\delta}{2} U_\infty \sqrt{GR^2 + 1} \tag{2.56}$$

This calculation shows that the LEV area has a direct dependence on the shear layer thickness, δ, a quantity not known a priori. Assuming that the vorticity in the shear layer originates at a stagnation point on the pressure side [76], and that the stagnation point flow is quasi-steady since the angle of incidence in a trapezoidal gust is approximately constant, the Hiemenz equations [49] can be used to approximate the thickness of the shear layer, as discussed in Widmann and Tropea [108] and Schlichting and Gersten [93]. This approximation is given by,

$$\delta = 2.4\sqrt{\frac{\nu}{a}} \tag{2.57}$$

where ν is the kinematic viscosity of the fluid and a is a parameter that describes the local flow curvature around the stagnation point on the pressure side, i.e., $a = U_\infty(x, y)/x = -V(x, y)/y$, with the origin of the coordinate system located at the stagnation point. a is proportional to U_∞, $a = a_0 U_\infty$, and equation (2.57) can then be written as,

$$\delta = 2.4\sqrt{\frac{\nu}{a_0 U_\infty}} \tag{2.58}$$

Equation (2.58) can be used in conjunction with equation (2.56) to predict the area growth of an LEV. In this dissertation, a steady vortex panel method was used to

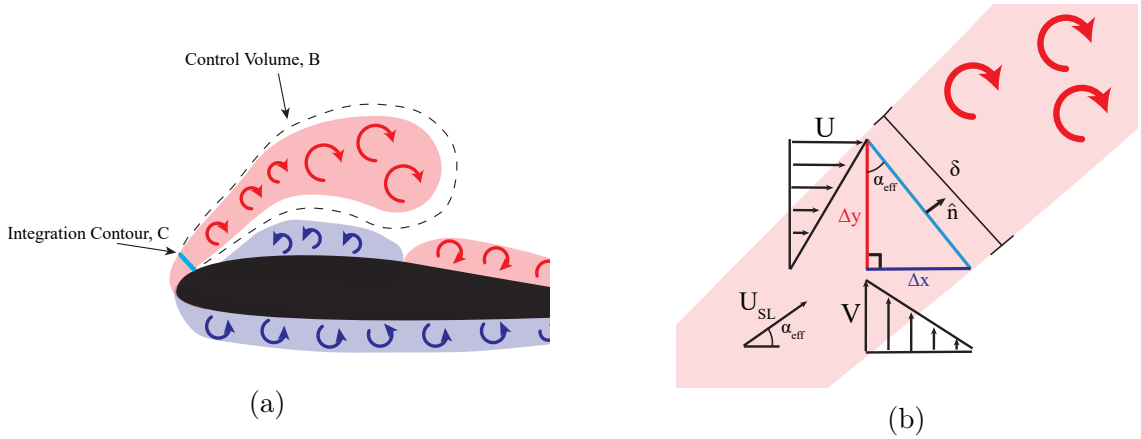

Figure 2.10: (a) Control volume analysis of LEV growth and (b) geometry of the problem after simplifying assumptions have been applied

compute the location of the stagnation point and the parameter a_0. It is found to be 1.67 and 2.59 for gust ratios 0.75 and 0.5, respectively. This method was also used in [108] to calculate a_0.

2.5 Chapter summary

In summary, this chapter explored the fundamental physics of unsteady aerodynamics, in the context of wing-gust encounters. The roles of vorticity, circulation, and aerodynamic impulse in the generation of unsteady forces was explored. Potential flow theory was presented and used to discuss inviscid, unsteady aerodynamics. This theory was then used to decompose unsteady loads in terms of its quasi-steady, circulatory, and non-circulatory components. Finally, the chapter highlighted the limitations of inviscid assumptions and introduced viscous effects, such as leading-edge vortex formation, to address more complex flow scenarios.

Chapter 3: Experimental methodology

This chapter describes the experimental methodology used in this dissertation. Key measurements were obtained using Particle Image Velocimetry (PIV) for flow visualization, load sensors for quantifying aerodynamic forces, and pressure transducers for surface pressure measurements. The chapter also details the characterization of gust profiles, instrumentation of wing models with embedded pressure sensors, and procedures for data synchronization and processing.

3.1 Towing tank facility

The experiments detailed in this dissertation were carried out using the University of Maryland's free surface water towing tank, pictured in figure 3.1a. This facility is 7 meters in length, 1.5 meters in width, and 1 meter in depth. Its design includes a steel framework with transparent glass walls, enabling optical access for particle image velocimetry (PIV).

The tank is equipped with a 4-degree-of-freedom motion control system, as shown in figure 3.1b, which supports streamwise, stream-normal, rotational, and pitching motions. The motor assembly consists of two independent parallel vertical brushless linear motors (H2W BLDC-04), responsible for pitching and plunging movements of the attached wing models. Out-of-phase motor actuation causes the model to pitch by changing its angle of attack. Conversely, in-phase motor actuation causes the model

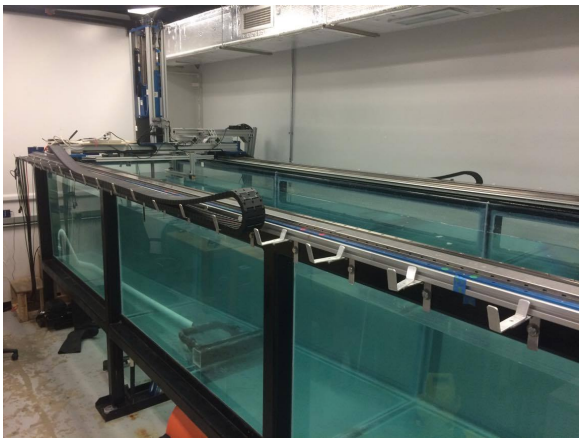

(a) Picture of the UMD STAL towing tank

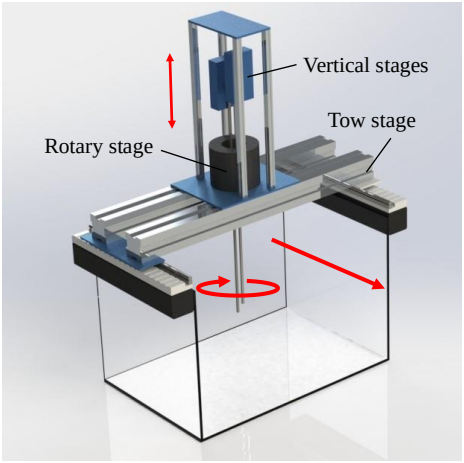

(b) Rendering of towing tank carriage

Figure 3.1: UMD STAL towing tank

to plunge. This plunging motion is often used to cancel any spurious pitch axis movement due to a change in angle of attack. The system also features a brushless rotary stage for continuous rotation and two brushless linear motors (H2W BLDC-08) that provide streamwise translation, generating the freestream velocity. The motion control is managed by a multi-axis Galil DMC 4153 controller and magnetic motor encoders.

3.2 Gust generator

In addition to standard aerodynamics testing hardware, gust encounter experiments require the use of a gust generation system. For transverse gust experimentation in a towing tank, a vertical jet must be created somewhere along the length of the tank. In the experiments of this dissertation, the gusting flow was created using the gust generator depicted in figure 3.2. This gust generator is driven by a variable-speed 1.85 HP Hayward centrifugal pump. The gust system circulates water through

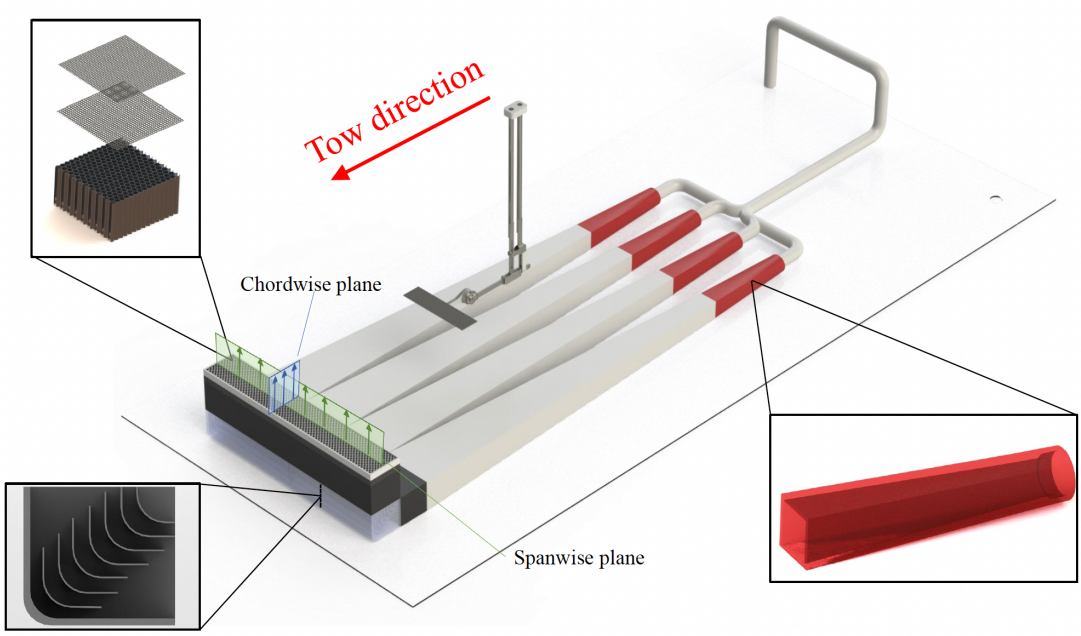

Figure 3.2: Rendering of the gust generator inside the STAL towing tank

a series of diffuser and turning sections that ultimately create a vertical gusting flow at the lengthwise center of the towing tank. The first part of the diffuser section, shown in red in figure 3.2, changes the cross-sectional shape of the flow from circular (matching the shape of the PVC piping) to rectangular (matching the shape of the gust outlet). The diffuser has a cone angle of 6°. After the flow has diffused to the gust outlet area (83.82x12.7 cm), it is turned by 90° by a set of turning vanes. The turning vanes radius is 2.54 cm and have a chord-to-vane-spacing ratio of 25%. Finally, the flow is conditioned through a honeycomb diffuser as well as a set of screens, depicted in figure 3.2. The honeycomb has a cell size of 3.18 cm and a cell length-to-width ratio of 8. The inner and outer screens were 16-mesh and 20-mesh, respectively.

3.3 Gust characterization

A gust characterization study was conducted to identify the shape and strength of the created gust. A static PIV setup was used to measure time-resolved gust velocities with varying pump RPM. The details of the static and tow PIV setup will be presented in section 3.4. For the gust characterization study, the field of view was centered 10 cm above the gust outlet, as shown in figure 3.3a. Figure 3.3b depicts gusting flow time-averaged, out-of-plane vorticity component and velocity vector field. The gusting flow is characterized by two shear layers that grow in size with increasing height. The gust profile is defined as the vertical velocity a body experiences as it goes through a gust. Figure 3.4 depicts gust profiles for 6 different pump RPMs. The profiles each start with near-quiescent flow on either side of the gust, and increase in strength in the shear regions. The region between the shear layers exhibits an almost constant velocity, which gives the gust its characteristic trapezoidal shape. The chordwise-averaged vertical velocity between the shear layers as a function of pump RPM is shown in figure 3.4b. The figure shows that the gust velocity increases linearly with pump RPM. Linear regression yields the relationship $V_g = 0.03(\text{RPM}/1000) - 0.007$, which can be used along with the prescribed tow velocity to determine the experiment gust ratio.

3.4 Particle Image Velocimetry and load measurements

This dissertation contains experimental data from two separate PIV and load measurement configurations. The two configurations are described in the following sections.

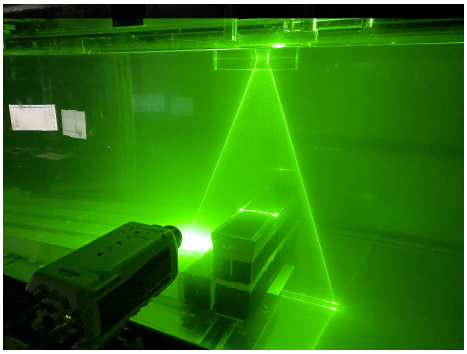

(a) Gust characterization PIV setup

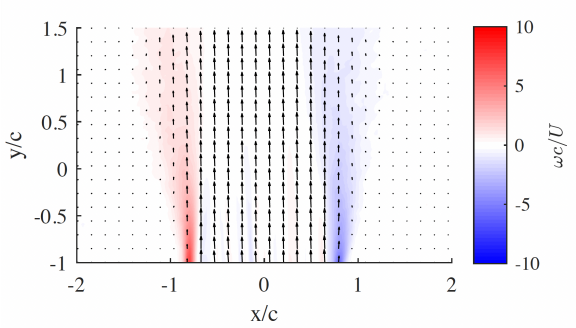

(b) Time-averaged, out-of-plane vorticity of the gusting flow.

Figure 3.3: Experimental setup and measurement of gust velocity

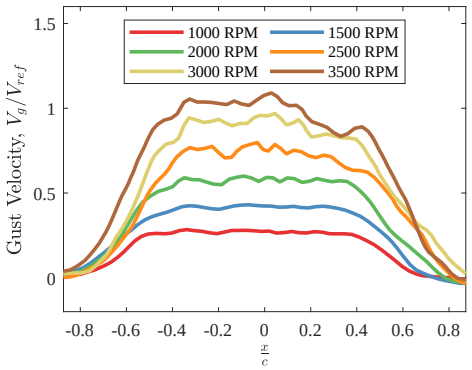

(a) Normalized gust velocity profiles for different pump RPMs.

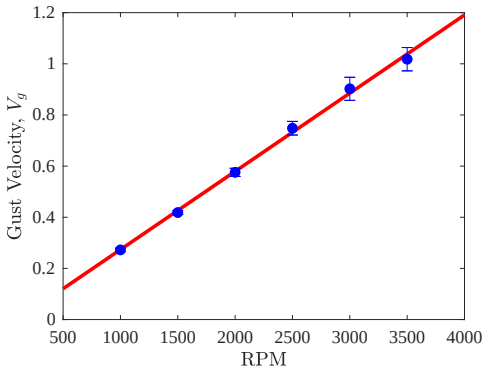

(b) Gust velocity as a function of pump RPM.

Figure 3.4: Gust profile and strength variation with pump RPM.

Table 3.1: Experimental test matrix

Gust Profile	Gust Ratio	Maximum Incidence	Reynolds Number
Trapezoidal	0.75	37°	6000, 12000
Trapezoidal	0.50	27°	12000, 17000
Trapezoidal	0.30	17°	12000, 28000
Trapezoidal	0.20	11°	12000, 42000

3.4.1 Configuration I: Static PIV

In the static PIV configuration, the camera, laser optics, and laser sheet were located off of the carriage, and were therefore fixed in the lab reference frame. This is depicted in a schematic in figure 3.6a, as well as in a picture in figure 3.7a. A Quantel Evergreen Nd:YAG 532 nm laser is located below the tank and its beam is redirected using a set of mirrors to a fixed structure mounted directly above the gust. On this structure, a pair of convex and concave lenses control the focus of the beam and a 45° powell lens creates the laser sheet depicted in figure 3.7a. The water tank was seeded with class IV soda lime spheres with 37 μm diameter and a Phantom v641 camera with 2560 x 1600 pixel resolution was used to capture images at 15 Hz in the laboratory reference frame.

In these experiments, the wing model used had a NACA0012-64 airfoil profile, with a chord of 10.5 cm and a span of 63 cm resulting in an aspect ratio of 6. The PIV plane was located 2.5 chords away from the wing tip of the model. The model was equipped with a 6-degree-of-freedom ATI Mini-40 force balance, depicted in figure 3.7a, that measured forces and moments at 1 kHz. Each experiment was repeated five times and all measurements were ensemble averaged, as well as filtered at a cutoff frequency of 5 Hz to remove structural vibrations in the 8-10 Hz range, as shown in figure 3.5

Table 3.1 summarizes the experiments used in this study. Two different Reynolds

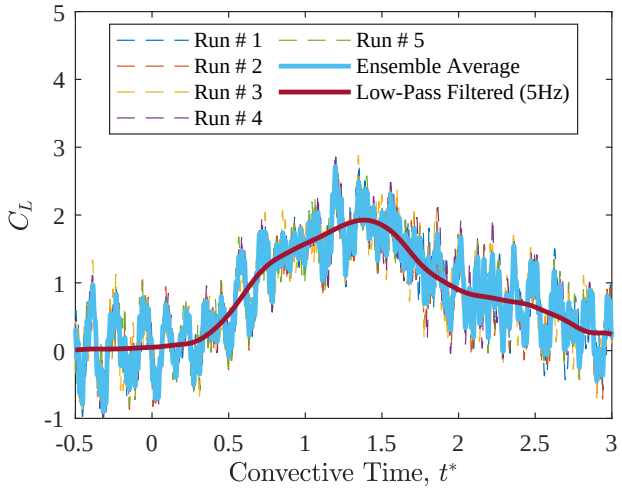

Figure 3.5: Example of an unfiltered, ensemble averaged, and low-pass filtered lift signal obtained using the ATI Mini-40 force balance.

numbers were tested at four gust ratios. The gust ratios were chosen to investigate two different regimes: A high gust ratio and a low gust ratio regime. All experiments were conducted at a geometric angle of attack of 0°. The effective angles of attack seen by the wing when fully immersed in gusts of gust ratios 0.75 and 0.5 are 37° and 27°, respectively. The effective angles of attack seen by the wing when the gust ratios are 0.3 and 0.2 are 17° and 11°, respectively.

3.4.2 Configuration II: Tow PIV

In the tow PIV configuration, the camera, laser optics, and laser sheet were towed with the carriage. This is depicted as schematic in figure 3.6b, and in a picture in figure 3.7b. A Photonics Industries Nd:YLF laser with a wavelength of 527 μm (DMX-30-527) is used to illuminate the neutrally buoyant class IV soda lime sphere tracer particles with a 37 μm diameter. The laser head was located beneath towing tank and the beam was redirected to an optical setup located on the towing tank carriage, as depicted in figuire 3.6b. The optical configuration used in these experiments was

similar to the one used in the static PIV experiments. A pair of convex and concave lenses and a powell lens were used to generate the laser sheet. An acryic block was placed at the air-water interface to avoid laser sheet reflection and diffraction.

The test article used in these experiments was a NACA0012 wing model with a chord of 115 mm and a span of 556 mm, resulting in an aspect ratio of 4.8. The wing model was equipped with a six-degree-of-freedom ATI Mini-40 force balance that measured forces and moments at 1 kHz. Both PIV and load experiments were repeated five times and the data was ensemble averaged to remove stochastic noise. The force measurements were also filtered at a cutoff frequency of 5 Hz to remove structural vibrations in the 8–10 Hz range. The gust experiments were carried out at a Reynolds number (defined as $\mathrm{Re} = U_\infty c/\nu$) of 10,000. The gust ratios, defined as $GR = V_g/U_\infty$, used in this study are $GR \in [0.25, 0.50, 0.75, 1.00]$.

3.5 Pressure sensor wing model

In this section we discuss the design choices and manufacturing of the pressure sensor instrumented model that was used in parallel with the models described in section 3.4. Following the design philosophy of [56], this work circumvents challenges in measuring surface pressures disuccused in section chapter 1 by embedding the pressure transducers directly below the model surface. While this eliminates the difficulties associated with tubing, it introduces other design restrictions. Namely, the sensors must be compact to fit inside the model, and also must measure absolute pressure using an internal vacuum, as access to a reference pressure would again require the use of tubing. Embedding sensors inside a model also results in long wiring distances. Towing tank motors produce a substantial amount of broadband electromagnetic interference (EMI) and long wiring carrying analog voltages exacerbates the noise in

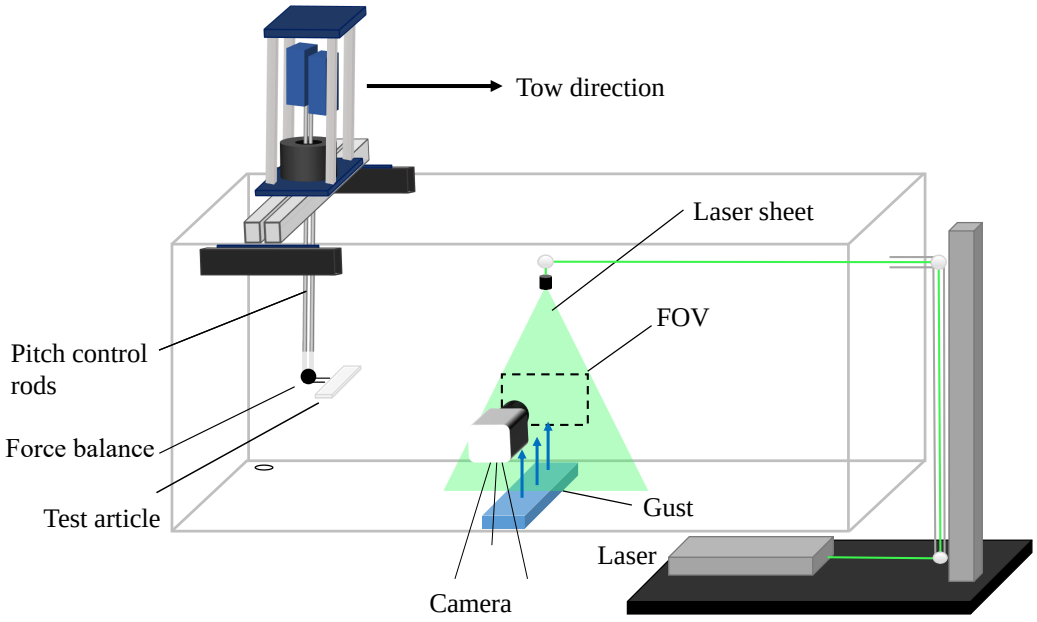

(a) Schematic of static PIV setup

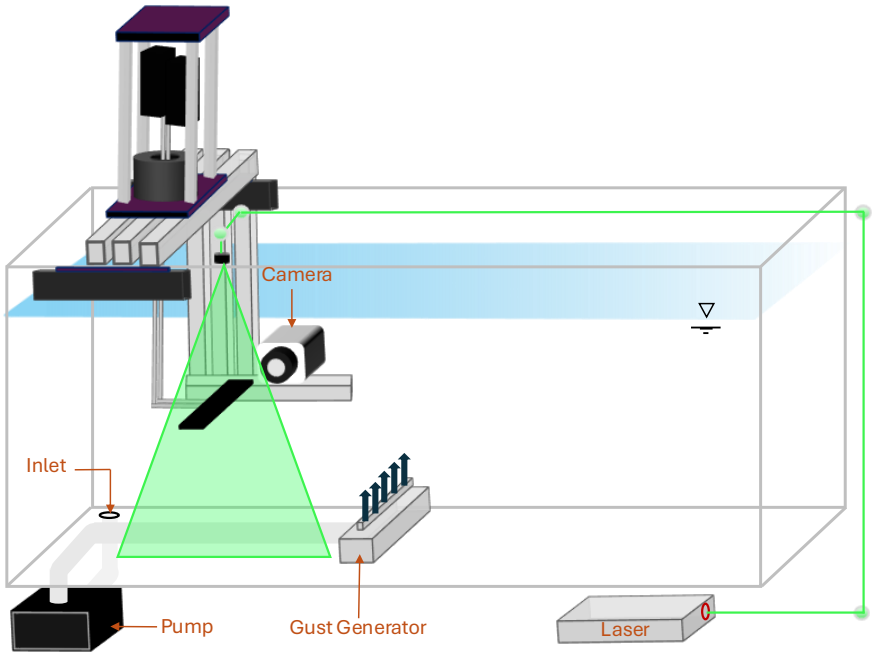

(b) Schematic of tow PIV setup

Figure 3.6: Two different PIV configuration used in this dissertation.

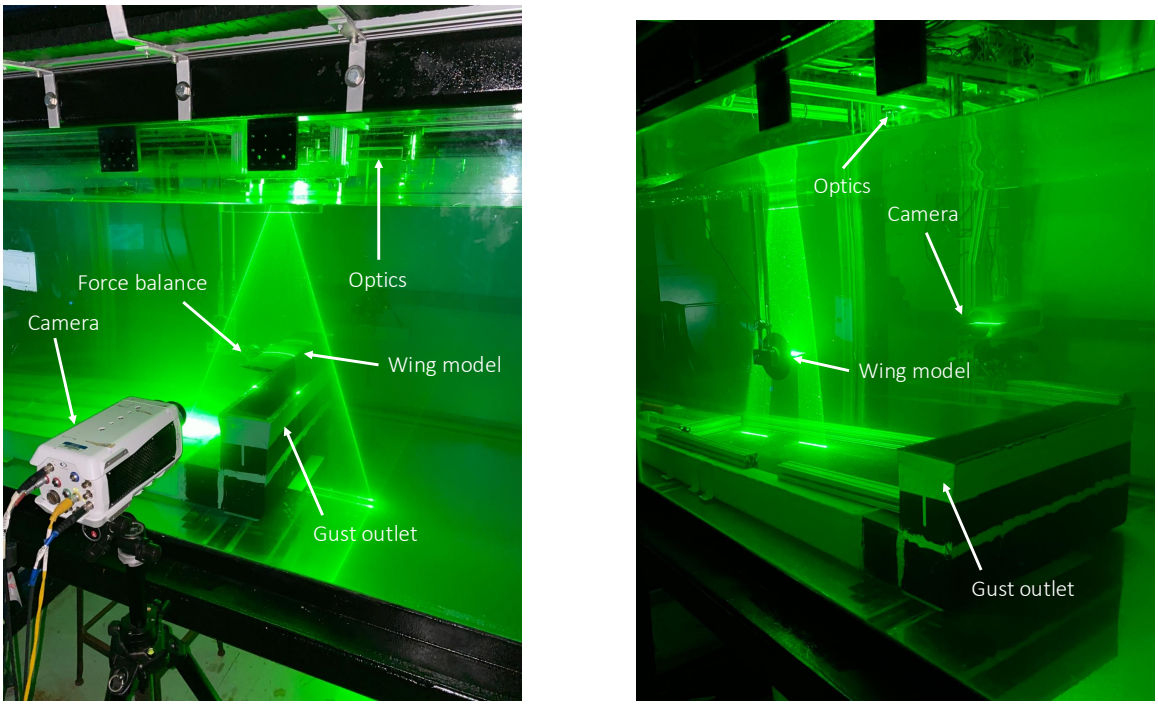

(a) Picture of static PIV setup

(b) Picture of tow PIV setup

Figure 3.7: Pictures of the two different PIV configuration used in this dissertation.

the signal. Thus, it is advantageous for the analog-to-digital conversion (ADC) of the pressure signal to take place physically close to the location of the measurement to minimize EMI.

Given these constraints, TE Connectivity's (TE) MS5837-02BA pressure sensor was selected for the measurements. The sensor is compact (3.3 x 3.3 x 2.75 mm), comes with an internal calibration, and uses an I2C communication protocol which directly outputs digital, temperature-compensated pressure. Its operating pressure range is 300-1200 mbar, with a $\pm$ 0.5 mbar accuracy. There are several drawbacks that accompany this family of sensors. In the context of experimental measurements, ADC chips located on the sensor limit the allowable sampling bandwidth. ADC conversion times for this sensor range from 0.54 to 16.44 ms, depending on the selected over-sampling rate (OSR), which after considering temperature compensation corresponds

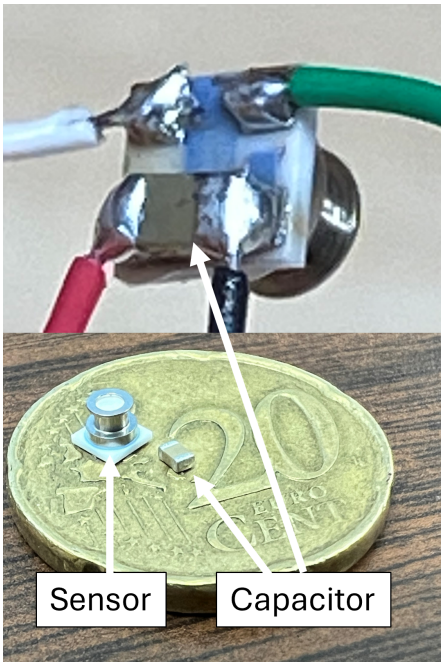

(a) A single MS5837 pressure sensor with the buffer capacitor displayed.

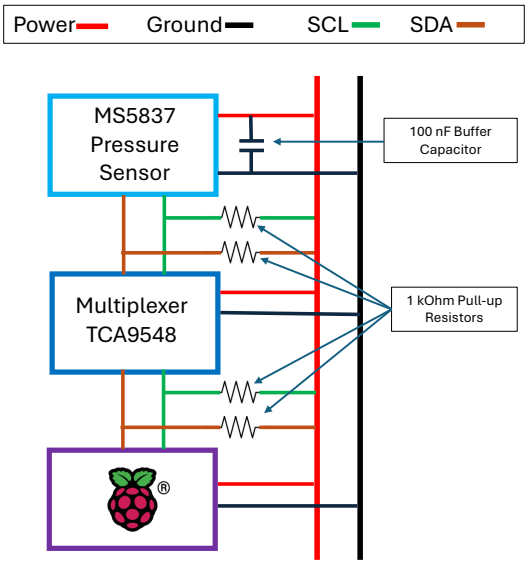

(b) Connection diagram for a single pressure sensor. SCL and SDA are the I2C clock and data lines, respectively.

Figure 3.8: Sensor soldering and wiring.

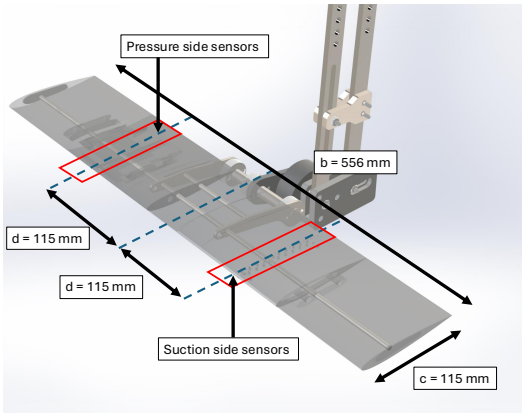

(a) Dimensions and pressure sensor locations for the instrumented model used in this study.

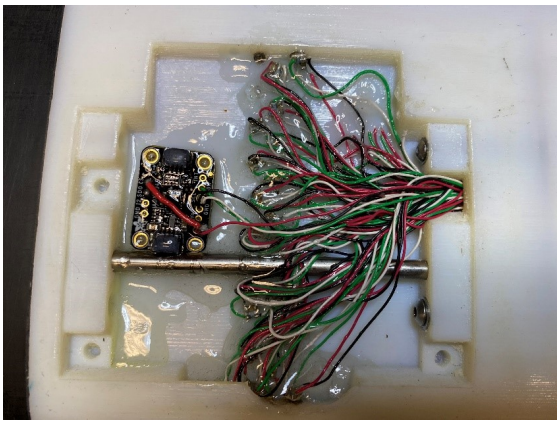

(b) One of the two sensor cavities of the instrumented model used in this study.

Figure 3.9: Embedded pressure sensor wing model design

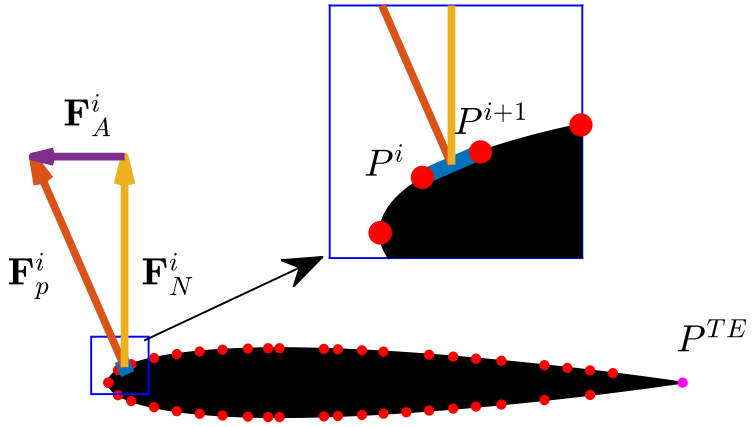

Figure 3.10: Schematic depicting a single panel for the pressure integration procedure as well as the resolves force components. The pressure sensor locations on the airfoil surface are also shown.

to sampling frequency of 900 to 30 Hz, respectively. Further, ADC chips require a stable voltage supply during the conversion cycle. In practice, this limits the wiring distance from the power source to the sensor to approximately 0.3 m. We found that this restriction can be relaxed if the voltage supply is stabilized near the sensor by using a buffer capacitor, which connects the power and ground channels on the sensor as shown in figure 3.8a. A buffer capacitance of 100 nF was found to remove most AC noise from the 3.3 V DC supply voltage and extended I2C communication to at least 2 m. The choice of pull-up resistors on the I2C data (SDA) and clock (SCL) lines also affects the allowable sampling rate. Pull-up resistors restore the digital line voltage to the supplied value (3.3 V in this case) when the sensor switch connected to ground is off. It is typically recommended to use high pull-up resistances to minimize power consumption when the digital signal line is high. However, a large pull-up resistance increases the line rise time and thus limits the communication bandwidth.

In the context of experimental measurements, power consumption is usually not a concern and it is recommended to decrease the pull-up resistance as much as possible to decrease signal rise time and allow higher communication baudrates. A pull-up resistance of 1 kΩ was used in this system. A custom data acquisition board was developed and used during the towing tank experiments. The board consists of a Raspberry Pi 4 Model B computer module, 6 TCA9548 multiplexers to handle I2C address conflicts, a 3.3 V power supply and digital IO connectors for the sensors. A connection diagram for a single sensor is shown in figure 3.8b. An oversampling rate of 2048 was found give the best balance between signal-to-noise ratio and time resolution. With 42 sensors, the overall sampling frequency of the system was 120 Hz.

A wing model identical in dimensions with the one described in section 3.4, was constructed of Vera family photopolymers using the Stratasys Objet500 Connex3 3D printer. The model was retrofitted with a total of 48 pressure sensors – 24 sensors on one side, 1 chord away from the centerline and 24 symmetrically on the other, as shown in figure 3.9a. For manufacturing purposes, each side houses either only top side or bottom side sensors. Thus, the top and bottom sensors can only be considered to be on the same wing section for flows that are symmetric about the centerline. The sensor chips were covered with epoxy and silicon for waterproofing, as depicted in figure 3.9b, while the sensor pressure port was exposed to the flow through pressure taps. 42 of the 48 installed sensors were found to operate nominally across all of the experiments conducted for this dissertation. For consistency, only data from these sensors are presented for all the experiments. Their locations on the surface are shown in figure 3.10 and listed in table 3.2.

Sensor #	1	2	3	4	5	6	7	8	9	10	11	12	13	14
x-coordinate	0.0000	0.0167	0.0397	0.0795	0.1192	0.1589	0.1987	0.2428	0.2781	0.2980	0.3753	0.3996	0.4415	0.4790
y-coordinate	0.0000	0.0220	0.0320	0.0427	0.0497	0.0543	0.0573	0.0592	0.0599	0.0600	0.0588	0.0581	0.0563	0.0540

Sensor #	15	16	17	18	19	20	21	22	23	24	25	26	27	28
x-coordinate	0.5585	0.6004	0.6402	0.6843	0.7594	0.7991	0.8389	0.8786	0.0167	0.0397	0.0795	0.1192	0.1589	0.1987
y-coordinate	0.0486	0.0453	0.0418	0.0381	0.0304	0.0256	0.0214	0.0165	-0.0220	-0.0320	-0.0427	-0.0497	-0.0543	-0.0573

Sensor #	29	30	31	32	33	34	35	36	37	38	39	40	41	42
x-coordinate	0.2428	0.2781	0.2980	0.3753	0.3996	0.4415	0.4790	0.5188	0.5585	0.6004	0.6402	0.6843	0.7594	0.8389
y-coordinate	-0.0592	-0.0599	-0.0600	-0.0588	-0.0581	-0.0563	-0.0540	-0.0517	-0.0486	-0.0453	-0.0418	-0.0381	-0.0304	-0.0214

Table 3.2: Locations of the pressure sensors on the airfoil's surface

3.6 Measurement uncertainty and error propagation

The PIV raw images are processed using LaVision's DaVis 8.4 software, employing a multi-pass cross-correlation technique. The processing begins with three passes using a 48×48 pixel square interrogation window with 50% overlap. For wing-gust encounter cases, a 24×24 pixel auto-adaptive interrogation window with 75% overlap is applied. The uncertainty of the PIV vector fields acquired in section 3.4 was quantified using a built-in DaVis error tool that uses correlation statistics to construct an error estimate [109]. For the static PIV experiments, the maximum uncertainty in the velocity field was found to be 3.6% and the average error was about 1%, while for the tow PIV experiments, the maximum uncertainty in the velocity field was found to be 6.6% and the average error was about 3.5%. The error on the force measurements was estimated based on the ensemble statistics of the experiments. The maximum standard deviation was found to be approximately 7% of the ensemble mean.

Errors in individual pressure measurements are estimated by collecting time-series data from each sensor at the specified oversampling rate and analyzing its statistics. These standard deviations are then added to the ensemble standard deviations, in the sum of squares sense. Uncertainty in derived quantities such as lift from pressure integration are estimated using linear uncertainty propagation, discussed in [94]. An example computation for lift proceeds as follows: The lift is written as a function of

the pressure measurements, $L = F(P_i) = \sum_i k_i P_i$, where k_i contains the effects of scaling and projecting the measurement in the lift direction as discussed in section 3.7.3. The variance in the derived measurement can then be written as,

$$\begin{aligned}\sigma_L^2 &= \sum_{i=1}^{N} \left(\frac{\partial F}{\partial P_i}\right) \sigma_{P_i}^2 + 2 \sum_{i=1}^{N-1} \sum_{j=i+1}^{N} \frac{\partial F}{\partial P_i} \frac{\partial F}{\partial P_j} \rho(P_i, P_j) \sigma_{P_i}^2 \sigma_{P_j}^2 \\ &= \sum_{i}^{N} k_i \sigma_{P_i}^2 + 2 \sum_{i=1}^{N-1} \sum_{j=i+1}^{N} k_i k_j \rho(P_i, P_j) \sigma_{P_i}^2 \sigma_{P_j}^2 \end{aligned} \tag{3.1}$$

where $\rho(P_i, P_j)$ is the cross correlation between pressure measurements and σ_{P_i} are the standard deviations of the individual pressure measurements. Since measured pressure scales with the dynamic pressure of each experiment, errors are found to be strongly related to the experiment tow velocity, U_∞. For a tow velocity of 0.5 m/s, the average error is less than 1%, while for a tow velocity of 0.1 m/s the average error is found to be approximately 10%. Error bars based on these estimates are displayed where possible.

3.7 Data postprocessing and analysis

3.7.1 Data synchronization and taring

The analysis presented in this dissertation requires synchronization of the load, pressure and flowfield data. The sensors also need to be tared so that irrelevant forces and pressures due to gravity and sensor drift are eliminated. Figure 3.11a shows the model pitch angle and height as a function of the experiment time, and figure 3.11b shows the pressure at the leading edge as well as the lift coefficient history over the same time period. In the first 6 seconds of the experiment, labeled sensor synchronization period, the model is aggressively raised to a height of 40 mm and

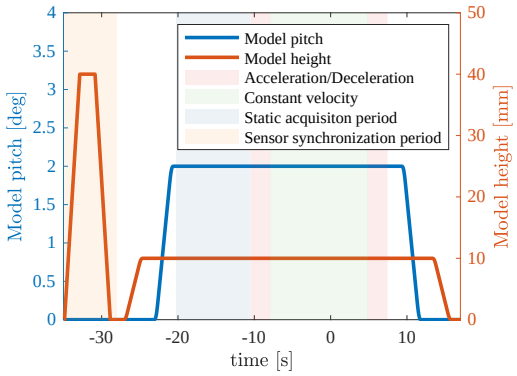

(a) Model pitch angle and tow height for the duration of an experiment.

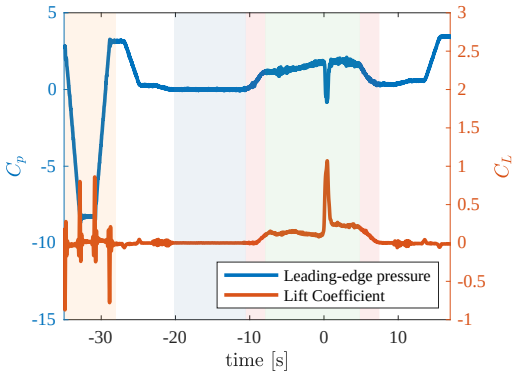

(b) Synchronized and tared pressure and lift coefficients.

Figure 3.11: Kinematics, measurements and phases of an example experimental run.

in the same manner brought back down. The creates 4 large lift spikes as well a hydrostatic pressure jump, as shown in figure 3.11b. The corresponding responses of the sensors can then be used to synchronize the measurements to the commanded kinematic profile.

Following this synchronization, the model is then brought to the height and angle of attack that the experiment will be conducted in. A 10 second window called the static acquisition period follows. During this time the model is completely stationary. Time-averaging of the loads and pressures during this window provides a measure of the bias of the sensors. This bias can then be subtracted from the measurement to ensure that the reading of the sensors are 0 before the experiment. The data in figure 3.11b has already been de-biased, hence, the lift and pressure during the static acquisition period is 0.

The model is then accelerated to the experiment tow velocity. A period of constant velocity follows and in this case a gust encounter takes place at $t = 0$. The model is then decelerated and the experiment ends.

3.7.2 Isolation of aerodynamic pressure

There are several pressure contributions that must be subtracted from the raw signal in order to isolate the purely hydrodynamic contribution of interest. Pressure data is presented in terms of pressure coefficient defined as,

$$C_p = \frac{P - P_\infty}{\frac{1}{2}\rho U_\infty^2}$$

where U_∞ is the freestream velocity and P_∞ is the far-field static pressure. A consequence of the taring procedure presented in section 3.7 is that the initial P_∞ is subtracted out during de-biasing. Thus, if the far-field static pressure remains constant for the duration of the experiment, the remaining pressure divided by the dynamic pressure would return the pressure coefficient of interest. However, if the towing tank is not perfectly level everywhere along its length, the hydrostatic pressure seen from the sensors will vary, as the wing will not be moving parallel to the free surface. Thus, the farfield static pressure would also be changing. This effect can be seen in the measured pressure of figure 3.11b. After the model is accelerated to the experiment tow velocity, the measured pressure continues to increase and begins decreasing a few seconds before the deceleration period. Experiments at different tow velocities verified that this contribution to pressure is indeed hydrostatic, since the magnitude of the bias is the same across all experiments when plotted as a function of tow position.

To isolate this component, a hydrostatic tare run was performed at the beginning each experimental campaign, where the wing was placed at 40 locations along the length of the tank, and the pressures were again averaged over a 10 second window. This created a hydrostatic bias as a function of tow position which was used to

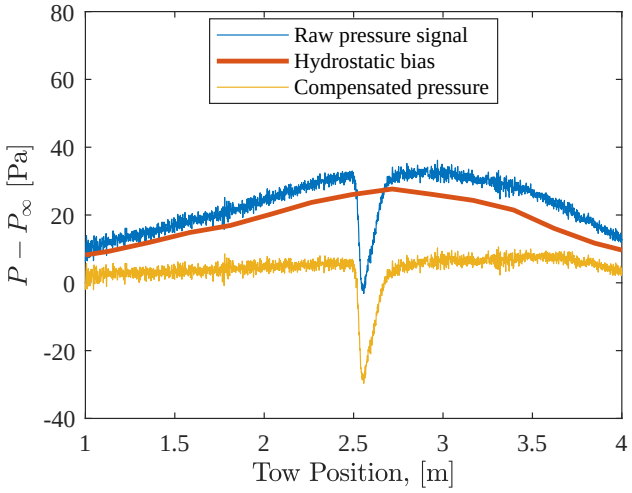

Figure 3.12: An example of how bias induced from a spatially varying hydrostatic pressure is removed from the pressure signal.

compensate the signal during postproccessing as shown in figure 3.12 for a single sensor

3.7.3 Pressure integration

In this study, surface pressure distributions are integrated to recover instantaneous pressure loads. A panel integration procedure is used, where the airfoil surface is discretized into panels that have pressure sensors on their edges, as shown in figure 3.10. Each panel is assumed to have a linear pressure distribution, varying between the measured pressures on its edges, P^i, P^{i+1}. Thus, the pressure force on each panel, $\mathbf{F}_p^i$, can be computed as,

$$\mathbf{F}_p^i = d_i \frac{P_i + P_{i+1}}{2} \hat{\mathbf{n}}_i$$

where d_i and $\hat{\mathbf{n}}_i$ are the length and normal vector of the ith panel, respectively. These forces can then be resolved into wing-normal and wing-axial components, $\mathbf{F}_N^i, \mathbf{F}_A^i$,

for each panel i, and then added to recover the total wing-normal and wing-axial pressure loads. To capture wing loading near the trailing edge, a fictitious pressure measurement is added at the trailing edge by linearly extrapolating and averaging the pressure and suction side pressure distributions. This creates a derived measurement, P^{TE}, which is used in the panel method described above. The overall loads were found to be insensitive to the inclusion of this trailing edge pressure, typically only contributing less than 1% to the total.

3.7.4 Vortex tracking

An objective method of vortex boundary, centroid and circulation identification is of interest in this paper as the properties of the LEV will be compared between different experiments. The vorticity field obtained from the PIV velocity vector field is useful in visually identifying vortex structures. However, when used in an algorithm vorticity fails to differentiate between distinct (but close in proximity) flow features such as a vortex and a shear layer. Furthermore, in flows with high ambient vorticity such as those of a gust, vortices of strength greater than that of the LEV can appear in the flow which further hinders the vortex identification process. In this work, an algorithm based on the vortex identification method proposed by Graftieaux et al. [44] is used. Graftieaux et al. [44] introduced two scalar functions, Γ_1 and Γ_2 which are derived directly from the PIV velocity field. Typically, Γ_1 is used to identify the vortex core and Γ_2 is used to identify the vortex boundary. For each point in the flowfield a circular window with radius R around that point is used to compute the

Γ_1 and Γ_2 fields, which are defined as follows

$$\Gamma_1(\mathbf{x}) = \frac{1}{N}\sum_{i=1}^{N}\frac{((\mathbf{x}-\mathbf{x}_i)\times\mathbf{u}_i)\cdot\hat{n}}{||\mathbf{x}-\mathbf{x}_i||\cdot||\mathbf{u}_i||} \tag{3.2}$$

$$\Gamma_2(\mathbf{x}) = \frac{1}{N}\sum_{i=1}^{N}\frac{((\mathbf{x}-\mathbf{x}_i)\times(\mathbf{u}_i-\mathbf{u}_{avg}))\cdot\hat{n}}{||\mathbf{x}-\mathbf{x}_i||\cdot||\mathbf{u}_i-\mathbf{u}_{avg}||} \tag{3.3}$$

where $\mathbf{x}$ is a position vector in the flowfield, $\mathbf{u}$ is a velocity vector, N is the number of vectors in the circle of radius R, $\mathbf{u}_{avg}$ is the average velocity within the circle, and $\hat{n}$ is the unit-normal vector in the z direction. Typically, vortex centers have Γ_1 values greater than 0.9 and vortices have Γ_2 values greater than $2/\pi$. Therefore, any Γ values that do not meet either criteria are set to 0. Although LEVs do not necessarily have the most vorticity in the flow, it is empirically found that they are the most coherent and have the biggest cluster of valid Γ_1 values at their vortex core. Therefore an outlier remover algorithm is applied to the Γ_1 field and the remaining valid Γ_1 positions in the flow undergo a vorticity-weighted average to determine the unique location of the LEV centroid. The valid Γ_2 values are then divided into different structures based on their connectivity (effectively giving all the vortices in the flow) and only the one with the previously identified LEV centroid within its boundary is kept and identified as the LEV. This procedure is found to be very robust. In the rare cases where it fails, a polygon is drawn manually around the LEV and the centroid is identified again through a vorticity-weighted average. Figure 3.13 shows examples of identified LEV boundaries on top of contours of vorticity. The circulation of the LEV is then found using Stokes' Theorem on the vorticity field inside the LEV boundary. The error in the vortex tracking algorithm was estimated by manually identifying the LEV boundary and centroid for a whole test case. When the algorithm was successful at finding the LEV, the average error of the LEV properties was found to be 5% and

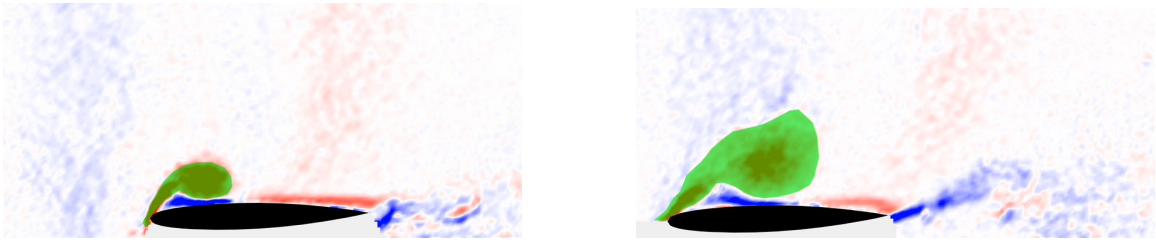

(a) (b)

Figure 3.13: Examples of LEV tracking during a gust encounter suing the Γ_1-Γ_2 algorithm

the maximum error was 8%.

3.7.5 Finite wing effects

The pressure integration procedure described in section 3.7.3 recovers the sectional load coefficients at the measurement section. These differ from the overall model load coefficients, which can be determined if the spanwise load distributions are known. For unsteady flows, these distributions are related to the transient evolution of the tip vortices, which is a difficult problem and an active area of research [15, 69]. We can obtain insight into this expected error by using the lift distributions for steady flows, which are well understood and can be computed using lifting-line methods [3, 73]. Specifically, we seek to use lifting-line analysis to express the overall lift coefficient of the wing, given a sectional lift coefficient at a prescribed location. Since we are interested in high incidence flows, we present a nonlinear variant of the lifting-line problem, which accounts for decay of the lift slope at high angles of attack, as well as the post-stall lift drop off. This is done through the use of 2D lift data, which can be obtained through experiment or simulation. Here, they are calculated using the XFOIL airfoil analysis tool, which has been shown capture the important steady pressure distribution and load characteristics of airfoils in this regime [29, 75].

The lifting-line algorithm presented here is a Fourier domain version of the one

discussed in Anderson Jr et al. [4], and proceeds as follows: An initial spanwise circulation distribution is assumed and decomposed into a sine Fourier series. We make use of the transformation $y = -\frac{b}{2}\cos(\theta)$, where b is the span of the wing, y is the length along the span and θ ranges from $0 < \theta < \pi$. Thus, $\Gamma(\theta) = 2bU_\infty \sum_n A_n \sin(n\theta)$, where the Fourier coefficients, A_n, can be computed as,

$$A_n = \frac{1}{\pi b U_\infty} \int_0^\pi \Gamma(\theta) \sin(n\theta) \mathrm{d}\theta \tag{3.4}$$

Given this distribution, the induced angle of attack distribution is determined as,

$$\alpha_i(\theta) = \frac{1}{4\pi U_\infty} \int_{-b/2}^{b/2} \frac{(\mathrm{d}\Gamma/\mathrm{d}y)}{y - y_0} \mathrm{d}y_0 \tag{3.5}$$

$$= \sum_{n=1}^{N} n A_n \frac{\sin(n\theta)}{\sin(\theta)} \tag{3.6}$$

A new circulation distribution can be then computed using the Kutta–Joukowski theorem and the 2D lift data as,

$$\Gamma(\theta) = \frac{c(\theta) U_\infty C_l(\alpha(\theta) - \alpha_i(\theta))}{2} \tag{3.7}$$

where $\alpha(\theta)$ is the spanwise geometric angle of attack distribution and $c(\theta)$ is the spanwise chord distribution, which effectively specifies the planform shape. The process then repeats until $\Gamma(\theta)$ converges.

Figure 3.14 depicts computed normalized circulation distributions for three cases: A wing with an elliptical planform at $\alpha = 5^\circ$, a rectangular wing at the same angle of attack with dimensions identical to those used in the present experiments, and the same rectangular wing but now at a post-stall angle of attack of 13°. The plot also depicts the pressure measurement section at $y^*/b \approx 0.2$. The analysis suggests that

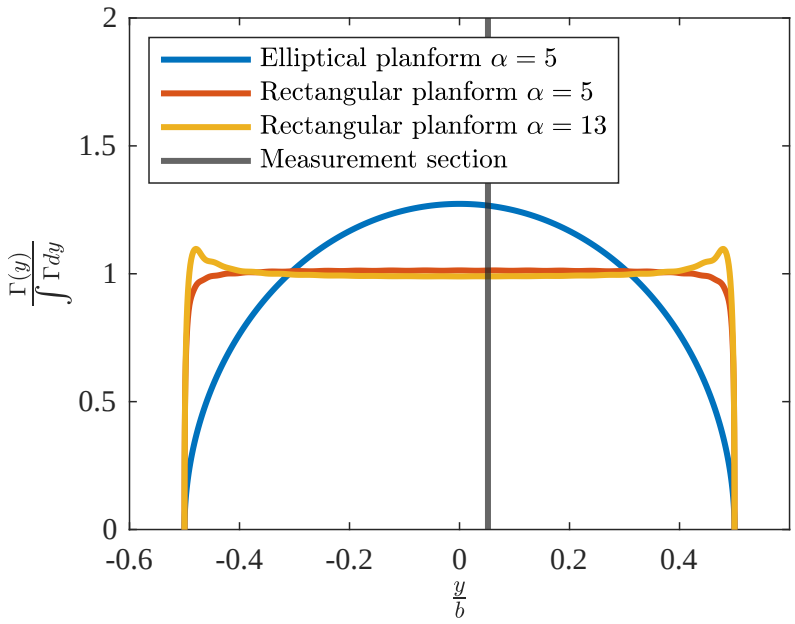

Figure 3.14: Converged spanwise circulation distributions from the lifting-line analysis described in 3.7.5.

for an elliptical planform, the sectional lift would be 16% higher than the overall lift. In contrast, for a rectangular planform, the lift is only 1% higher than the overall lift, due to the inefficient, yet flat pressure distribution produced by rectangular planforms. This analysis shows that for attached flows it is expected that the sectional lift will be close to the overall lift. For post-stall angles of attack, the induced angle of attack near the wingtips causes the flow to reattach, resulting in higher lift near the wing tips, as depicted in figure 3.14. Thus, for post-stall angles of attack, wing sections near the tips have higher loading than the rest of the planform. This effect, along with lift induced by the tip vortex itself, have been the subject of recent investigations for low aspect ratio wings, and are a likely source of systematic error in this study for post-stall angles of attack [26, 69].

3.8 Chapter summary

This chapter detailed the experimental methodology used in this dissertation to investigate wing-gust encounters. Key components included the UMD towing tank, gust generator, and motion control systems. Measurement techniques such as PIV and load sensing and pressure measurements were described alongside procedures for gust characterization, pressure integration, vortex tracking, and data synchronization. The chapter also addressed uncertainty analysis and finite-wing effects to ensure accuracy and reliability in the experimental results.

Chapter 4 utilizes the static PIV setup and model. Chapters 5 and 6 employ the tow PIV setup and instrumented wing model, providing synchronized flowfield, pressure, and force data to investigate dynamic interactions during wing-gust encounters.

Chapter 4: Evaluation of linear gust-encounter dynamics

This chapter presents and analyzes flowfields, lift transients explores how the vorticity distributions shed from a wing's leading and trailing edges affect its lift history during a large-amplitude transverse gust encounter. Flowfields and lift transients of blunt-edged wings encountering gusts are studied at different Reynolds numbers and gust ratios. Emphasis is placed on comparing experimental lift transients and vorticity distributions with those predicted by Küssner's transverse gust model.

4.1 Flow morphology and Reynolds number effects

This section presents the general flow evolution characteristics, as well a comparison between the experimental force transients and those predicted by Küssner's model. The effects of Reynolds number on the flow and loads are also briefly explored, as previous Reynolds number independence results have only been demonstrated for flat plate wings [20, 45, 83]. The low gust ratio regime consists of gust ratios 0.2 and 0.3 and the high gust ratio regime consists of gust ratios 0.5 and 0.75. Each gust ratio is repeated at a different Reynolds number as shown in table 3.1. For brevity, flowfields only for $GR = 0.3$ and $GR = 0.75$ are presented.

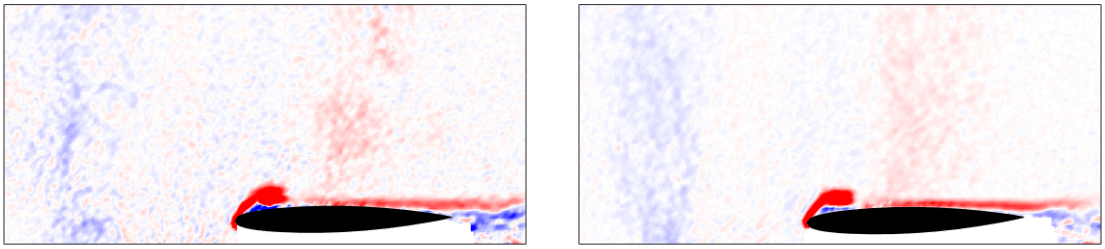

(a) $\frac{tU_\infty}{c} = 0.50,\ GR = 0.75,\ Re = 6000$

(b) $\frac{tU_\infty}{c} = 0.50,\ GR = 0.75,\ Re = 12000$

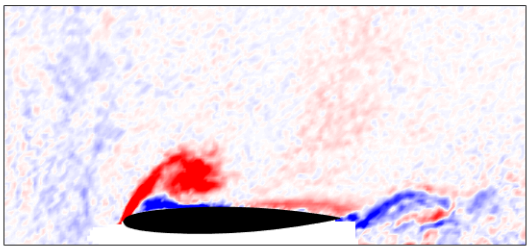

(c) $\frac{tU_\infty}{c} = 1.1,\ GR = 0.75,\ Re = 6000$

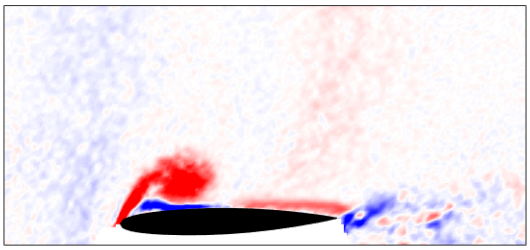

(d) $\frac{tU_\infty}{c} = 1.1,\ GR = 0.75,\ Re = 12000$

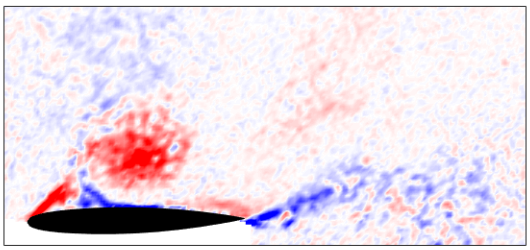

(e) $\frac{tU_\infty}{c} = 1.5,\ GR = 0.75,\ Re = 6000$

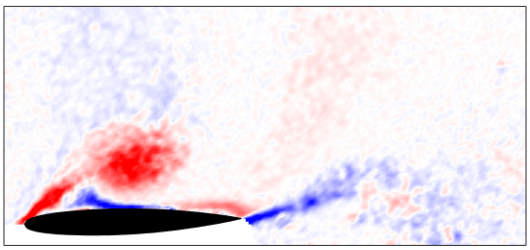

(f) $\frac{tU_\infty}{c} = 1.5,\ GR = 0.75,\ Re = 12000$

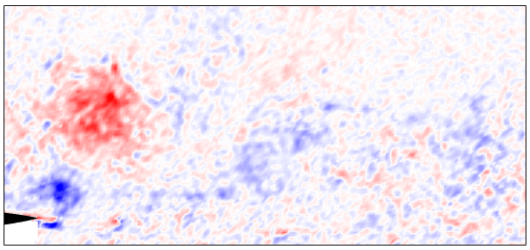

(g) $\frac{tU_\infty}{c} = 2.5,\ GR = 0.75,\ Re = 6000$

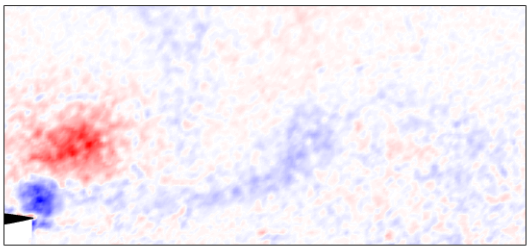

(h) $\frac{tU_\infty}{c} = 2.5,\ GR = 0.75,\ Re = 12000$

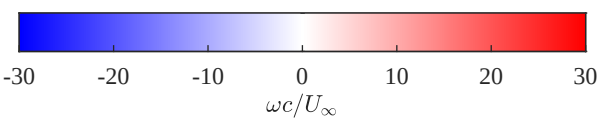

Figure 4.1: The vorticity fields for $GR = 0.75$ at (left) Re=6000 and (right) Re=12000

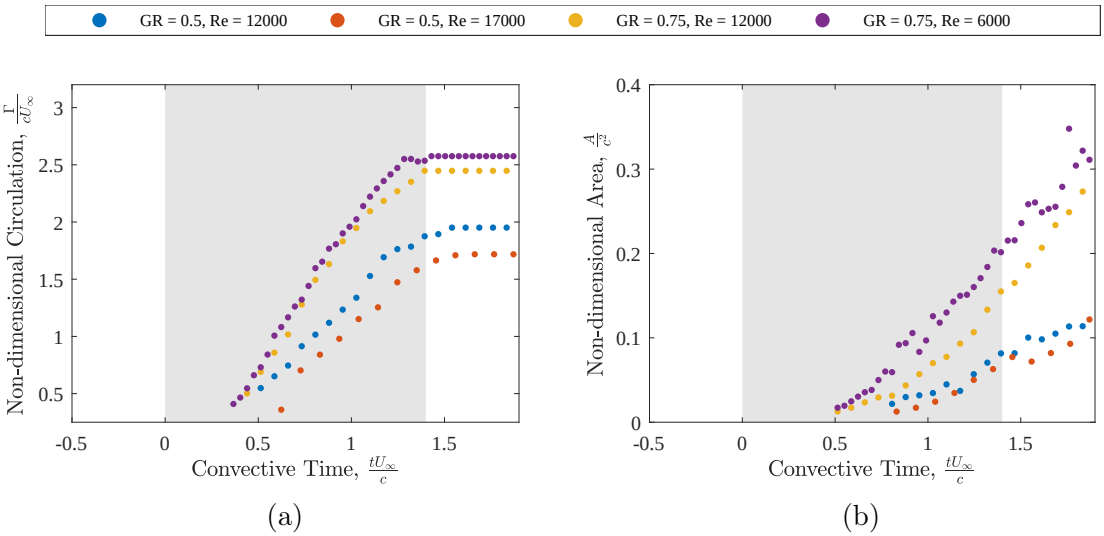

(a) (b)

Figure 4.2: The evolution of (a) the non-dimensional circulation and (b) the non-dimensional area of the LEV for the high gust ratio cases

4.1.1 High gust ratio regime

Figure 4.1 depicts the gust encounter vorticity fields at four different timesteps for $GR = 0.75$. $tU_\infty/c = 0$ corresponds to the leading edge entering the gust and $tU_\infty/c = 1.4$ corresponds to the leading edge exiting the gust. Figure 4.2 shows the LEV circulations and areas for the cases $GR = 0.50$ and $GR = 0.75$ which have been extracted from PIV using the method discussed in section 3.7.4. At $tU_\infty/c = 0.5$ the flow for both Reynolds numbers has already separated and formed a small but coherent LEV. The vortex has the same strength for both Reynolds numbers but for $Re = 6000$, the vortex encompasses a slightly larger area as shown in figure 4.2b. For $tU_\infty/c = 1.1$, a large region of secondary vorticity has formed under the LEV and the flow is attached past the midchord. As the wing moves through the gust the primary and secondary vorticities grow in strength and the reattachment point moves down the chord of the wing. As the wing is exiting the gust at $tU_\infty/c = 1.5$, the LEV is noticeably larger for $Re = 6000$ as well as at a higher vertical position

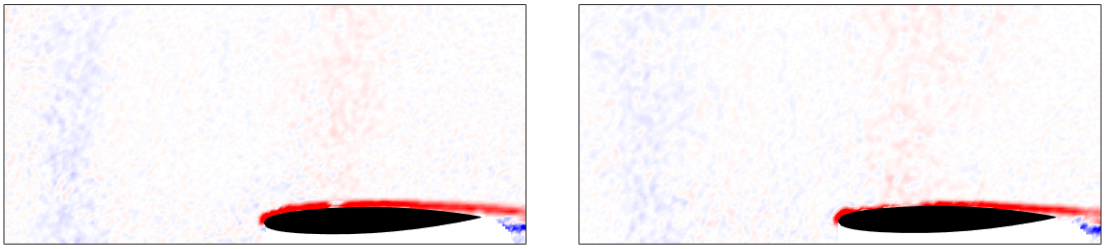

(a) $\frac{tU_\infty}{c} = 0.5$, $GR = 0.3$, $Re = 12000$

(b) $\frac{tU_\infty}{c} = 0.5$, $GR = 0.3$, $Re = 28000$

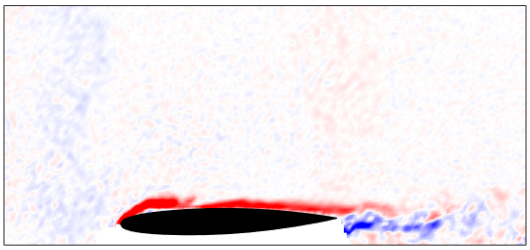

(c) $\frac{tU_\infty}{c} = 1.1$, $GR = 0.3$, $Re = 12000$

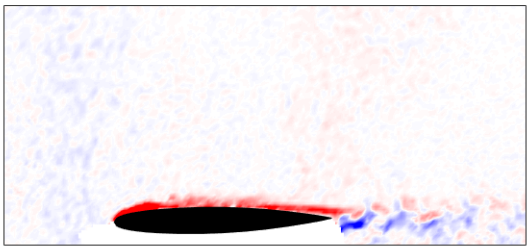

(d) $\frac{tU_\infty}{c} = 1.1$, $GR = 0.3$, $Re = 28000$

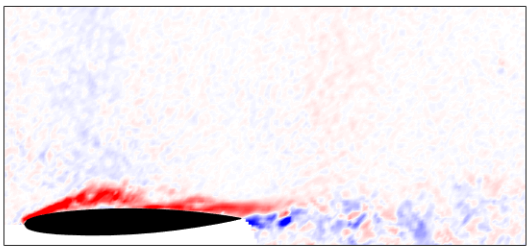

(e) $\frac{tU_\infty}{c} = 1.5$, $GR = 0.3$, $Re = 12000$

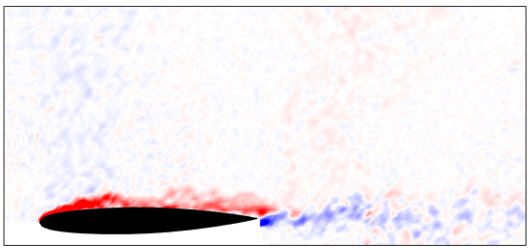

(f) $\frac{tU_\infty}{c} = 1.5$, $GR = 0.3$, $Re = 28000$

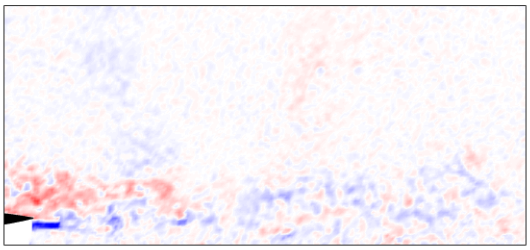

(g) $\frac{tU_\infty}{c} = 2.5$, $GR = 0.3$, $Re = 12000$

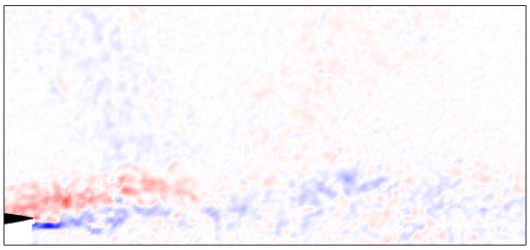

(h) $\frac{tU_\infty}{c} = 2.5$, $GR = 0.3$, $Re = 28000$

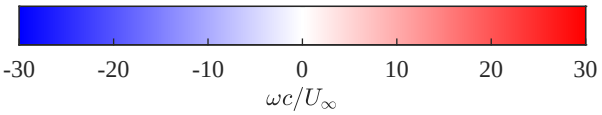

Figure 4.3: The vorticity fields for $GR = 0.30$ at (left) Re=12000 and (right) Re=28000

with respect to the wing. This is consistent with the fact that low Reynolds numbers promote viscous effects and the shear layer (originally a boundary layer on the leading edge with thickness $\propto Re^{-0.5}$) has diffused over more fluid and therefore has more mass. Although at both Reynolds numbers the secondary vorticity is separating at $tU_\infty/c = 1.5$, the separation at $Re = 6000$ is more advanced and has partly severed the advection of vorticity into the LEV. This is again consistent with the fact that at lower Reynolds numbers secondary vorticity is more diffuse but also more susceptible to separation. Thus, for a given imposed adverse pressure gradient, the vortex-wall interaction is expected to be more advanced. Before the boundary layer eruption mechanism can fully detach the LEV, the wing exits the gust and the LEV is shed. As the wing moves past the LEV in figures 4.1 (g) and (h), the reattachment point eventually reaches the trailing edge which induces flow reversal and a small trailing edge vortex (TEV) forms. A topological perspective on this flow reversal mechanism can be found in Rival et al. [90] for plunging kinematics. Furthermore, from figure 4.2 it is clear that the Reynolds number also affects the convective time of LEV onset, t^*_{onset}. As expected, increasing the Reynolds number delays the onset of flow separation and LEV formation.

4.1.2 Low gust ratio regime

The flowfields for $GR = 0.3$ are shown in figure 4.3. At $tU_\infty/c = 0.5$ the flow is fully attached. The flow develops differently for each Reynolds number as the wing moves through the gust at $tU_\infty/c = 1.1$. At $Re = 28000$ a boundary layer instability is seen at this time on the surface of the airfoil, while at $Re = 12000$ there is shear layer roll-up at the leading edge. At $tU_\infty/c = 1.5$ this leading-edge vortex has grown and is forcing flow reattachment, while at $Re = 28000$ no such forcing mechanism

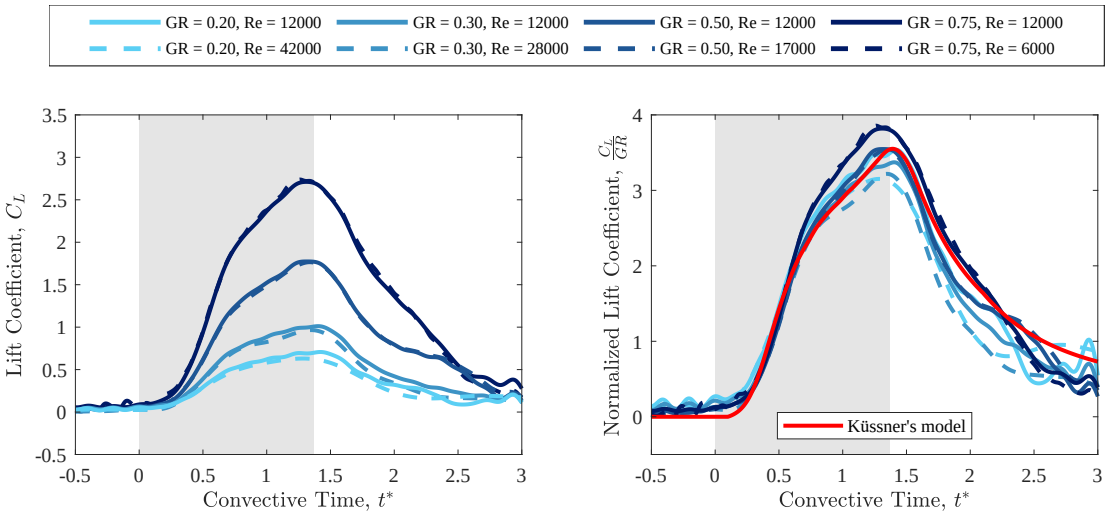

(a) (b)

Figure 4.4: Lift coefficient comparison for different gust ratios and Reynolds numbers for a blunt-edged airfoil encountering a trapezoidal gust: (a) Non-normalized (b) normalized by gust ratio

exists and the flow is separating at the trailing edge.

4.1.3 Force measurements

Figure 4.4 depicts the lift coefficients for each of the gust encounters discussed in sections 4.1.2 and 4.1.1. For the low gust ratio cases ($GR = 0.2$, $GR = 0.3$) the force coefficients are larger when the Reynolds number is lower. This is consistent with the results seen in section 4.1.2. At low gust ratios, the effective angle of attack is close to the static stall angle of attack, which is known to be a strong function of the Reynolds number. Therefore, changes in the Reynolds number can change the separation dynamics of the encounter. As shown in figure 4.3, the flow separates at the leading edge at $GR = 0.3$, $Re = 12000$ but not at $GR = 0.3$, $Re = 28000$. Furthermore, this effect can be seen in the gust ratio normalized lift coefficients of figure 4.4b. The high Reynolds number cases at low gust ratios converge to a smaller peak coefficient than the rest of the cases. A two sample t-test has been used to

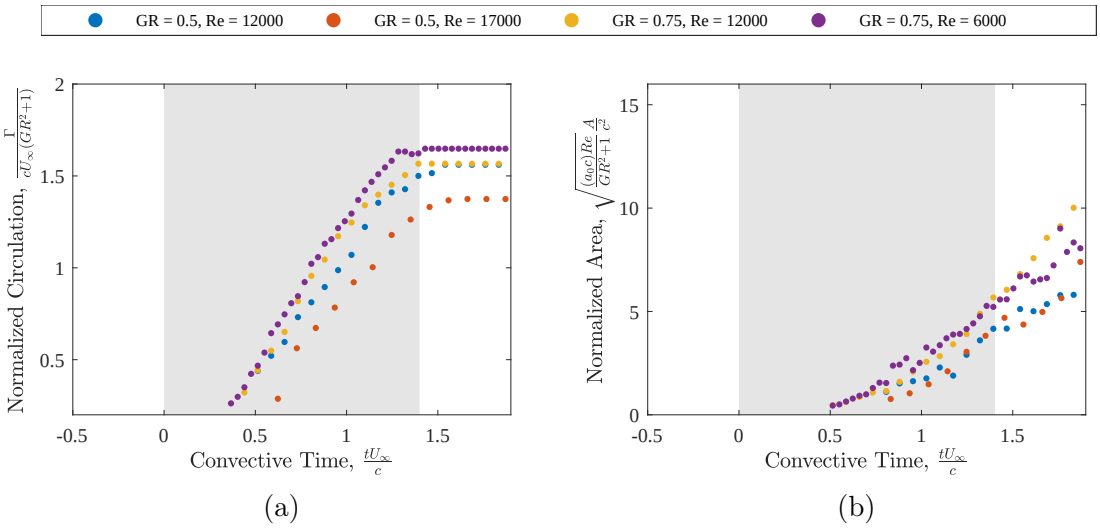

(a) (b)

Figure 4.5: Normalized LEV properties using the shear layer scaling suggested by equations (4.1) and (4.2): (a) Normalized LEV circulation and (b) Normalized LEV area

verify that the differences in maximum lift coefficient between Reynolds numbers is statistically significant at the 5% significance level.

Given the similarity of the flowfields and the strengths of the LEVs, it is not surprising that in the high gust ratio regime lift is independent of Reynolds number. This can be attributed to the fact that at high gust ratios the boundary layer effectively separates at the leading edge, not allowing any Reynolds number dependent effects to materialize. It is worth noting that the difference in size of the LEV as shown in figure 4.2b does not affect the forces. However, this might not always hold true, as the size of the LEV can trigger different LEV detachment mechanisms [108] which can in turn change the dynamics of the LEV. Figure 4.4b shows that the well-known gust ratio scaling is appropriate for high gust ratio gust encounters with rounded leading-edge wings. Figure 4.4b also shows the lift response of Küssner's model for the trapezoidal gust shape. As observed in previous studies, the overall agreement with experimental data is good. The success and shortcomings of the model will be investigated in section 4.3.

4.2 LEV growth

In this section the vortex integral properties discussed in section 2.4.1 are used to study the growth of the vorticity shed from the leading edge. A trapezoidal gust has an approximately uniform gust ratio across its width. Therefore, the LEV circulation in equation (2.53) and LEV size in equation (2.56), written in terms of the non-dimensional variables scale as follows,

$$\frac{\Gamma}{cU_\infty} \propto \frac{1}{2}(GR^2+1)t^* \tag{4.1}$$

$$\frac{A}{c^2} \propto 1.2t^*\sqrt{\frac{GR^2+1}{(a_0c)\ Re}} \tag{4.2}$$

According to this formulation the growth of non-dimensional circulation is linear in t^* with slope proportional to (GR^2+1). The growth of the non-dimensional LEV size is also linear in t^* but with a slope that is governed by three non-dimensional parameters: gust ratio, Reynolds number, and the product of chord with a_0, the streamline curvature around the stagnation point (for details on its calculation see section 2.4.1).

Equations (4.1) and (4.2) suggest an alternative scaling of the LEV growth. Figure 4.5 depicts the data of figure 4.2 normalized by the prediction of equation (4.1) and (4.2) for each case, i.e., (GR^2+1) for the circulations, and $(GR^2+1)^{0.5}\ (a_0c)^{-0.5}\ Re^{-0.5}$ for the areas. The normalized LEV properties in figure 4.5 have similar growth rates across the different cases, which suggests that, for the parameter space examined, the LEV circulation and size growth are approximately proportional to the quantities suggested by equation (4.1) and (4.2). The disparity in the growth rates increases with convective time. This could be attributed to the simplified calculation of the shear layer velocity. At the initial stages of the gust encounter, the flowfield is dominated by

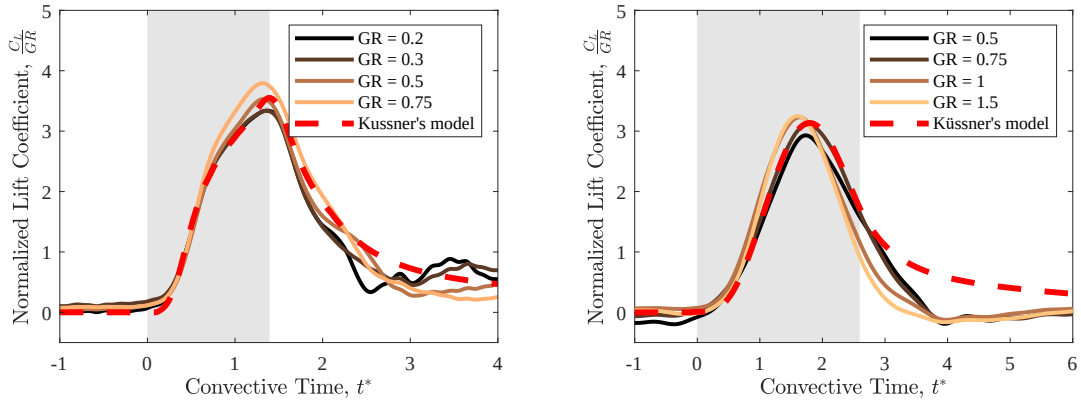

Figure 4.6: Experimental and theoretical lift coefficients normalized by gust ratio for (a) Trapezoidal gust profile and (b) Sine-squared gust profile

gust vorticity. However, in the latter stages, there is significant build up of bound and LEV circulation, which affect the shear layer velocity. The two cases with $Re = 12000$ remain in fair agreement, while the case with $Re = 6000$ has a slightly larger maximum LEV circulation, and the case with $Re = 17000$ has a slightly lower maximum LEV circulation. This suggests that the Reynolds number is important in the leading edge vorticity production after the wing has spent more than 1 convective time inside the gust.

4.3 Comparison of experimental and theoretical circulations

This section evaluates the differences in circulation budget and lift between the experimental data and Küssner's model. The normalized experimental and theoretical lift coefficients for the two different gust profiles are presented in figure 4.6. The model performs remarkably well during the early phases of the gust encounter. This suggests that the experimental lift early in the gust encounter is indeed non-circulatory as shown in figure 2.9. This phenomenon has been investigated by Corkery and Babinsky

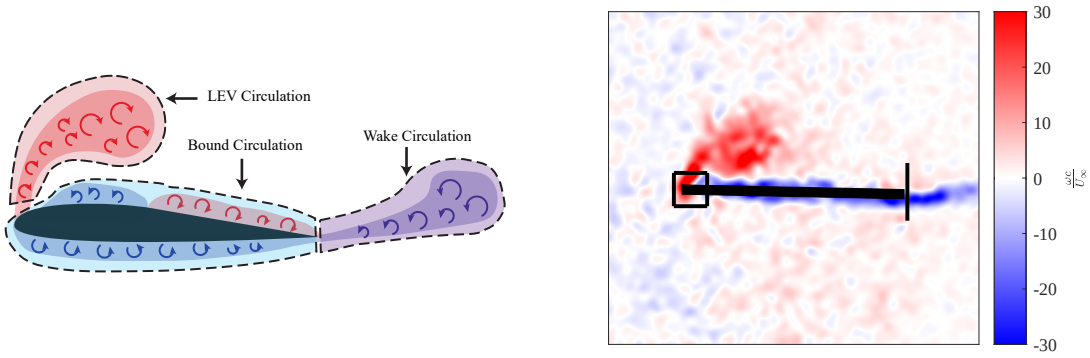

(a) (b)

Figure 4.7: The circulation of the LEV was measured from the flux of positive vorticity through a square control volume centered at the leading edge. Circulation shed in the wake was measured from the flux of total circulation through a plane perpendicular to the trailing edge. (a) Decomposition of the circulation in the flowfield and (b) Surfaces through which vorticity fluxes were measured.

[19] for wings with small thickness and extended to bodies of finite thickness by Gehlert and Babinsky [40]. Effects that do not scale with gust ratio appear around $t^* = 0.75$, approximately coincident with the onset of flow separation. Namely, the rate of increase of normalized lift slightly increases with increasing gust ratio, and the convective time of the peak lift coefficient slightly decreases with increasing gust ratio. This has also been reported by Andreu-Angulo et al. [6] and Andreu-Angulo and Babinsky [5] (See for example figure 18 in Andreu-Angulo and Babinsky [5]). After the peak lift coefficient is reached, the experimental lift has a sharper drop-off than Küssner's model. This drop-off is more pronounced for the sine-squared gust encounter.

To investigate the above results, the experimental circulations shed from the leading and trailing edges are quantified. The partitioning is carried out as shown in figure 4.7a. All vorticity shed from the leading edge is counted as LEV circulation, Γ_{LEV}, while all vorticity shed from the trailing edge is counted as wake circulation, Γ_w. As

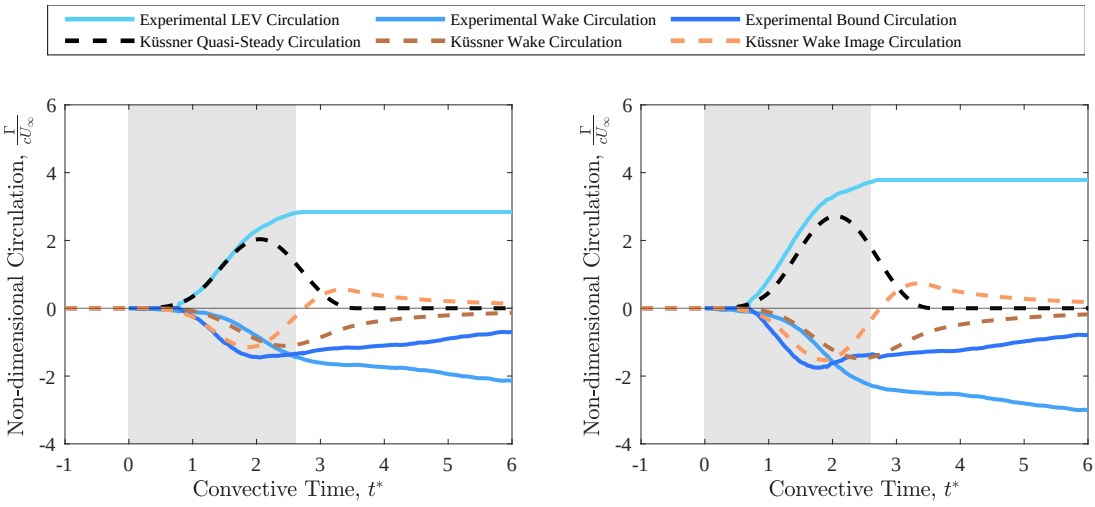

Figure 4.8: Experimental and theoretical circulation trends during a transverse gust encounter for a sine-squared gust at (a) $GR = 0.75$ and (b) $GR = 1$

the sum of gust circulation must be 0, the bound circulation, Γ_b, can be approximated by the (negative) sum of the leading edge and trailing edge circulations. Therefore, $\Gamma_b = -(\Gamma_{LEV} + \Gamma_w)$. The leading edge circulation is captured by measuring the flux of vorticity through a control volume centered at the leading edge with side length 8% of the chord. The trailing edge circulation is quantified by measuring the flux of vorticity through a plane located at the trailing edge which is perpendicular to the wing. The flux surfaces used are shown in figure 4.7b.

A similar circulation decomposition can be applied to Küssner's model. Since in this case the flow is attached, the bound circulation must be equal and opposite of the total circulation in the wake, $\Gamma_b^K = -\Gamma_w^K$, where $()^K$ denotes quantities related to Küssner's model. The bound circulation in Küssner's model can be further decomposed into quasi-steady circulation, Γ_{qs}^K, and the circulation due to the image vorticity of the wake, Γ_{IW}^K.

Figure 4.8 depicts the evolution of each circulation in Küssner's model as well as the experimental circulations for sine-squared gust encounters at gust ratios of

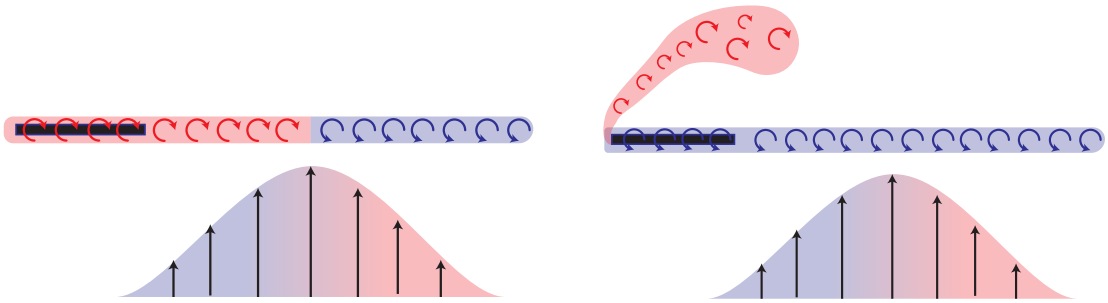

(a) (b)

Figure 4.9: Wake vortex sheet distributions during a transverse gust encounter for (a) Küssner's model and (b) experiments

0.75 and 1. From figure 4.6b, $GR = 0.75$ shows the best agreement with Küssner's model. The circulation trends for this case are shown in figure 4.8a. Early on in the gust encounter, both experimental and theoretical circulations are small. This is consistent with the understanding that in this phase of the gust encounter most of the force is non-circulatory as discussed in section 2.3.5 and shown in figure 2.9. As the effective angle of attack increases, the flow separates and a LEV forms at a convective time of $t^* = 0.75$. As positive circulation accumulates in the LEV, negative bound circulation develops on the wing which is manifested in the wing's attached pressure side boundary layer, as well as suction side secondary vorticity. Circulation shed from the trailing edge starts to increase as the wing is fully immersed in the gust at around $t^* = 1$. Interestingly, this trailing edge circulation very nearly follows the theoretical circulation shed in Küssner's model up until $t^* = 2$. Since in Küssner's model $\Gamma_w^K = -\Gamma_b^K$ and in the experiments $\Gamma_w = -(\Gamma_{LEV} + \Gamma_b)$, it then follows that $\Gamma_{LEV} + \Gamma_b = \Gamma_b^K$, i.e., although the real viscous flow is separated, the bound circulation of Küssner's inviscid model captures the combined circulations of the bound vortex and LEV in the experiments.

For $GR = 0.75$, the circulation trends possess two more interesting characteris-

tics: (i) The LEV circulation is approximately equal to the theoretical quasi-steady circulation and (ii) the experimental bound circulation is approximately equal to the theoretical bound circulation induced by the wake in Küssner's model (the image vorticity required to enforce no flow through the wing, and the Kutta condition). In other words, Küssner's bound circulation approximates the experimental bound vortex-LEV pair with the LEV carrying positive circulation instead of the quasi-steady bound vortex. This fact, along with favorable vortex dynamics (to be discussed in section 4.4), gives the model predictive power over a significant portion of the gust encounter.

However, this phenomenon breaks down at around $t^* = 2$, at which point the circulations diverge between theory and experiment. This is caused by the following discrepancy between Küssner's model and the real separated flow: In the attached flow theoretical model, the wing's quasi-steady circulation decreases as it nears the exit of the gust and positive upwash-inducing vorticity must be shed to satisfy Kelvin's circulation theorem, as discussed in section 2.3.5. This is shown in figure 4.9a, where in the second half the gust encounter the circulation shed from the trailing edge is positive. In contrast, in the real separated flow it is the LEV that is supplying the lift and not the bound circulation. As the effective angle of attack decreases, the wing will shed part of its bound circulation, which in this case is negative and downwash-inducing. This is depicted in figure 4.9b and can be seen in the PIV vorticity fields of figures 4.1 (e) and (f). The absence of upwash-inducing wake vorticity is the reason a much sharper drop-off is observed in experiments when compared to Küssner's model. The model is only able to capture the correct wake topology while the quasi-steady circulation is increasing. This is also shown quantitatively in figure 4.8, where in the second half of the gust encounter the experimental wake circulation continues to decrease, while Küssner's wake circulation increases until it reaches 0. This persistent negative circulation in the experimental wake and the negative bound circulation

after the gust exit often cause negative lift in the aftermath of the encounter (see for example figure 4.6b and figure 18 in [5]). Upon gust exit the effective angle of attack is zero. The LEV is shed and is no longer supplying much positive lift, but the wake is still inducing downwash, thus causing negative lift.

Further discrepancy between theory and experiments can be caused by the fundamental difference in the vorticity generation mechanism between linear theory and separated lifting flows. The circulation of Küssner's quasi-steady bound vortex is created from the integrated effect of the effective angle of attack over the chord of the wing, and thus scales linearly with gust ratio. In contrast, the LEV has no such restriction. In section 4.2 it was shown that under certain conditions, the vorticity generated at the leading edge can instead be a function of the gust ratio squared, and only a function of the effective angle of attack at the leading edge. Furthermore, it has been observed in this study as well as in studies of wings with unsteady kinematics [24, 57], that increasing the magnitude of the unsteady parameters can lead to earlier flow separation and thus a decreasing time of LEV onset, t^*_{onset}. This can be seen in figure 4.8b which shows the circulation trends for Küssner's model and the experiments at a gust ratio of 1. In this case, the LEV circulation leads the quasi-steady circulation in Küssner's model by approximately 0.1 convective times. The corresponding lift transient in figure 4.6b shows similar characteristics, as the peak lift coefficient is earlier than Küssner's model and the rate of increase of lift is slightly larger for higher gust ratios. This effect can also be seen in figure 4.6a for a trapezoidal gust, where again the rate of increase of normalized lift increases with gust ratio. It is worth noting that the rate of increase of LEV vorticity does not directly translate to a corresponding increase in lift, as the bound circulation also needs to be accounted for. Unfortunately, bound circulation is a function of the proximity of the LEV to the wing, as well as the size of the region the LEV occupies,

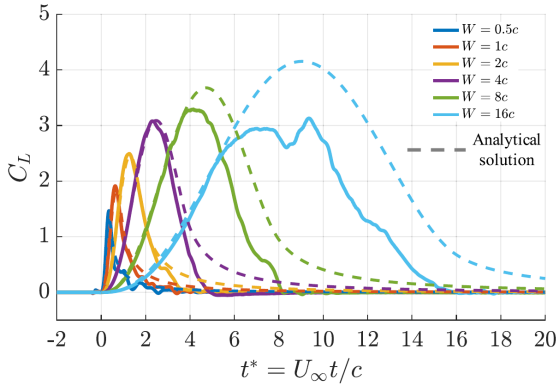

Figure 4.10: Computational and theoretical lift transients for a sine-squared gusts, varying the gust width at a gust ratio of 0.8 [8]

and thus its growth rate is a nontrivial function of gust ratio. The data suggest that the circulatory lift during a transverse gust encounter increases with a factor slightly larger than gust ratio, i.e., GR^n where $1 < n < 2$.

4.4 Vortex detachment

In the previous section it was observed that, early in the gust encounter, Küssner's model captures the general circulatory characteristics of the real viscous flow. However, equation 2.11 implies that the convection of vorticity is also a contributor to the overall lift of the system. Indeed, the experimental agreement with Küssner's model demonstrated in this study and in previous studies [9, 14, 21] is expected to break down after some critical gust width, due to the convection of the LEV. For long enough gusts, the LEV will reach its maximum circulation and detach. The purpose of this section is to quantify the critical gust width and to show that the gust widths under investigation are shorter than the critical vortex formation timescale. Thus, we can expect the LEV to remain attached for the duration of gust encounter. In this study, an LEV is called attached if it is connected to the feeding shear layer while also convecting at a speed close to the freestream velocity.

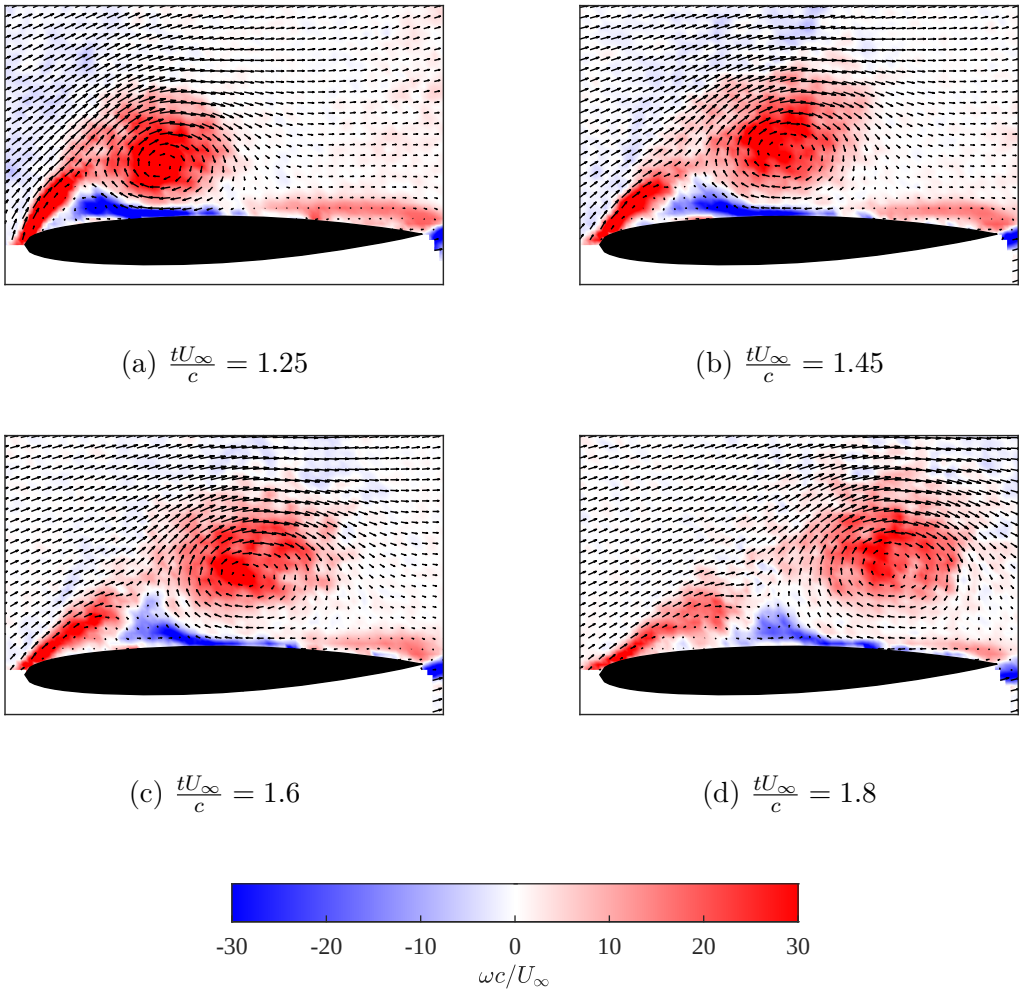

(a) $\frac{tU_\infty}{c} = 1.25$

(b) $\frac{tU_\infty}{c} = 1.45$

(c) $\frac{tU_\infty}{c} = 1.6$

(d) $\frac{tU_\infty}{c} = 1.8$

Figure 4.11: Vorticity contours and velocity vector field in the reference frame of the wing at $GR = 0.75$ and $Re = 12000$, depicting the progression of the forced LEV detachment upon gust exit.

Stall-delay has been shown to be a function of the unsteady flow parameters [24]. Le Fouest et al. [64] quantified the stall-delay for pitching wings as a function of reduced pitch rate. They found that the delay obeys a decaying power law, and as pitch rate increases the delay asymptotically approaches the vortex formation number discussed in section 1, i.e., the maximum time the LEV can grow before reaching its maximum circulation and detaching. For a gust encounter, the pitch rate corresponds to the rate of change of the effective angle of attack. This means that the high-amplitude, high-frequency gust encounters presently being studied have an effective pitch rate that is an order of magnitude higher than that required to achieve vortex formation stall delay. Therefore, it is expected that the vortex formation timescale is the limiting timescale of the observed lift transient and can be used to approximate how wide a gust needs to be for stall to occur - stall in this case referring to the lift drop-off at the end of the dynamic stall process.

Starting from the definition of vortex formation time, $\hat{T} = C\Gamma/(D\Delta U)$, for leading-edge vorticity production the constant, C, is often taken to be one, as discussed in Rival et al. [90] and the characteristic length-scale, D, to be the chord. Furthermore, the velocity across the shear layer during a gust encounter is $U_{SL} = \sqrt{U_\infty^2 + V^2} = U_\infty\sqrt{GR^2+1}$ and the circulation of the LEV is expected to scale with U_{SL}^2 [28, 108, 110], i.e., $\Gamma_{LEV} = KU_{SL}^2 t$, where K is the proportionality constant between the square shear layer velocity and the LEV circulation. Thus, we have the following,

$$\hat{T} = \frac{C\Gamma_{LEV}}{c\Delta U} = \frac{KtU_{SL}^2}{cU_{SL}} = K\frac{U_\infty t}{c}\sqrt{GR^2+1} = Kt^*\sqrt{GR^2+1} \tag{4.3}$$

According to vortex formation theory, there a exists a critical formation time, $\hat{T}_{crit}$, at which the LEV will reject any additional vorticity and detach. Using the above

relation it is then possible to recover the critical convective time (or the gust width-to-chord ratio) that a wing can spend inside a gust without stalling. Rearranging equation (4.3),

$$t^*_{crit} = \left(\frac{w}{c}\right)_{crit} = \frac{\hat{T}_{crit}}{K\sqrt{GR^2+1}} \tag{4.4}$$

Equation (4.4) states that as the gust ratio increases, the critical width-to-chord ratio decreases since the LEV will reach its critical circulation faster. To the authors knowledge, there exist no experimental apparatus that can vary the gust width to determine the constants in equation (4.4). Badrya et al. [8] conducted a CFD study for sine-squared gusts, keeping the gust ratio fixed and varying the gust width. The lift coefficients are shown in figure 4.10 along with Küssner's prediction for each. Their results show that for $GR = 0.8$, Küssner's theory captures the lift transient all the way up to a gust width-to-chord ratio of 4, after which stall onset hampers the model's performance.

The experiments presented in this dissertation have a maximum gust width-to-chord ratio of 2.6, well below the critical width-to-chord ratio predicted above, even after accounting for a higher gust ratio. Therefore, the LEV grows until the wing exits the gust at which point it detaches. This is evident in figure 4.2a, as the peak circulation for each of the cases takes place as the wing is exiting the gust. Further, figure 4.10 shows that for gust widths longer than 4 chords, the peak lift coefficient takes place before the wing starts exiting the gust. The detachment of the LEV is facilitated by a forced interaction between the primary shear layer and the secondary vorticity. The progression of the forced detachment is depicted in figure 4.11 for $GR = 0.75$, $Re = 12000$. In figure 4.11a , the wing is fully immersed in the gust. The LEV is attached and the separation angle at the leading edge is high due to the high

effective angle of attack. As the wing is exiting the gust in figures 4.11b and 4.11c, the effective angle of attack gradually decreases and the shear layer moves closer to the wing surface where it interacts with the secondary vorticity. The downward-moving fluid of the secondary vorticity reverses part of the flow of the primary shear layer, reducing the advection of vorticity into the LEV. By $tU_\infty/c = 1.8$ in figure 4.11d, the advection of vorticity into the vortex has ceased and the LEV has detached.

4.5 Chapter summary

This chapter investigates the lift and shed vorticity distributions of wing's encountering transverse gusts. Emphasis is placed on comparing experimental lift transients and shed vorticity distributions with those predicted by inviscid theory. The following concepts are applied to transverse gust encounters: (i) The notion of optimal vortex formation time, and (ii) LEV growth prediction through the integration of shear layer fluxes. The circulation shed in the wake of Küssner's model were compared with the circulation shed in the wake during experiments. A key result is that although the real viscous flow is separated, the bound circulation in Küssner's inviscid model captures the combined circulation of the bound vortex-LEV pair of the experiments, conditioned on an increasing quasi-steady circulation. The performance of Küssner's model deteriorates once the quasi-steady circulation starts to decrease. This is because the lift-producing mechanisms between theory and experiment are fundamentally different, even though they produce similar values of lift while the quasi-steady circulation is increasing.

Chapter 5: Unsteady surface pressure measurements in a gust

This chapter investigates the unsteady pressure distributions produced during transverse wing-gust encounters. Pressure measurements are initially presented for steady and unsteady wings in pre-stall and post-stall configurations. The flowfields and pressure distributions are then concurrently analyzed. Finally, quantities derived from pressure are explored in the context of flow sensing for gust encounters.

5.1 Steady measurements

In this section, data from steady-state experiments are presented and the pressure measurements are examined and validated. Figure 5.1 presents steady (time-averaged) pressure and load measurements at varying angles of attack at a Reynolds number of 50,000. The figure compares lift, drag, and midchord pitching moment coefficients obtained from the force transducer as well as the pressure integration procedure described in section 3.7.3. Figure 5.1 also depicts four examples of time-averaged pressure distributions for $\alpha \in [2^\circ, 6^\circ, 12^\circ, 16^\circ]$ along with pressure distributions generated by the XFOIL airfoil analysis tool discussed in section 3.7.5. The XFOIL distributions were generated using viscous mode, based on the effective angle of attack at the measurement section, taking into account the induced angle of attack computed using equation (3.6).

The measured pressure distributions and force data in figure 5.1 indicate that the

flow remains attached at the leading edge up to an angle of attack of 12°. For these attached flow cases, the measured pressure distributions are in close agreement with those obtained from XFOIL. A stagnation point with $C_p = 1$ forms on the leading edge for each angle of attack. A pressure plateau signifies the formation of a laminar separation bubble for cases $\alpha \in [6°, 12°]$ at 30% and 10% of the chord, respectively, a flow characteristic also present in the XFOIL distributions. The separated pressure distribution at $\alpha = 16°$ exhibits a near-flat suction-side pressure of $C_p = -1$, while the pressure side closely follows the attached flow solution. For post-separation angles of attack, XFOIL is known to lose its accuracy due to assumptions built-in its viscous-inviscid coupling scheme. In this case, XFOIL predicts the presence of a laminar separation bubble near the leading edge, a flow characteristic not present in the measurements.

The lift coefficients obtained from pressure integration are nearly identical to those obtained from the force transducer for all angles of attack up to 12°. For post-stall angles of attack, the lift drop-off as measured from pressure is larger than the one measured from the force transducer. In , there is some contribution to lift that is not reflected in the sectional pressure distribution measured near the centerline. This suggests a concentration of lift near the tips of the wing, which is consistent with the discussion in section 3.7.5 and recent work on the lift generation of low aspect ratio wings at high angles of attack [26, 69]. In this regime, tip vortices can induce reattachment as well as vortex lift near the wing tips, creating lift distributions that grow in strength near the tips. Pressure sensors near the center of the wing are not able to capture this lift mechanism, and so cannot capture the full lift produced by the wing.

The pressure-integrated drag coefficient has a constant but small bias when compared to the true drag coefficient (as measured by the force balance), likely due to the

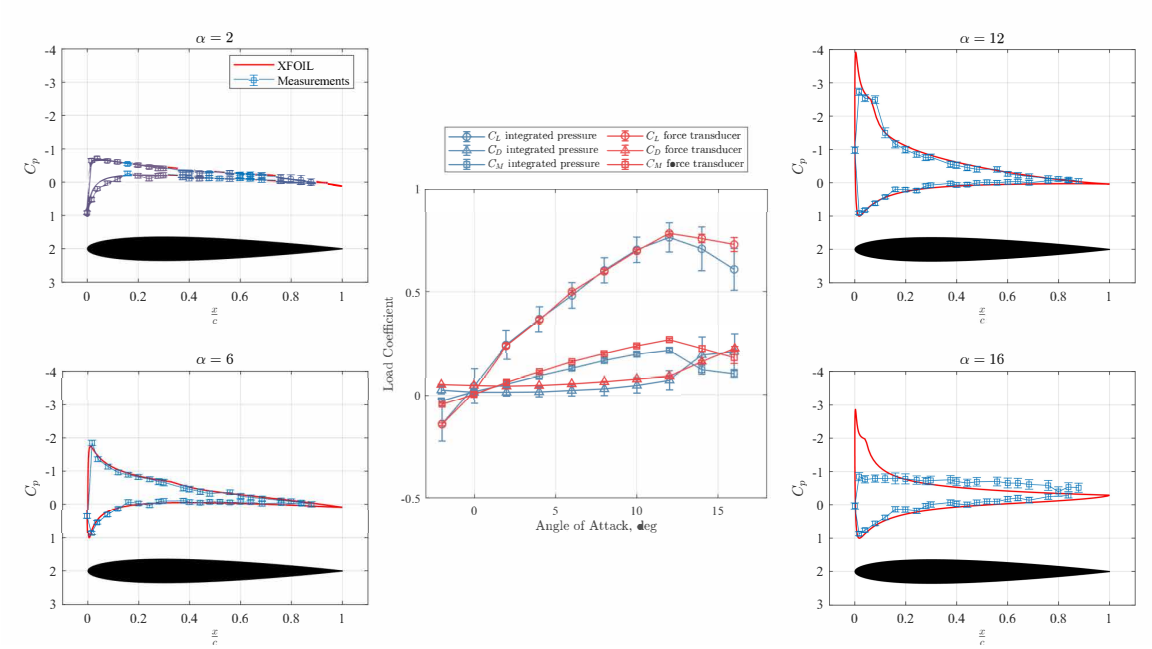

Figure 5.1: Steady-state pressure distributions and load coefficients measured at Reynolds number of 50k. The pressure distribution plots also display XFOIL generated pressure distributions. The load coefficient plots compare the loads measured from the force balance with the loads obtained from pressure integration.

omission of the skin friction contribution to drag. Past the static stall angle of attack, the drag coefficient increases drastically and the pressure-integrated drag converges to the true drag, indicating that the overall drag is primarily due to pressure. The pitching moment coefficient attained through pressure integration follows a similar estimation trend as the lift coefficient, with the addition of a small bias that increases with angle of attack. A possible explanation for this bias is the lack of resolution of the leading edge suction peak, a well-known pressure characteristic of airfoils at incidence, and evident in the XFOIL distributions. Overall, the data suggests that the pressure sensing platform is able to capture the characteristics of steady pressure distributions and the pressure integration is able to predict the the overall lift, pressure drag and moment coefficients, with good accuracy, albeit with deterioration in the lift and pitching moments after the onset of stall.

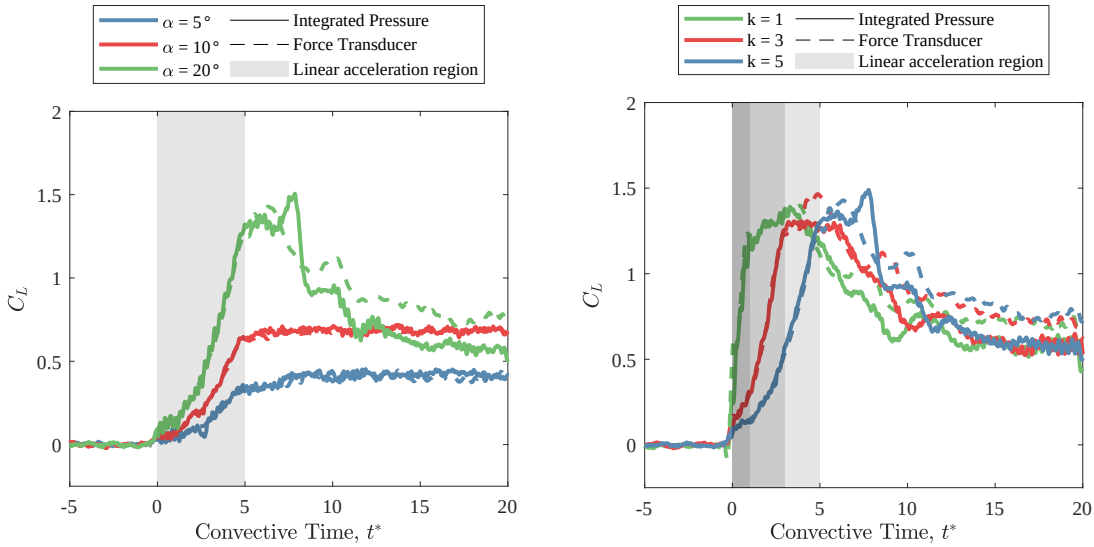

Figure 5.2: Lift coefficient transients obtained from pressure integration and force balance measurements for impulsively started wings at (a) varying angles of attack and (b) varying acceleration parameters

5.2 Unsteady measurements

In this section, pressure and load measurements are presented for impulsively started wings, with the aim of validating the time-response of the pressure sensors to accelerating flows and to extend observations of the sectional pressure measurements and integration procedure to the unsteady regime. The lift behavior of impulsively started wings at incidence has been extensively studied and is known to be governed by the vortex formation stage, during which lift increases, and the vortex detachment phase, during which lift decreases and approaches steady state [12, 37, 71]. Figure 5.2a compares the lift transients measured from the force transducer with those calculated from integrating pressure, for an impulsively started wing at $\alpha \in [5°, 10°, 20°]$. The wing is accelerated from rest with constant acceleration over a distance of five chords. For each of the angles of attack, the pressure integration captures the lift during the

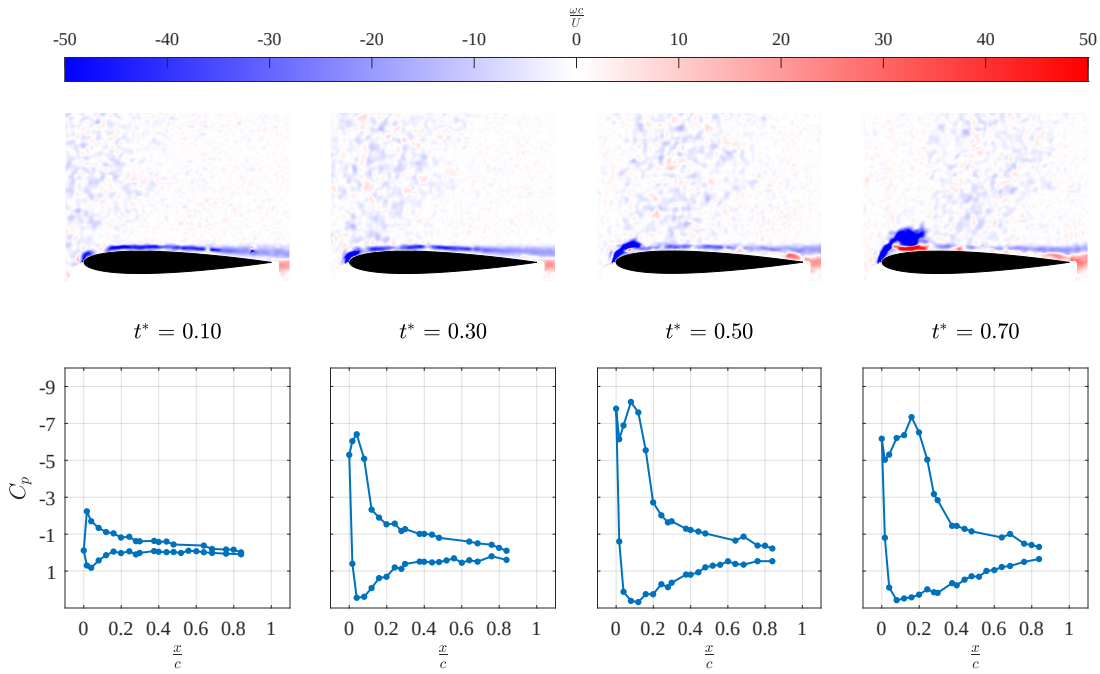

Figure 5.3: Vorticity fields and pressure distributions during a gust encounter at GR = 1, at four different timestamps

initial transient. For the attached flow cases, $\alpha \in [5°, 10°]$, the pressure integration and force transducer measurements continue to agree into the steady-state region. For $\alpha = 20°$, the pressure integration starts to undershoot lift when lift starts to decrease after approximately seven convective times. Hence, during the vortex formation stage of the dynamic stall process, the sectional pressure distribution accurately tracks the overall lift. However, once lift starts to drop due to the detachment of leading-edge vortex, three dimensional effects discussed in section 5.1 are realized and the sectional pressure distribution no longer reflects the distribution near the tips.

Figure 5.2b compares the lift transients measured from the force transducer with those calculated from integration pressure, for impulsively started wings at $\alpha = 20°$, for $k \in [1, 3, 5]$, where k is the acceleration parameter, denoting the distance in chords during which the acceleration takes place. Each of the cases is qualitatively similar.

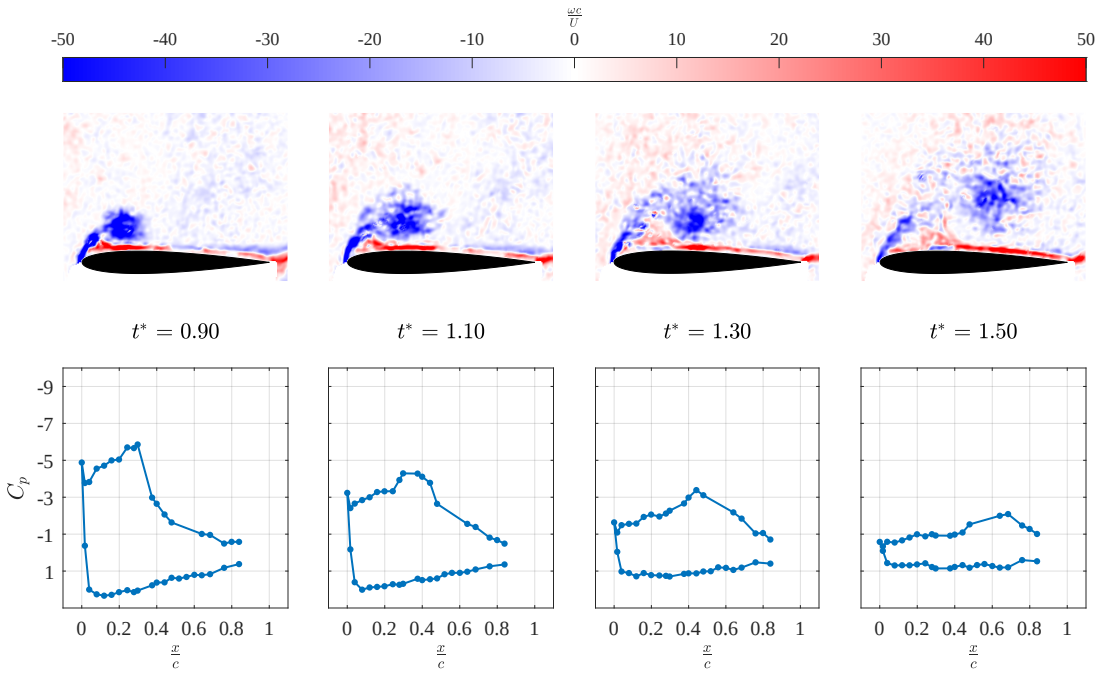

Figure 5.4: Vorticity fields and pressure distributions during a gust encounter at GR = 1, at four different timestamps

The lift from pressure tracks the force transducer lift for each of the cases during the initial transient, and eventually undershoots the overall lift by an amount that is independent of the acceleration parameter. Each of the curves converge to their expected steady-state values. It is worth noting that the sensors are able to respond to each of the accelerations with no sign of measurement delay or hysteresis.

5.3 Transverse gust encounters

5.3.1 Pressure-flowfield analysis

In this section the unsteady pressure distributions during transverse gust encounters are investigated. Figures 5.3 and 5.4 show the vorticity contours along with the corresponding pressure distributions at different convective times, defined as

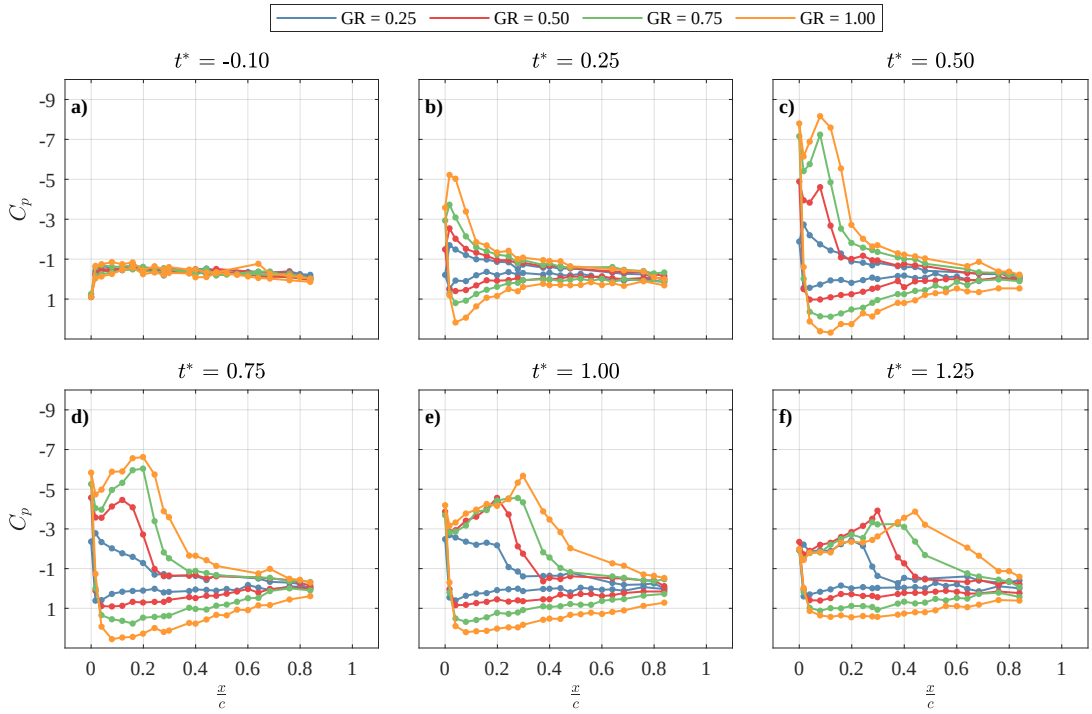

Figure 5.5: Pressure distribution during a gust encounter for four different gust ratios and at six different timestamps

$t^* = tU_\infty/c$, during a gust encounter with GR = 1. The wing enters the gust at convective time $t^* = 0$. At $t^* = 0.1$, the flow is attached and the pressure distribution resembles that of steady-state airfoil at a moderate angle of attack. The stagnation surface pressure coefficient is almost exactly 1, as most of the dynamic pressure at that point comes from the freestream velocity. At $t^* = 0.3$, the stagnation pressure coefficient rises to approximately 2 due to the dynamic pressure induced by the gust. The vorticity contours at this timestep depict vorticity concentration in the first 10% of the chord. This concentration corresponds to a pressure peak of approximately the same expanse. The width of this pressure peak resembles that of a separation bubble (see figure 5.1 $\alpha = 12°$) but its pressure is much lower than typical steady-state separation bubbles. At $t^* = 0.5$, the flowfield shows the concentrated vorticity lifting off the surface, initiating the formation of a small but coherent LEV. A secondary

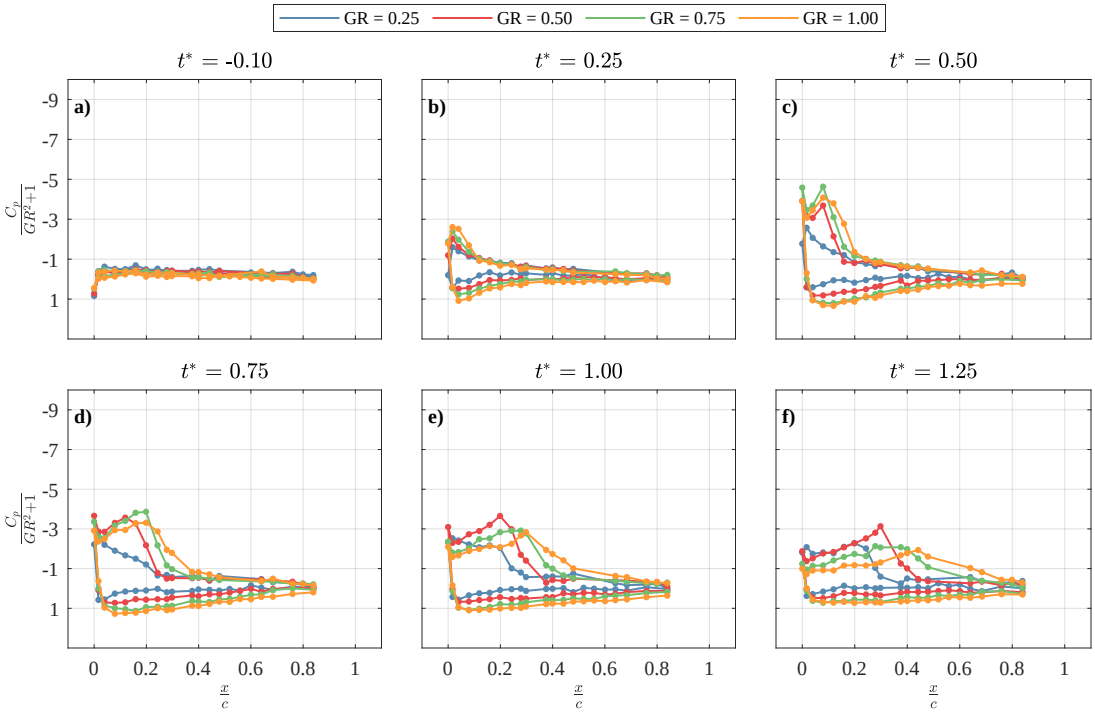

Figure 5.6: Gust dynamic pressure normalized pressure distribution during a gust encounter for four different gust ratios and at six different timestamps

suction peak is evident in the pressure distribution at this timestep. The pressure peaks at the leading edge and then again at 15% of the chord, directly below the LEV. At $t^* = 0.7$, both the primary and the secondary pressure peaks have decreased in strength and the secondary peak has grown in width, with its extremum directly below the vortex core. The pressure on the bottom side has a linear profile, starting at the stagnation pressure near the leading edge ($C_p \approx 2$) and ending at the farfield static pressure near the trailing edge ($C_p \approx 0$). As the flow develops in figure 5.4, the pressure peak continues to decrease in strength despite the increasing size and strength of the LEV. This can be attributed to the vertical distance between the vortex and the airfoil surface, which increases once the vortex separates and convects away from the feeding shear layer. At each of the subsequent convective times in figures 5.3 and 5.4, the suction peak and LEV convect downstream in unison. As the

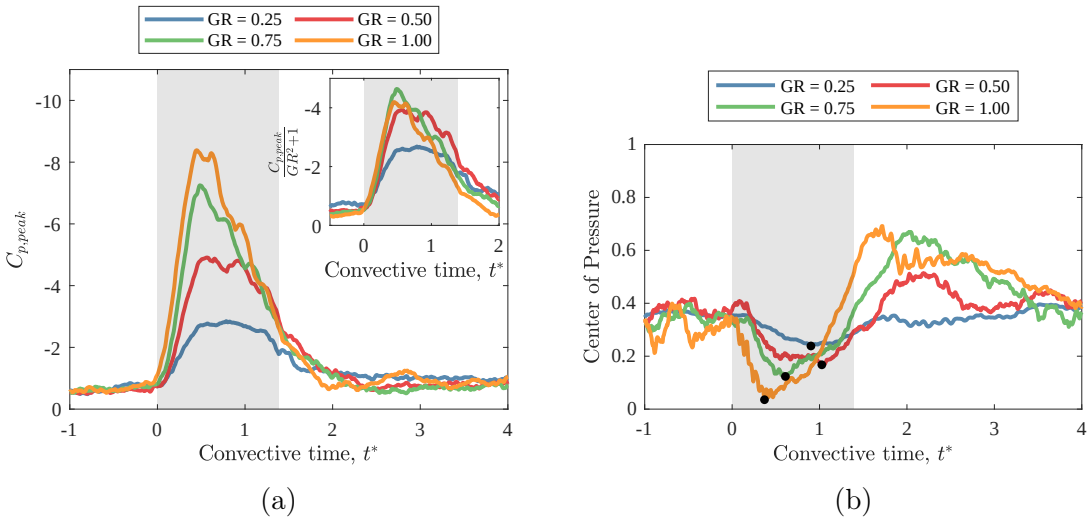

Figure 5.7: Variation of (a) the pressure distribution suction peak and (b) the wing's center of pressure, as function of convective time at four different gust ratios. The pressure peak is computed as the minimum pressure of the pressure distribution and the inset displays the same data normalized by the gust dynamic pressure.

wing exits the gust at $t^* = 1.3$ and 1.5, the stagnation pressure returns to 1, the LEV detaches, and the suction peak diminishes.

5.3.2 Effect of gust ratio

The pressure distributions for all the gust ratios at six different convective times are plotted in figure 5.5. At $t^* = -0.1$, each of the pressure distributions has a stagnation point at the leading edge and equivalent pressures on the top and bottom side of the airfoil. At $t^* = 0.25$, the pressure distributions are qualitatively similar, with pressure loading concentrated near the leading edge and proportional to GR. By $t^* = 0.5$, the secondary peak has formed for each of the gust ratios except for GR = 0.25. The secondary peaks increase in strength with gust ratio and are located at approximately the same chordwise location. At $t^* = 0.75$, the strengths of the secondary peaks have decreased in strength at a rate that is proportional to gust

ratio (higher gust ratio results in bigger decay in suction peak) and have moved in the chordwise direction by an amount proportional to gust ratio (higher gust ratio results in more chordwise motion). These trends persist for the remainder of the gust encounter, and as a result, at $t^* = 1.25$ the suction peak strength is the same for all gust ratios, but is further down the chord for higher gust ratios. This can be also visualized in figure 5.7a, which plots the strength of the suction peak in time. Figure 5.7a shows that the suction peaks increase in strength at a rate that is proportional to gust ratio, but collapse on a single curve during their decay. The evolution of GR = 0.25 is different, and instead of a coherent LEV-associated peak, a laminar separation bubble forms near the leading edge and induces a pressure plateau.

The differences in pressure distribution between gust ratios in figure 5.5 are partly due to the differing dynamic pressures induced by the gust. To isolate the effects of incidence from the effects of inflow strength, figure 5.6 depicts the same distributions but nondimensionalized using the total dynamic pressure of the freestream and gust flow. This is equivalent to scaling the original definition of pressure coefficient by $\mathrm{GR}^2 + 1$. Using this normalization, the initial secondary suction peak is of similar strength for each of the gust ratios, as shown in panel (c) of figure 5.6. As a result of this and the previous discussion on suction peak decay, this normalization results in suction peaks that are weaker with increasing gust ratio. This can be seen in panel (f) of figure 5.6 as well as the inset of figure 5.7a, which displays the same peak strengths as the main figure, but normalized by $\mathrm{GR}^2 + 1$. In the inset, the growth rates and maximum suctions for each case possessing a LEV are collapsed until $t^* = 1$, after which the suction is higher for lower gust ratios. These trends are manifestations of the competing effects of vortex strength and vortex-wall distance. High gust ratios produce stronger vortices that result in large initial suction peaks. However, higher gust ratios also result in larger separation angles and faster convection of the vortex

away from the wing, resulting in the behavior summarized in figure 5.7a.

The behavior of the center of pressure of the wing is also dominated by the dynamics of the vortex or lack thereof. Figure 5.7b plots the chordwise ordinate of the center of pressure of the wing for different gust ratios. For GR = 0.25, the center of pressure starts at approximately 40% of the chord at gust entry and moves up to the quarter chord by $t^* = 1$. This is inline with Kussner's inviscid result for attached flow gust encounters, which states that the center of pressure for a wing fully immersed in a transverse gust is at the quarter chord [105]. The center of pressure then gradually returns to 40% of the chord after recovery. For the other cases which exhibit a coherent LEV, the centers of pressure are again at approximately 40% of the chord at gust entry. During the early phases of the gust encounter, the centers of pressure shift towards to the leading edge, each one reaching a minimum denoted by black markers on the plot. These minima are closer to the leading edge with increasing gust ratio, and also occur earlier in time with increasing gust ratio. Immediately following each minimum is a stage where the center of pressure shifts towards the trailing edge, overshooting its gust entry value. The rate of this center of pressure movement is proportional to gust ratio. The centers of pressure then gradually recover back to their gust entry values.

5.4 Pressure sensing

5.4.1 Integrated pressure distributions

This section of the results investigates the use of pressure sensors as a platform for flow sensing during gust encounters. When dense pressure measurements are available, the pressure integration procedure discussed in section 3.7.3 can be used to estimate the loads during a gust encounter. Figure 5.8 shows the lift, drag, and

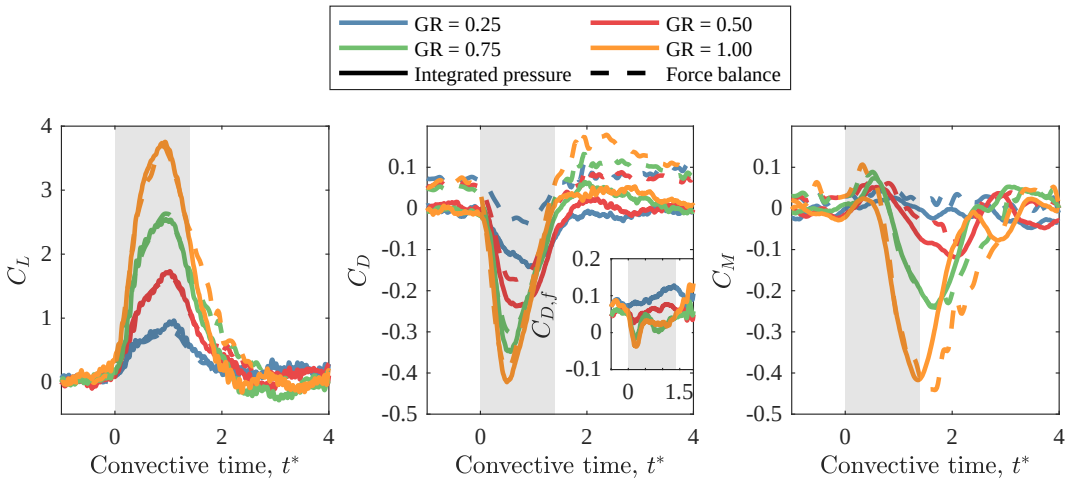

Figure 5.8: Lift, drag, and moment coefficients during gust encounters at four different gust ratios. Both force balance and pressure integrated loads are displayed.

moment coefficients for different gust ratios, as measured by the force balance (FB) and also as computed by integrating pressure (IP). The IP lift coefficient is in near perfect agreement with the FB lift coefficient while the wing is fully immersed in the gust, across all gust ratios. This agreement can be attributed to the analysis presented in section 3.7.5 and the results from section 5.2. In other words, for steady flows and unsteady flows with attached LEV's, the sectional lift coefficient is representative of the overall load coefficient. The timescale of these gust encounters is shorter than the vortex formation timescale and so the vortex remains attached for the duration of these gust encounter [41]. However, as the wing exits the gust the feeding shear layer is forced to interact with the secondary vorticity and the vortex detaches. The vortex detachment sets in motion the aforementioned lift undershoot behavior previously discussed and shown in figure 5.8 during gust exit. The lift undershoot of the IP lift increases with gust ratio and is not present for the GR = 0.25 case where a coherent LEV does not form.

As expected, the IP drag coefficient outside the gust is very near 0 and does not

capture the skin friction drag evident in the FB drag coefficient. During the gust encounter the drag is measured to be negative by both the IP and FB measurements. [1] While there is always a discrepancy between FB and IP drag coefficients due to skin friction, the discrepancy decreases as the gust ratio increases. That is, the drag becomes increasingly dominated by pressure as the gust ratio increases. This is shown in the inset figure 5.8, which plots the difference between IP and FB drag measurements. The moment coefficients follow similar trends as the lift coefficients. The IP measurements follow the FB closely during the gust encounter. After the gust exit, the IP moment coefficents undershoot the FB moment coefficients.

5.4.2 Leading-edge suction and pressure gradient

Pressure distributions are rarely densely resolved during operation. Outside of the laboratory, a few pressure measurements are typically available, tasked with probing specific flow characteristics. The leading edge is a good candidate for sensor placement, as measurements there can provide useful information pertaining to flow events related to stall. Pressure at the leading edge can be used to extract the leading-edge suction, a quantity whose criticality can be used estimate the shedding of vorticity at the leading edge [46, 100, 101]. Using the present measurements and the procedure described in section 3.7.3, the experimental leading-edge suction coefficient, $\mathcal{L}$ can be

[1] This anomalous measurement is a result of the axis system used to define the load coefficients. Lift and drag are defined to be perpendicular and parallel to the freestream velocity vector. In other words, the gust is treated as a disturbance and does not change the orientation of the lift and drag vectors. Redefining drag to be parallel to the inflow velocity gives the expected result of positive drag.

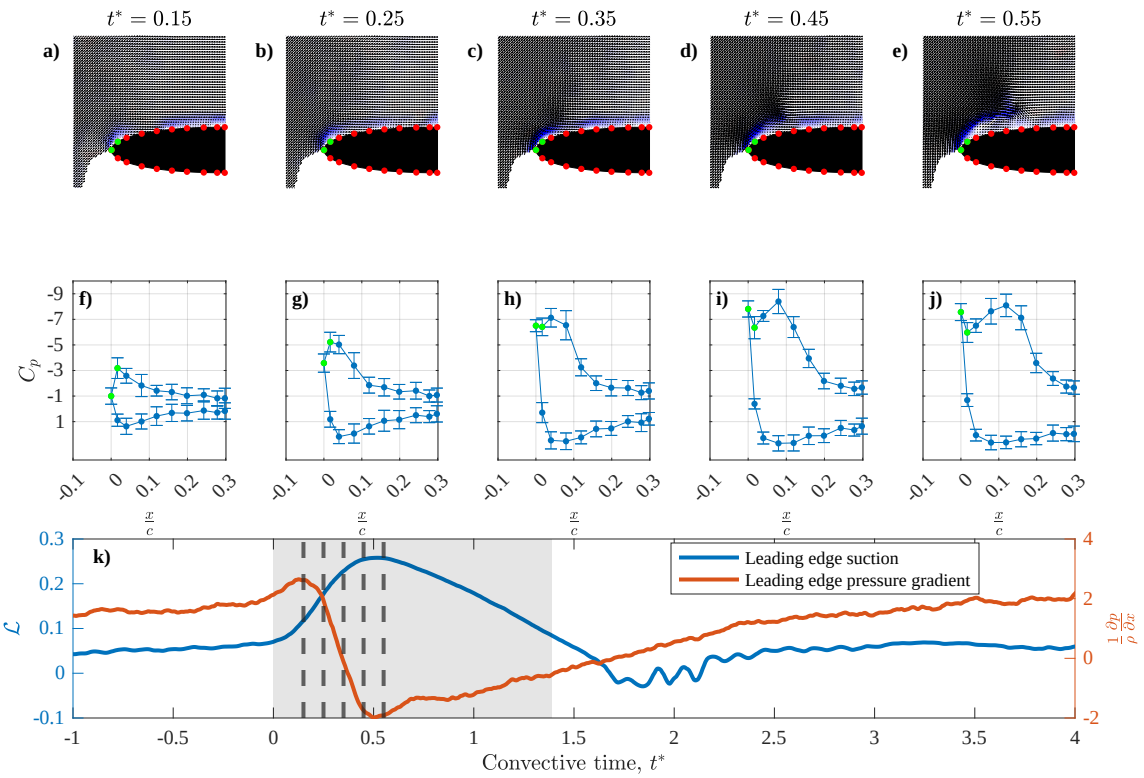

Figure 5.9: Evolution of the flowfield, pressure distribution, leading-edge suction, and leading-edge pressure gradient during separation at GR = 1. Panels (a)-(e) display vorticity contours and velocity vector fields, panels (f)-(j) display the pressure distributions, and panel (k) displays the leading-edge suction coefficient, $\mathcal{L}$, and the pressure gradient computed using the sensors marked with green in the previous panels. The vertical dash lines in panel (k) correspond to the timesteps associated with panels (a)-(j).

defined as [79]

$$\mathcal{L} = \begin{cases} \text{sgn}(F_{N,\text{LE}})\sqrt{\frac{F_{A,\text{LE}}}{2\pi q_\infty c}}, & \text{for } F_A > 0, \\ 0, & \text{for } F_A \leq 0. \end{cases} \tag{5.1}$$

where the leading-edge normal and axial forces, $F_{N,\text{LE}}, F_{A,\text{LE}}$, are computed by summing the load contribution from panels on the leading edge, defined to be the leading 30% of the chord.

Another quantity that is known to be critical during leading-edge stall is the

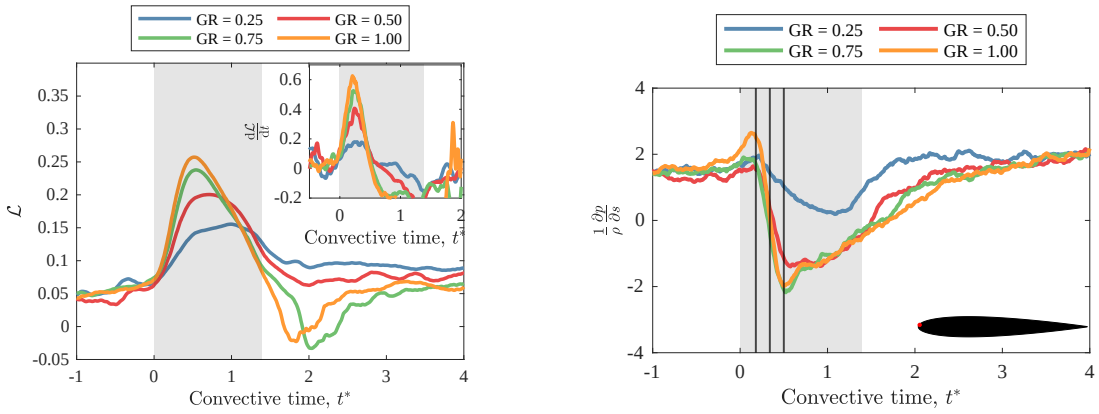

Figure 5.10: Quantities derived from pressure on the leading-edge. Figure (a) displays the leading-edge suction coefficient, $\mathcal{L}$, and (b) displays the leading-edge pressure gradient as function of convective time for four different gust ratios. The inset displays the time derivative of the leading-edge suction data.

pressure gradient at the leading edge. While always subject to discretization errors, the pressure gradient can be estimated using finite differences of the measured pressure distribution. This section analyzes the evolution and criticality of these derived quantities during the gust encounters being studied.

Figure 5.9 examines the evolution of leading-edge separation for the case GR = 1. Panels (a)-(e) depict out-of-plane vorticity contours along with the velocity vectors for the leading 30% of the chord. Panels (f)-(j) depict the corresponding pressure measurements, and panel (k) depicts the leading-edge suction coefficient, $\mathcal{L}$, as well the pressure gradient at the leading edge, computed as a finite difference using the sensors marked in green in the other panels. At $t^* = 0.15$, the vorticity contours and the pressure distribution show that the flow accelerates around the leading edge and only starts to decelerate between the first and second sensors on the top surface, evident by the favorable pressure gradient in panel (k). At this timestep, this favorable pressure gradient has reached a maximum and the leading-edge suction coefficient is

rapidly increasing. At $t^* = 0.25$, the velocity vectors indicate an onset of a wall-normal velocity component near the leading-edge surface and the leading-edge suction reaches an inflection point (its growth rate begins to decreases). By $t^* = 0.35$, the secondary suction peak discussed in section 5.3.1 has appeared in the pressure distribution and significant surface normal velocities are present in the resolved portion of the boundary layer. The leading-edge suction is still increasing, albeit at a slower rate, and the leading-edge pressure gradient has crossed the x-axis due to the formation of the secondary suction peak. At $t^* = 0.45$, vorticity can be seen lifting off the surface and the leading-edge suction reaches its maximum, while the pressure gradient at the leading edge has reached a minimum. Subsequently, the vortex begins convecting in the chordwise direction, the leading-edge suction begins decreasing, and the pressure gradient begins increasing.

The above data suggest that during gust encounters the onset of stall takes place before the leading-edge suction reaches its maximum value. Instead, the flowfields and pressure distributions suggest that the onset of the dynamic stall process corresponds to the point where the suction growth rate begins to diminish, and the maximum suction coefficient corresponds to the onset of vortex lift-off and chordwise convection. This can be more clearly seen in figure 5.10a, which plots the suction coefficients for each of the gust ratios, while its inset plots their time derivative. The data shows that for each of the gust ratios that exhibit coherent vortex formation, GR $\in [0.5, 0.75, 1]$, the suction coefficients reach their inflection points (where their derivatives have a maximum) at approximately the same time, $t^* \approx 0.2$. Further, each of the suction coefficients reach their maximums at approximately $t^* \approx 0.5$. This observation is useful to the design of gust alleviation controllers that use flow sensors. An inflection in suction coefficient can provide information on the timing of the vortex formation process during a severe gust encounter, while its maximum can provide information

on the timing of the vortex convection initiation phase.

While the timing of the suction coefficient evolution is independent of gust ratio, the magnitude of the suction coefficient is dependent on gust ratio, as shown in figure 5.10a. This was previously explored in Narsipur et al. [79], who investigated the variation of leading-edge suction with unsteady parameter variation. This variation is problematic to a flow sensing framework using leading-edge suction, since the gust ratio is a parameter that is not known a priori. The leading-edge pressure gradient provides an alternative way of sensing vortex formation processes. Each of the vortex formation events discussed above are also reflected in the leading-edge pressure gradient transients, shown for each gust ratio in figure 5.10b. The first signs of stall at $t^* \approx 0.2$ correspond to the sudden drop in leading-edge pressure gradient (first vertical line). The formation of the secondary peaks corresponds to the pressure gradient crossing the x-axis (second vertical line), and the onset of vortex convection corresponds to the rise in leading-edge pressure gradient (third vertical line). In contrast to the leading-edge suction, the variation of leading-edge pressure gradient between different gust ratios is a small percentage of the overall variation during a gust encounter. In other words, each case takes a similar pressure gradient trajectory through the gust encounter. Thus, the leading-edge pressure gradient can provide gust ratio invariant information to a gust alleviation controller.

The case GR = 0.25 has the same suction coefficient inflection and pressure gradient drop timing but its subsequent evolution is different. The pressure gradient at the leading edge never crosses the $x = 0$ line (no secondary peak formation), and its suction coefficient continues to increase until the effective angle of attack begins decreasing at $t^* \approx= 1$.

5.5 Chapter summary

This chapter analyzes simultaneous flowfield, load, and pressure distribution measurements of gust encounter flows. A surface pressure measurement wing model capable of simultaneous pressure and load measurements is developed and is validated using steady and unsteady test cases. It was shown that pressure integration can capture the overall wing lift while the leading edge is inside the gust but undershoots the overall lift after the wing exits the gust and the vortex detaches.

Analysis of the transient flowfields and pressure distributions detailed the following event sequence for high gust ratio experiments: While $t^* < 0.2$, the flow remains attached and a large suction peak forms on the leading edge. As time progresses, the suction widens and eventually splits into two distinct peaks. The first is associated with the acceleration of the flow around the leading edge and the second with the concentration of vorticity near the surface. Eventually, the concentrated vorticity lifts off the surface and a coherent vortex forms. The initial location of the secondary peak is found to be independent of gust ratio and its strength is found to be proportional to the gusting flow dynamic pressure, i.e., GR^2+1. Leading-edge flow sensing techniques for gust encounters were also investigated. Specifically, the behavior of the leading-edge suction coefficient and the leading-edge pressure gradients were analyzed. The onset of stall is found to take place when the leading-edge suction reaches an inflection point. A peak in leading-edge suction is found to correspond with vorticity lifting off the surface. The pressure gradient computed at the leading edge was found to contain useful signatures for each of the events during the gust encounter. The initiation of stall causes the pressure gradient to decrease. The formation of the secondary suction peak takes place when the pressure gradient crosses the x-axis, and the detachment of the vortex causes an increase in leading-edge pressure gradient.

Chapter 6: Inviscid modeling applications

This chapter investigates the use of inviscid models in different flow sensing and control applications during transverse gust encounters. The chapter is organized into three sections. The first section discusses the development of a low-order inviscid model that can calculate unsteady pressure distributions associated with leading-edge vortex flows. The second section develops an analytical relation between the pressure at the leading edge and the strength of the leading-edge vortex sheet. The third section discusses the development of optimal gust mitigation kinematics using Theodorsen's model and the Simplified Iterative Maneuver Optimization (SIMO) procedure, developed in Xu et al. [113].

6.1 Application I: Low-order unsteady pressure computation

In this section we develop a low-order numerical procedure to calculate unsteady pressure distributions associated with leading-edge vortex flows. We compare the generated values with experimental measurements and study the effects of separation on the pressure distribution of a wing in a gust encounter.

6.1.1 Computing inviscid, unsteady pressure

In this method, the wing is represented by a closed vortex sheet that also models its thickness (as opposed to thin-airfoil bound vortex sheets). The leading and trailing

edge shed vorticity distributions are represented by free vortex sheets attached to the bound vortex sheet, while gusts are represented by the appropriate point vortex distributions or boundary conditions. This representation of the flowfield is shown in figure 6.1. The pressure distribution on the wing can be computed using the unsteady Bernoulli equation,

$$C_p(s) = 1 - \left(\gamma_b^2(s) + 2\frac{\partial \phi(s)}{\partial t} \right) \frac{1}{U_\infty^2} \tag{6.1}$$

While this representation is convenient, there are several theoretical details about this system need to be addressed. First, since we are interested in computing the pressure on the surface of a wing with thickness, the bound vortex sheet must form a closed loop, a shown in figure 6.1. This is problematic for the computation of the unsteady potential in equation (6.1). In chapter 2, it was shown that the potential jump of a vortex sheet is related to the local circulation of the vortex sheet as

$$\frac{\partial \phi}{\partial s} = -\frac{\partial \Gamma}{\partial s} \tag{6.2}$$

However, for closed vortex sheets, equation (6.2) can only yield the potential up to a time-dependent integration constant. This is because it is topologically impossible for a closed circulation contour to cross the bound vortex sheet just once. In order to form a closed loop, the contour needs to cross the bound vortex sheet at least twice, and after integration, the value of the circulation at either intersection needs to be specified to compute the potential. Unfortunately, this information is not available, and the pressure distribution of the representation in figure 6.1 cannot be determined using Bernoulli's equation.

Fundamentally, this issue arises because the method first solves for the bound vortex sheet strength and then integrates the sheet to obtain the potential. A workaround

to this problem is to instead solve directly for the potential on the surface instead of the bound vortex sheet. This entails replacing the bound vortex sheet with a bound doublet sheet, μ (also called a double layer potential), whose strength is exactly the jump in potential on the body. To carry out this replacement we can relate the induced velocities of vortex sheets and doublet sheets to create equivalent distributions. An important theoretical detail is that the bound doublet sheet strength cannot be assumed to be continuous. This is because intersections with the leading-edge and trailing-edge vortex sheets will cause tangential discontinuities in the potential. To relate the induced velocities we use a vector identity proven in Eldredge [31] which reads,

$$\overbrace{-\nabla \times \int_S G(\boldsymbol{x}-\boldsymbol{y})\, \mathbf{n}_y \times \nabla_y \mu(\boldsymbol{y})\, dS(\boldsymbol{y})}^{\text{Vortex sheet}} = \underbrace{-\int_{C_D} [\mu(\boldsymbol{y})]_-^+ \nabla G(\boldsymbol{x}-\boldsymbol{y}) \times d\mathbf{l}(\boldsymbol{y})}_{\text{Discontinuity}} + \underbrace{\nabla \int_S \mu(\boldsymbol{y})\, \mathbf{n}_y \cdot \nabla G(\boldsymbol{x}-\boldsymbol{y})\, dS(\boldsymbol{y})}_{\text{Doublet sheet}}$$

where S is the surface the sheets are on, and C_D are the segments where discontinuities exist in μ. Since μ is the potential jump, the LHS represents the induced velocity of a vortex sheet with strength $\mathbf{n}_y \times \nabla_y \mu(\boldsymbol{y})$. The second term on the RHS is the induced velocity of a doublet sheet with strength $\mu(\boldsymbol{y})$, and the first term represents the effects of doublet sheet discontinuities In other words, a vortex sheet of strength $\mathbf{n}_y \times \nabla_y \mu(\boldsymbol{y})$ on a surface can be regarded as a doublet sheet of strength $\mu(\boldsymbol{y})$ on the same surface, plus a term accounting for discontinuities in the dipole distribution. These discontinuities capture the overall potential jump contribution from the attached shed vortex sheets. Since the shed vortex sheets are not closed, their potential jump can be computed using the circulation method described in section 2.2.2. Namely, their

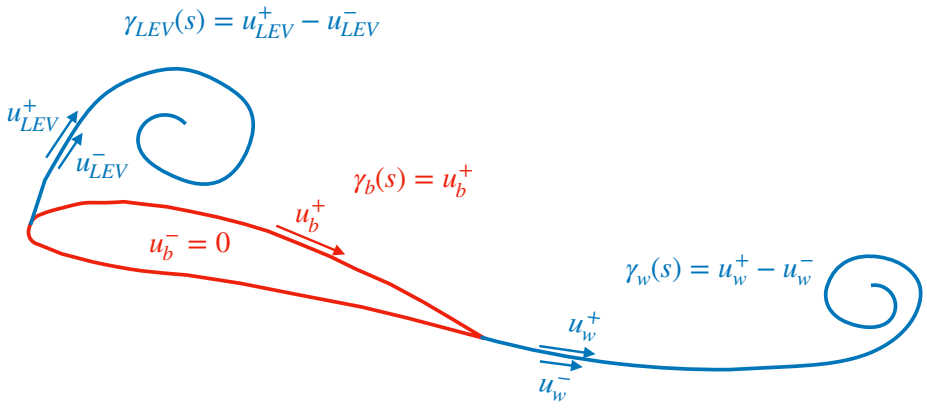

Figure 6.1: Vortex sheet representation of the flowfield

total potential jump contribution is the circulation of contours that completely enclose them and cut through the intersection point with the bound vortex sheet, as shown in figure 6.2. The bound doublet strength μ, is the jump in potential from the constant internal potential inside the wing to the potential outside the wing, $\mu = \phi - \phi_i$. Each of the edges contains a discontinuity in surface potential. For example the strength of the potential on either side of the leading edge is related by, $\phi^+_{LE} = \phi^-_{LE} + \Gamma_{LEV}$, where Γ_{LEV} is the circulation of the leading-edge vortex.

While the strength of the trailing edge vortex sheet can be determined using Kelvin's circulation theorem and the Kutta condition, the leading-edge vortex sheet needs to be modeled heuristically. The method of leading-edge suction first described in Ramesh et al. [88] and discussed in 2 provides a convenient route to its calculation. However, as it stands it can only be applied to thin-airfoil geometries. To bypass this issue, we solve the thin-airfoil problem on the camber line of the wing as well as the thick-airfoil problem on the wing's surface. The shed vorticity distributions are determined based on the thin-airfoil problem. Subsequently, the dipole distribution is solved for the given shed and gust vorticities. Figure 6.3 shows an example calculation of the flowfield and associated surface pressure during a wing-gust encounter. The

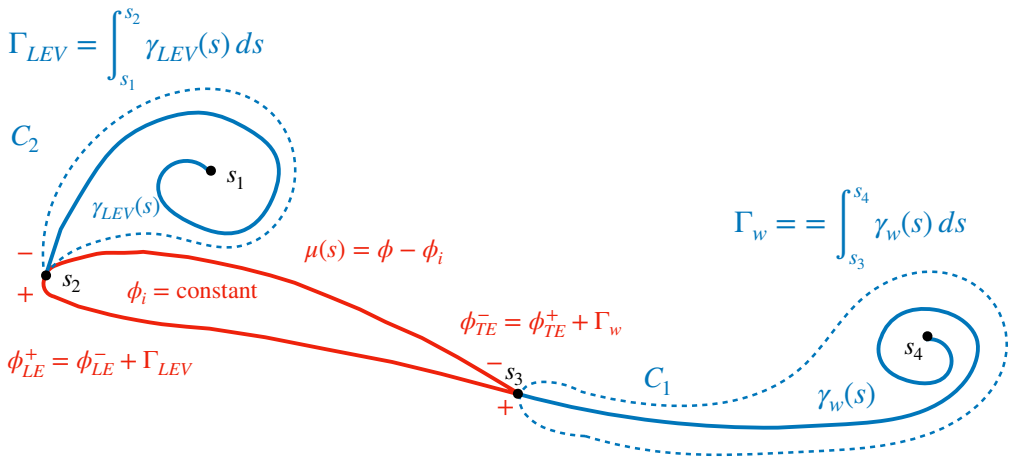

Figure 6.2: Bound doublet sheet distribution and its relationship to shed vorticity distributions

plot on the left in 6.3b is the velocity contribution to surface pressure, similar to the steady Bernoulli equation. The middle plot in 6.3b is the unsteady contribution to the pressure distribution. Note the the discontinuities at the leading and trailing edges. They are caused by the attached vortex sheets at either edge, and the size of the discontinuities is related to the rate of change of circulation of the attached vortex sheets. The plot on the right in 6.3b is the surface pressure distribution of the flowfield in figure 6.3a.

6.1.2 Effect of gust model

An important modeling choice pertains the representation of the gust in the flow. There are two ways one can model a gust: 1) As a velocity boundary condition, or 2) as flow vorticity. The velocity boundary condition approach is the most straightforward in both and implementation and computational complexity. A gust profile is assigned and any body under its influence must adjust its surface and shed vorticities to enforce the boundary conditions. The main disadvantage of modeling a gust in this way is the

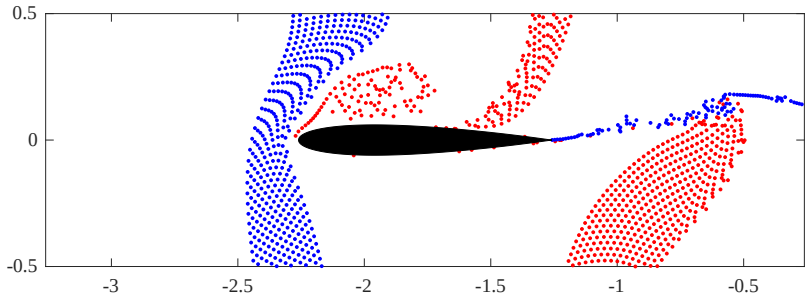

(a) Low-order calculation of a wing-gust encounter at $GR = 0.75$

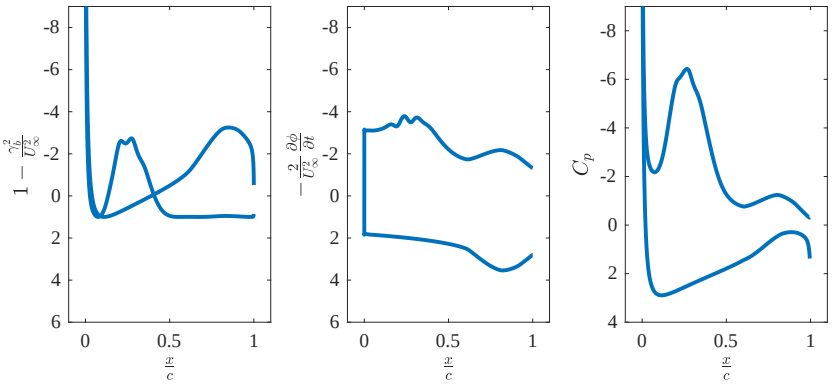

(b) Contributions to surface pressure from the unsteady Bernoulli equation.

Figure 6.3: Example calculation of the flowfield and associated surface pressure during a wing-gust encounter.

fact that it does not deform. The problem is one-way coupled and the wing cannot influence the properties of the gust. In contrast, the representation of the gust as flow vorticity is a two-way coupled problem. During the wing-gust encounter, the wing's bound and shed vorticities are deforming the gust shear layers in accordance with potential flow dynamics.

The way to construct a specific gust profile using flow vorticity is as follows: Regions of constant gust velocity are left empty. Regions of gust shear are modeled using a series of vortex sheets. Note that the strength of each vortex sheet is equivalent

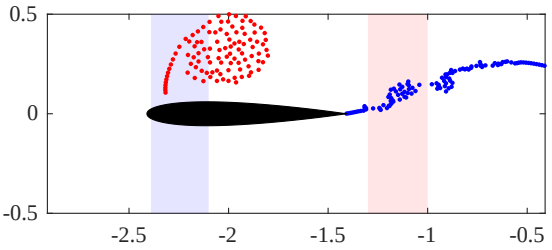

(a) Model of rigid gust as velocity boundary condition.

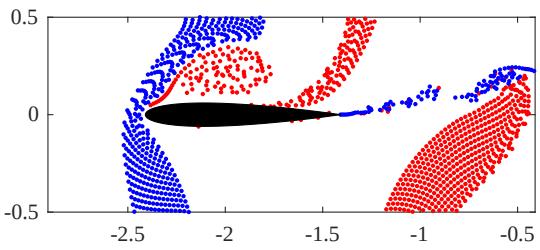

(b) Model of non-rigid gust as point vorticity distribution.

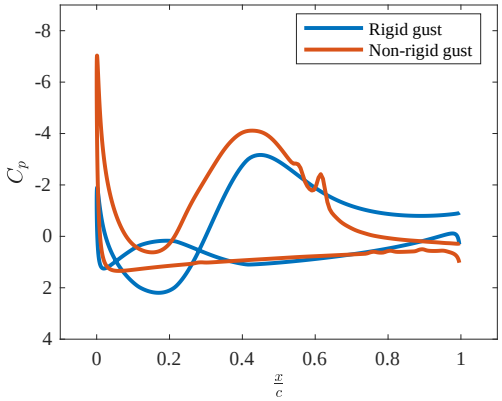

(c) Pressure distributions for rigid and non-rigid gusts associated with the flowfields in (a) and (b).

Figure 6.4: Two different ways gusts can be modeled in a low-order setting.

to a jump in its tangential velocity. Thus, if a smooth climb in gust velocity from 0 to V_g is desired, N vortex sheets can be used each one with strength V_g/N.

Figure 6.4 shows a snapshot from an example calculation of a wing-gust encounter at $GR = 0.75$, for both rigid and deformable gusts. Their associated pressure distributions are shown in figure 6.4c. The leading edge of the wing encountering the rigid gust has exited the gust. Consequently, the suction peak at its leading edge has diminished. In contrast, the wing encountering the non-rigid gust is still experiencing high velocity at its leading edge and possesses high loading in the first 15% of its chord. The biggest discrepancy between the two cases is the negative lift produced by the wing encountering the rigid gust at about 20% of its chord. This area of negative

lift propagates down the chord of the wing as it crosses the rigid shear layer. This phenomenon is neither present in the non-rigid gust case nor observed in experiment. It is an artifact created by the rigid gust assumption. As the wing crosses the rigid shear layers, it experiences large gradients in velocity. The large gradients induce unrealistic surface accelerations that produce this negative lift peak. For the remainder of this chapter all computations will use the non-rigid gust model.

6.1.3 Effect of leading-edge separation

One of the main advantages of the unsteady pressure model developed in section 6.1.1 is that leading-edge separation can be toggled based on the value of the critical leading-edge suction. For example, setting the critical value to infinity recovers the familiar attached flow dynamics. In this section we use this model along with experimental pressure measurements to investigate the effects of separation on the pressure distribution.

Figure 6.5 depicts the experimental pressure distributions at six different timesteps and four different gust ratios. Overlaid are also the pressure distributions predicted by the inviscid model without any leading-edge shedding ($\mathcal{L}_c = \infty$). The modeled pressure distributions correspond to those produced by the linear aerodynamics studied in chapter 4, with the additional effects of wing thickness, gust deformation, and dynamic wake modeling. For $GR = 0.25$, the inviscid and experimental pressures are in agreement, with the exception of the low gust ratio separation bubble near the leading edge seen in chapter 5. At $GR = 0.50$, the inviscid pressure distribution develops a large suction peak at the leading edge which grows in time during the gust encounter. While a suction peak does exist in the experimental pressures, it is much smaller in magnitude and also decreases in strength after the LEV starts propagating

downstream at $t^* = 0.75$. While this discrepancy may be attributed to the separation present in the experiments, it is also likely that the finite resolution of the pressure taps are unable to capture localized pressure peaks. There are two other obvious discrepancies between the experimental and inviscid pressures: 1) The LEV suction peak on the suction surface, and 2) the pressure side pressure which appears to be slightly higher in the experiments. These trends persist as the gust ratio increases. At $GR = 0.75$ and $GR = 1.00$, the suction peaks discrepancy increases, but the pressure difference between experiments and the model on the pressure surface also increases (see for example figure 6.5, panels (t)-(x)). This is unexpected and will be addressed later on in the text.

Figure 6.6 depicts the same experimental data as figure 6.5, but this time overlaid with the inviscid pressures that include the effects of leading-edge separation ($\mathcal{L}_c = 0.13$). For reference, figure 6.7 depicts the experimental vorticity contours along with the vorticity shed by the wing in the vortex model. For $GR = 0.25$, the leading-edge suction of the model does not exceed the critical amount and no leading-edge shedding takes place. For the rest of the gust ratios, the leading-edge suction does exceed the critical value and vorticity is shed from the leading edge, as depicted in figure 6.7. In general, the shed vorticity has the desired effect on the inviscid pressure distribution. The shed vorticity forms a LEV which induces a large suction peak on the suction surface. This is not true for $GR = 0.50$, where the shed vorticity in the model fails to roll up as in the experiments. Thus, no coherent suction peak forms on the surface. For $GR = 0.75$ and $GR = 1.00$, the vorticity rolls up and creates a suction of strength that is in agreement with measurements, but that initiates about a quarter of a convective time too late. This is not related to the onset of separation, but rather, to the dynamics of the separate shear layer after separation. An interesting suction surface discrepancy between the model and the experiments is the relatively

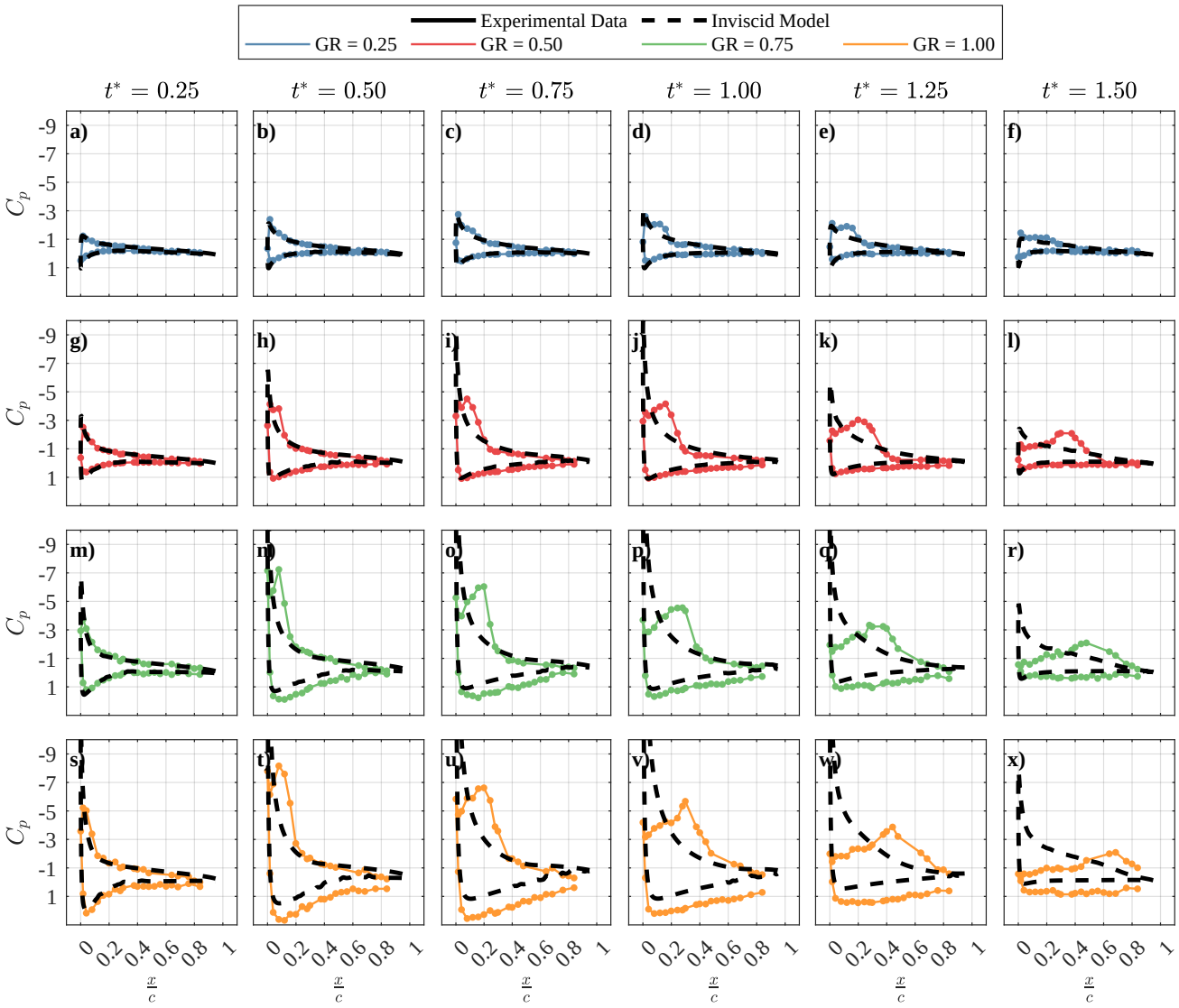

Figure 6.5: Pressure distribution during a gust encounter for four different gust ratios and at six different timestamps. Both experimental and inviscid model with no leading-edge separation are shown.

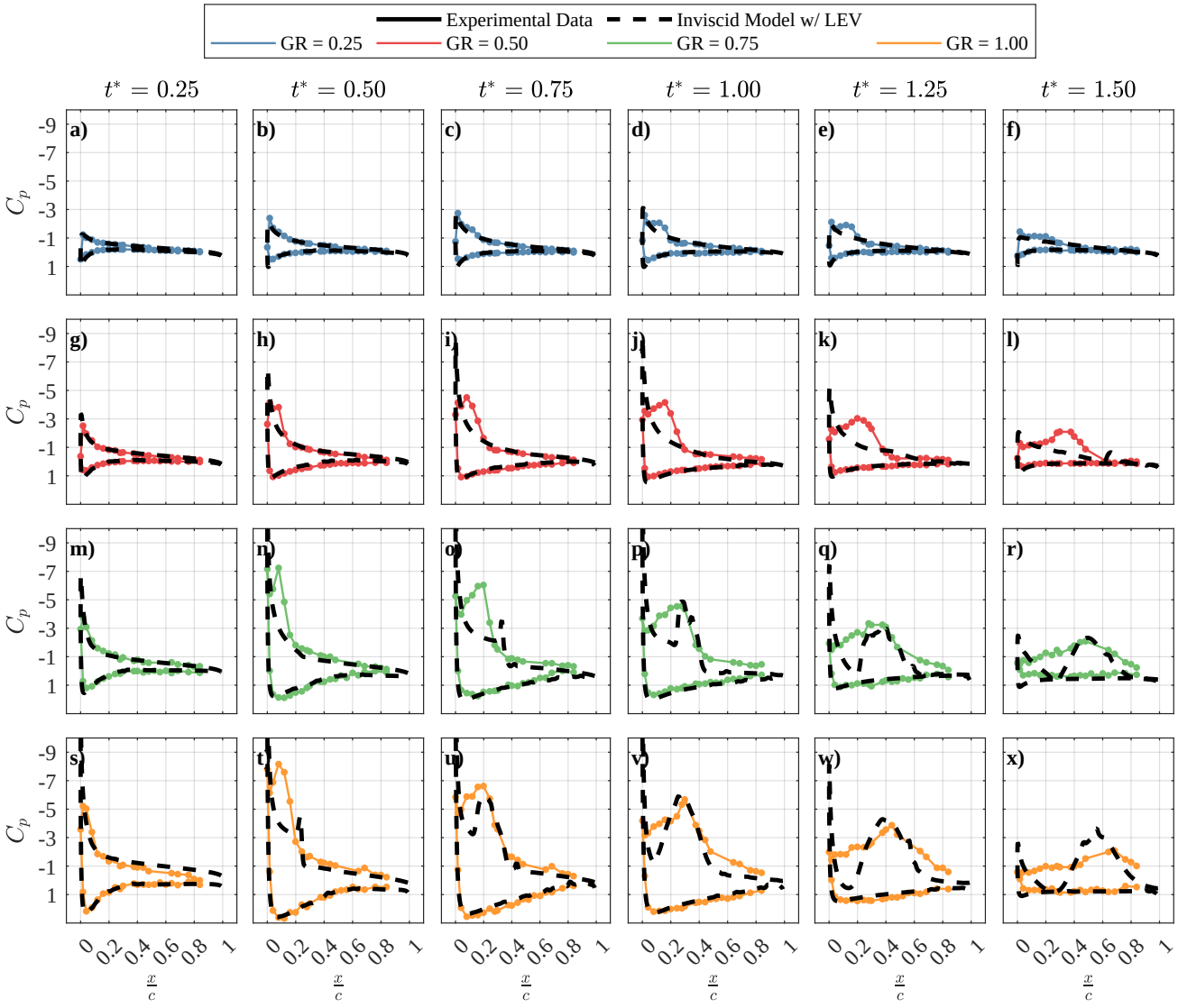

Figure 6.6: Pressure distribution during a gust encounter for four different gust ratios and at six different timestamps. Both experimental and inviscid model with leading-edge separation are shown.

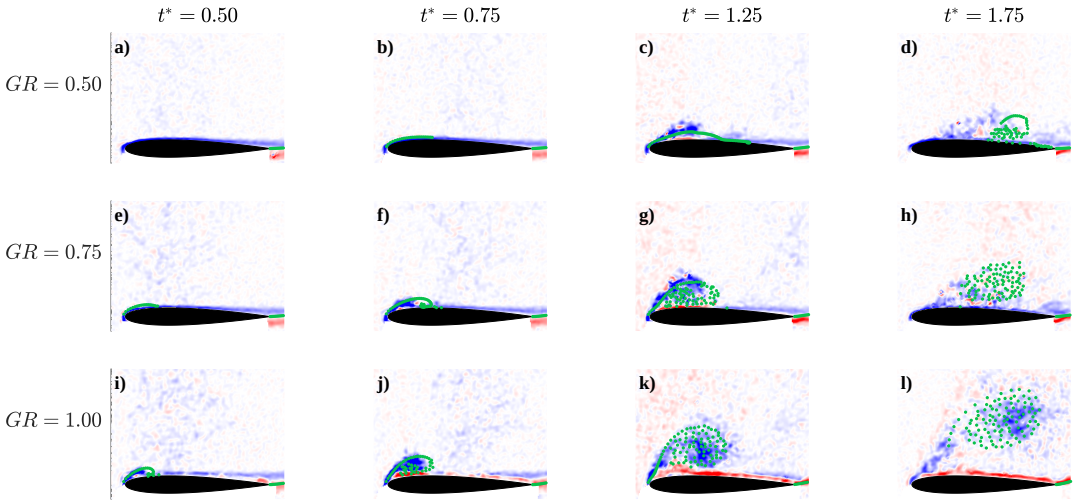

Figure 6.7: Experimental contours of vorticity overlaid with shed leading-edge vorticity in the inviscid model.

low pressure associated with secondary vorticity in the experiments. Even though inviscid dynamics capture the shed vorticity and its dynamics (see figure 6.6 panel (w) and 6.7 panel (k)), they fail to capture the effect of the secondary vorticity under the separated shear layer. This is more clearly seen in figure 6.8, which plots the suction side pressure signatures as contours in space and time. The experimental suction peak signatures are connected to the leading edge through a low pressure region (see region in $x/c \in [0, 0.2]$ in figure 6.8). This modeled signatures exhibit a sharp increase in pressure before reaching the leading edge. This effect, along with the lack of roll up for $GR = 0.50$ highlight scenarios where simply predicting the inviscid flowfield is inadequate and viscous-inviscid coupling is necessary.

The most surprising characteristic of the modeled pressure distributions is their phenomenal agreement with experiment on the *pressure side* of the wing. This is in contrast to the previous comparison of figure 6.5, which did not include leading-edge separation. Hence, modeling separation has the effect of increasing the pressure on the pressure side of the wing, and this increase in pressure matches the experimental

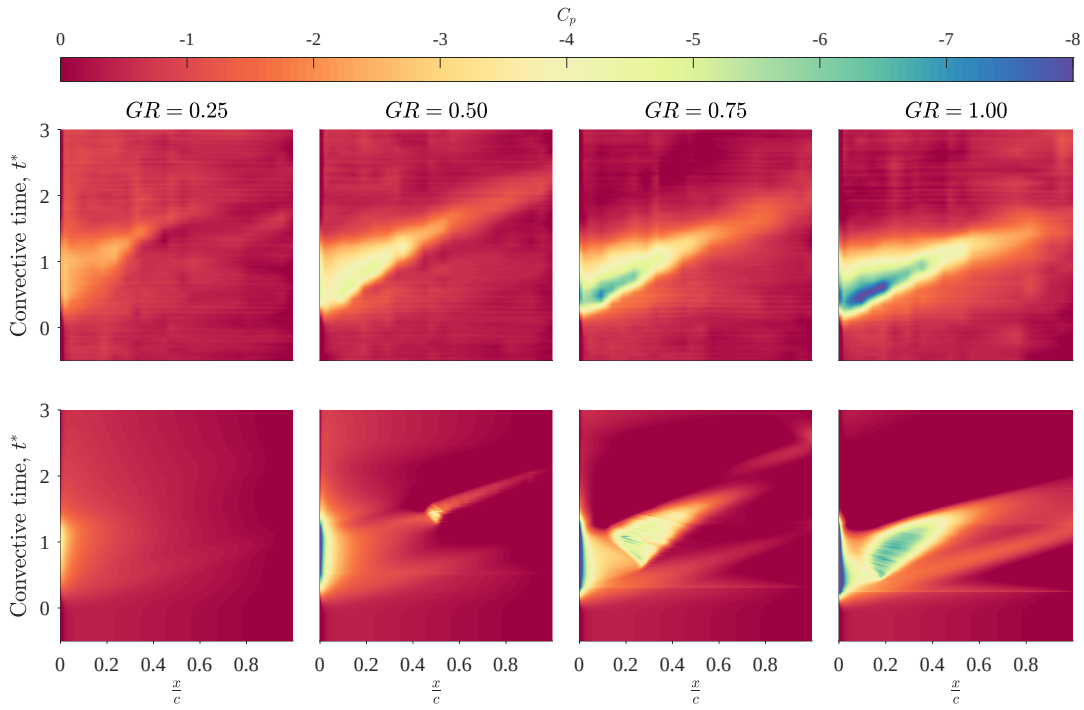

Figure 6.8: Pressure distribution on suction surface from the experiments (top row), and the inviscid model (bottom row).

data. This is seen for each of the gust ratios $GR \in [0.5, 0.75, 1.00]$ by comparing the pressure side agreement between figure 6.5 and 6.6. Figure 6.9 shows contributions to unsteady surface pressure of the inviscid pressure distribution shown in panels (u) of figures 6.5 and 6.6. The figure demonstrates that the attached flow model is able to capture the vortex sheet strength on the pressure surface, and the steady contribution to pressure is nearly identical for the two cases (only on the pressure surface). However, the attached flow model does not capture the correct unsteady contribution to pressure through the unsteady potential. The presence of leading-edge separation and LEV formation corrects for this inside the model. The unsteady potential in the Bernoulli equation can be hard to interpret physically. An alternative formulation for pressure in a fluid is the pressure Poisson equation. Eldredge and Le Provost [33] solve the pressure Poisson equation equation for an unbounded viscous

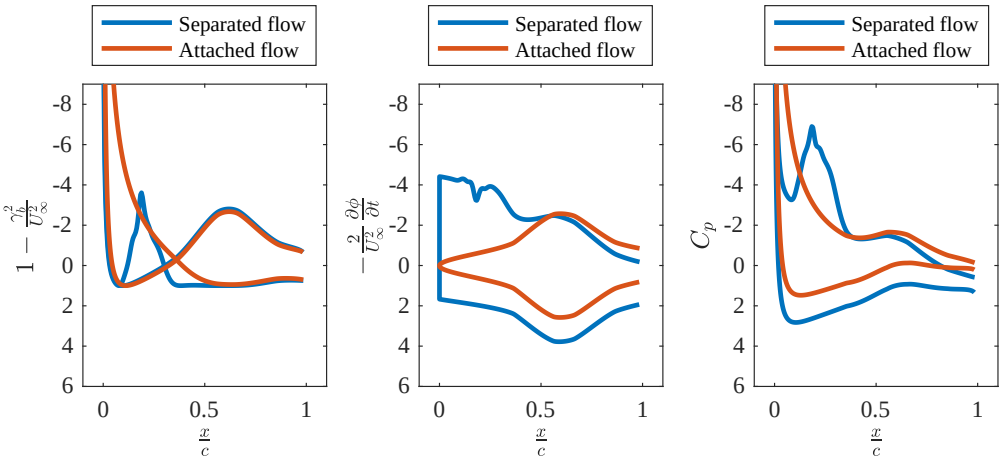

Figure 6.9: Contributions to unsteady surface pressure of the inviscid pressure distribution shown in panels (u) of figures 6.5 and 6.6.

fluid and make a connection between the unsteady potential and more familiar flow quantities. When applied to the above flow, the solution reads,

$$C_p(\boldsymbol{x}) = 1 - \frac{|\boldsymbol{u}(\boldsymbol{x})|^2}{U_\infty^2} + \frac{2}{U_\infty^2}\int_{\boldsymbol{y}} \nabla G(\boldsymbol{x}-\boldsymbol{y}) \cdot (\boldsymbol{u}(\boldsymbol{y}) \times \boldsymbol{\omega}(\boldsymbol{y}))\, dV(\boldsymbol{y}) \qquad (6.3)$$

where $G(\boldsymbol{x})$ is the Green's function of the Laplace operator. By comparison to the unsteady Bernoulli equation (6.1), the second term on the RHS of equation (6.3) can be identified to contain the effect of the unsteady potential. This term requires an integral of the flow Lamb vector $(\boldsymbol{u}(\boldsymbol{y}) \times \boldsymbol{\omega}(\boldsymbol{y}))$, which is associated with vector force [61]. Thus, the extra pressure on the wing's pressure side in the presence of an LEV can be associated to the vector force of the LEV.

6.2 Application II: Leading-edge vortex sensing

The LEV has dominant influence on the surface pressure distribution during a gust encounter. This motivates the following: Is it possible to relate surface pressure to vortex characteristics? This is the subject of this section.

6.2.1 Attached vortex sheet model

In order for the problem to be analytically tractable, thin-airfoil theory is used. Specifically, we consider the following structure shown in figure 6.10: A thin-airfoil bound vortex sheet, γ_b is attached to a vortex sheet at its leading edge, γ_{LEV} and a vortex sheet at its trailing edge, γ_w. Kelvin's circulation theorem states that the overall circulation of the system must be 0,

$$\int_{s_2}^{s_3} \gamma_b(s)\, ds + \int_{s_3}^{s_4} \gamma_w(s)\, ds + \int_{s_1}^{s_2} \gamma_{LEV}(s)\, ds = 0 \tag{6.4}$$

Bernoulli's equation for the pressure difference on the bound vortex sheet is,

$$\Delta C_p(s) = \frac{2}{U_\infty^2}\left(u_\tau(s)\gamma_b(s) - \frac{\partial \phi}{\partial t}\right) \tag{6.5}$$

where $u_\tau(s)$ is the local tangential velocity induced by the flowfield on that particular point (excluding the contribution of the bound vortex sheet). For example, for a wing at an angle of attack α, encountering a transverse gust of strength V, $u_\tau(s) = U_\infty \cos(\alpha) + V \sin(\alpha)$. We postulate that the point connecting the bound vortex sheet and the leading-edge vortex sheet might yield important information about the LEV. For this reason, we consider the contour C_1, which encloses the bound vortex sheet and the wake vortex sheet, shown in figure 6.10. The circulation of this contour is,

$$\Gamma_1 = \int_{C_1} \boldsymbol{u} \cdot\, d\boldsymbol{\ell} = \int_{s_2}^{s_3} \gamma_b(s)\, ds + \int_{s_3}^{s_4} \gamma_w(s)\, ds \tag{6.6}$$

$$= -\int_{s_1}^{s_2} \gamma_{LEV}(s)\, ds = -\Gamma_{LEV} \tag{6.7}$$

where in the last step we have used Kelvin's circulation theorem (6.4) to replace the circulation inside the contour with the remaining circulation outside the contour, i.e.,

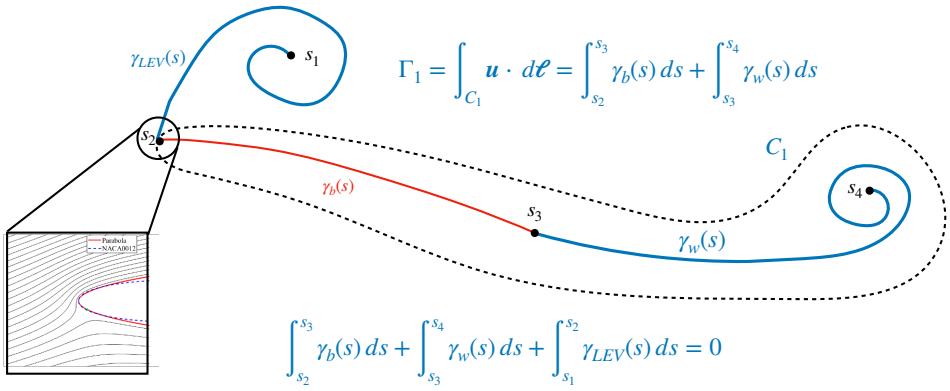

Figure 6.10: Schematic of the attached vortex sheet model

the LEV circulation. We can now use this result to evaluate the unsteady Bernoulli equation at the leading edge,

$$\Delta C_p(s_2) = \frac{2}{U_\infty^2}\left(u_\tau(s_2)\gamma_b(s_2) + \frac{\mathrm{d}\Gamma_{LEV}}{\mathrm{d}t}\right) \tag{6.8}$$

This is an interesting result. It tells us that pressure difference at the leading edge is a function of the velocity at the leading edge and the rate of change of the LEV circulation. However, in its current form this equation is not useful since the vortex sheet strength and pressure difference are singular at the leading edge. This is a mathematical artifact of thin-airfoil theory resulting from the flow having to turn around a sharp corner, and not a physical phenomenon. This singularity will be addressed in the next section.

6.2.2 Resolution of the leading-edge singularity

In thin-airfoil theory, the singularity at the leading-edge is integrable and does not prohibit calculation of quantities such airfoil loads. There are applications however, where it does cause issues. For example, for the purpose of LEV sensing, we are

trying to relate measurements at the leading edge with theoretical thin-airfoil values. The singularity was first resolved by Lighthill [67] and the procedure was formalized by Van Dyke [104]. The process involves a Matched Asymptotic Expansion (MAE) of the thin-airfoil singular solution with a non-singular representation of the leading edge flow. In this section we will use MAE similar to that described in Ramesh [87].

Outer Solution:

The outer solution of the expansion is the familiar thin-airfoil theory presented in chapter 2, with bound vortex strength,

$$\gamma_b(\theta, t) = 2U_\infty \Big(A_0(t) \frac{1 + \cos(\theta)}{\sin(\theta)} + \sum_{n=1}^{\infty} A_n(t) \sin(n\theta) \Big) \tag{6.9}$$

Note the singularity $\theta = 0$, $\gamma_b = \infty$. The pressure difference on the sheet is,

$$\frac{\Delta p(x)}{\rho} = u_\tau(x)\gamma_b(x) + \frac{\partial}{\partial t} \int_0^x \gamma_b(x)\, dx \tag{6.10}$$

Plugging equation (6.9) in equation (6.10) and taking the limit as $x \to 0$ leads to,

$$\frac{\Delta p(x)}{\rho} = 2U_\infty A_0 \sqrt{\frac{c}{x}} u_\tau(x) + 4U_\infty \dot{A}_0 \sqrt{cx} \tag{6.11}$$

Inner Solution:

The inner solution will be based on approximating the flow near a rounded leading-edge with the potential flow over a parabola. The flow over a parabola can be analytically derived using a conformal mapping of the well-known stagnation point flow. See Deparday et al. [25] and Ramesh [87] for the full derivation. The key parameters are U and V, which control the stagnation and parallel flows, respectively, and r which controls the leading-edge radius. The conformal map and its parameters are demostrated in figure 6.11. The wall in the z-plane maps to a parabola in the ζ-plane.

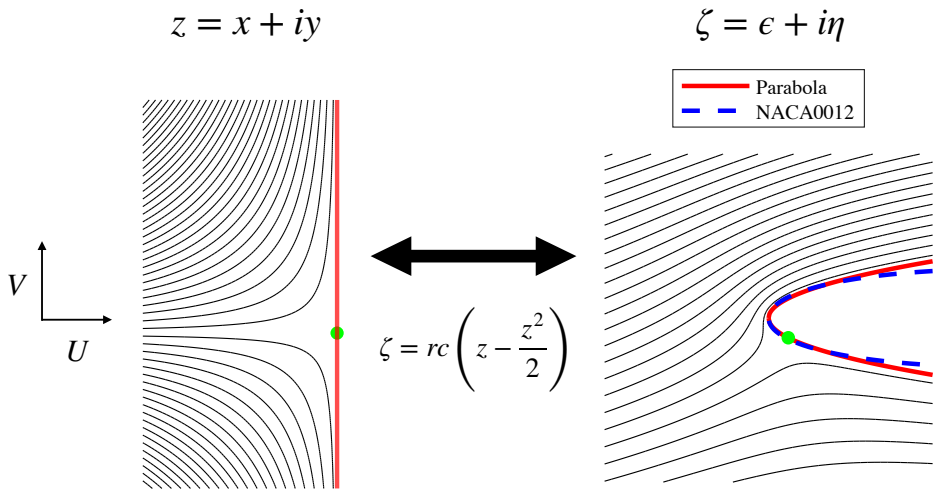

Figure 6.11: Conformal map of the stagnation point flow to the flow over parabola

By changing the ratio of the stagnation and parallel velocities, the angle of attack is adjusted in the ζ-plane and the stagnation point moves on the surface of the parabola.

The pressure difference on the parabola is derived reads,

$$\frac{\Delta p(x)}{\rho} = \frac{2\sqrt{2x}UV}{rc\sqrt{rc}(2x + rc)} + 2\dot{V}\sqrt{\frac{2x}{rc}} \tag{6.12}$$

Taking the limit as $x \to \infty$ leads to the asymptotic expression,

$$\frac{\Delta p(x)}{\rho} = \frac{\sqrt{2}UV}{rc\sqrt{rcx}} + 2\dot{V}\sqrt{\frac{2x}{rc}} \tag{6.13}$$

The expressions for pressure (6.11) and (6.13) can be set equal to each other as they are both valid in the intermediate region. The result is a relationship between thin-airfoil parameters and the stagnation point flow variables,

$$U = rcu_\tau \tag{6.14}$$

$$V = \sqrt{2r}U_\infty A_0 \tag{6.15}$$

This allows us to evaluate properties at the leading edge of a thin-airfoil with leading-edge radius r. For example, the velocity and the unsteady potential near the leading edge of the airfoil become

$$u(x) = \frac{\sqrt{x}u_\tau \pm \sqrt{c}U_\infty A_0}{\sqrt{x + \frac{rc}{2}}} \tag{6.16}$$

$$\frac{\partial \phi}{\partial t} = \dot{u}_\tau \frac{x}{rc} \pm 2U_\infty \dot{A}_0 \sqrt{\frac{x}{c}} \tag{6.17}$$

With this information we can define the pressure coefficient near the leading edge as

$$C_p(x) = 1 - \left(\left(\frac{\sqrt{x}u_\tau \pm \sqrt{c}U_\infty A_0}{\sqrt{x + \frac{rc}{2}}} \right)^2 - 2\dot{u}_\tau \frac{x}{rc} \mp 4U_\infty \dot{A}_0 \sqrt{\frac{x}{c}} \right) \frac{1}{U_\infty^2} \tag{6.18}$$

This is a complicated expression but simplifies considerably if evaluated at the leading edge where $x = 0$,

$$C_p^{LE} = 1 - \frac{2A_0^2}{r} \tag{6.19}$$

This substantial simplification is partly due to the fact that the unsteady potential term vanishes at the leading edge. This is inline with the analysis in section 6.2.1 which showed this is the case if no leading-edge vortex exists. This expression is also in agreement with Ramesh [87], who showed that the velocity at the leading edge is $u_{LE} = \sqrt{2/r}U_\infty A_0$

6.2.3 LEV strength estimation

Equation (6.19) relates the pressure coefficient at the leading edge with the A_0 Fourier coefficient from thin-airfoil theory. However, the leading-edge suction hypothesis states that A_0 does not exceed a critical value $\mathcal{L}_c$. Thus, equation (6.19) translates the critical leading edge suction to a critical leading-edge pressure coefficient at the

leading edge,

$$C_{p,c}^{LE} = 1 - \frac{2\mathcal{L}_c^2}{r} \tag{6.20}$$

From chapter 5, $\mathcal{L}_c \approx 0.13$. The radius of the NACA0012 leading edge can be estimated by fitting a parabola to its shape. In this study, fitting a parabola to 5% of the chord resulted in a value of $r = 0.015$. The parabola can be seen in figure 6.11. Using these values the critical pressure becomes $C_{p,c}^{LE} \approx -1.25$. Thus, we expect that for attached flows at this Reynolds number and geometry, the pressure coefficient will not exceed this critical value.

If the flow is separated at the leading edge, the contribution of the leading-edge vortex sheet to pressure as shown in section 6.2.1, needs to be accounted for. A vortex sheet at the leading edge introduces a contribution to the unsteady potential which takes the form of the rate of change of the leading-edge circulation, as demonstrated in equation 6.8. According to this model, any additional suction beyond the critical value must come from the rate of change of circulation of the leading-edge vortex sheet. The only other way for the pressure to decrease at the leading edge is by an increase in velocity. However, at the point of separation the velocity has reached its maximum value as postulated by critical suction hypothesis. This allows us to attribute any excess pressure beyond the critical pressure value to leading-edge circulation,

$$C_p^{LE} = \overbrace{1 - \frac{2\mathcal{L}_c^2}{r}}^{C_{p,c}^{LE}} - \frac{2}{U_\infty^2}\frac{\mathrm{d}\Gamma_{LEV}}{\mathrm{d}t} \tag{6.21}$$

$$C_p^{LE} - C_{p,c}^{LE} = -\frac{2}{U_\infty^2}\frac{\mathrm{d}\Gamma_{LEV}}{\mathrm{d}t} \tag{6.22}$$

Figure 6.12a plots the measured pressure at the leading-edge for four different gust ratios. The critical pressure coefficient is also shown as a horizontal line. Each of

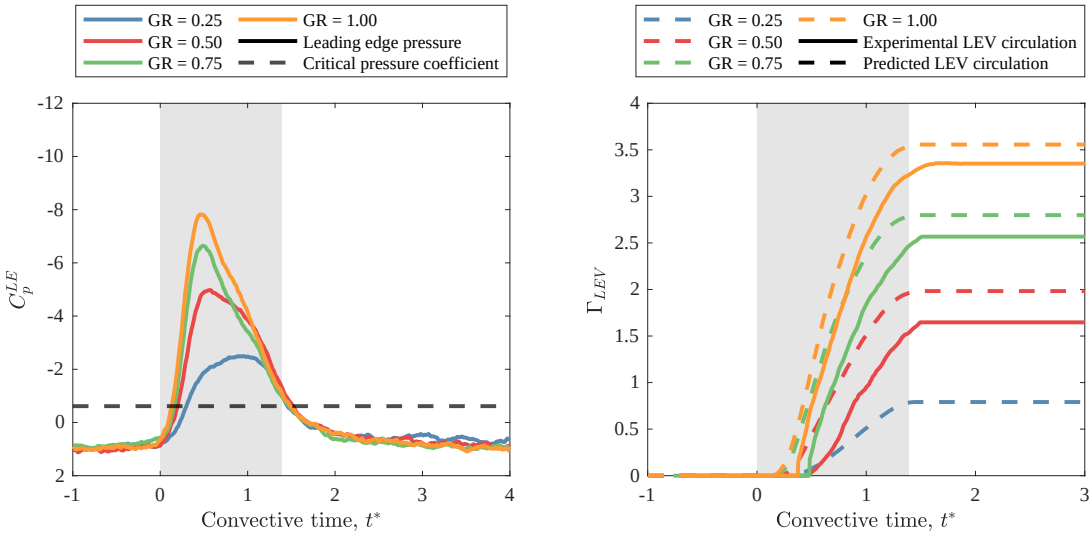

(a) Measurements of leading edge pressure coefficient for four different gust ratios.

(b) Experimental and predicted LEV circulations using the attached vortex sheet theory.

Figure 6.12: Leading-edge pressure measurements and the corresponding vortex circulation predictions.

the four cases exceeds the critical value. Figure 6.12b plots the experimental LEV circulations along with the predictions made using equation (6.22). There is fair agreement between the experimental and predicted values, although there are also pretty notable shortcomings. For example, while the theoretical prediction is able to capture the approximate rate of circulation production, it is not able to capture the timing of the production. For each of the gust ratios there is a significant gust ratio dependent delay between the predicted and the actual circulation values. This delay increases with decreasing gust ratio. The predicted final LEV circulation is also higher for each of the gust ratios. For $GR = 0.25$, the model predicts a significant LEV of strength $\Gamma_{LEV} \approx 0.75$, but this is not observed in the experiments. Nevertheless, the ability to get first-order estimates of the LEV strength with one sensor can be valuable in many scenarios.

There are several modeling assumptions that may contribute to the error in LEV

circulation. Most importantly, viscocity can play a significant role in situations where the vortex is close to the wing and viscous stresses are important. This could explain the large delay that experimental circulations have compared to the predictions. This could also play a role in the fact the delay increases with decreasing gust ratio. For lower gust ratios, the vortex is closer to the wing and has more interaction with the wing's boundary layers.

Another assumption that may contribute to the error of this procedure is that the parabola model remains accurate after separation. As the flow turns around the leading edge and separates, the effective curvature of the leading edge decreases. In other words, the separation streamline has lower curvature than the leading-edge. Deparday et al. [25] modeled these phenomenon by experimentally measuring the shear layer height and adjusting the effective radius of the leading edge. A potential improvement to the above procedure is accounting for the violation of this assumption.

6.3 Application III: Optimal gust mitigation kinematics

While previous sections use inviscid models to address challenges in gust measurement and prediction, this section addresses the related problem of gust mitigation. Specifically, it utilizes inviscid theory and an optimization procedure to derive optimal gust mitigation kinematics.

6.3.1 Iterative maneuver optimization

In this dissertation, optimality is defined as the L^2–norm of the lift transient. In other words, given some lift transient $C_L(t)$, and some target lift reference, $C_L^{ref}(t)$, the cost is,

$$J[u(t)] = \frac{1}{2}\int_{t_0}^{t_f} \left(C_L(t) - C_L^{ref}(t)\right)^2 dt \tag{6.23}$$

where the cost is written as a functional of the control action $u(t)$. For example, $u(t)$ can be the angle of attack or plunge amplitude history (or both) of the wing. The goal of the optimization problem is to find $u^*(t)$ that minimizes $J[u(t)]$.

Several studies have designed and tested gust mitigating controllers in experiment [48, 98]. However, it is typically not possible to compute optimal maneuvers due to the lack of accurate models of gust encounter dynamics. For example, Wagner's and Kussner's models can be used to construct and test an optimal alleviation maneuver. However, since both Wagner's and Kussner's models are based on linear aerodynamics, the generated maneuver is bound to perform non-optimally.

To bypass the shortcomings of available models, we use an iterative optimization technique called Simplified Iterative Maneuver Optimization (SIMO) to generate optimal maneuvers. This method was designed in [113] and has its roots in iterative control theory. The main idea of SIMO is to take an imperfect model of the dynamics, G, and iteratively account for its bias. It is advantageous to pick a model that incorporates the most important physics but is also simple enough to be used in an optimization routine. For these reasons, Theodorsen's inviscid model is chosen. The lift coefficient resulting from Theodorsen's model is,

$$C_L = \pi b \left(\frac{\dot{\alpha}}{U_\infty} + \frac{\ddot{h}}{U_\infty^2} - \frac{ba\,\ddot{\alpha}}{U_\infty^2} \right) + 2\pi C(k) \left[\frac{\dot{h}}{U_\infty} + \alpha + b\left(\frac{1}{2} - a\right) \frac{\dot{\alpha}}{U_\infty} \right] \tag{6.24}$$

The model takes in wing kinematics as input $(\alpha, \dot{\alpha}, \ddot{\alpha}, \dot{h}, \ddot{h})$, and outputs the lift coefficient transient of the wing. Thus, it is possible to compute an optimal maneuver based on this model if the gust lift transient is specified and the model is inverted to yield the kinematics which would cancel the gust transient. In this dissertation the model is inverted based on the procedure described in [113] which uses a PI controller to track the desired signal C_L^{ref} using kinematics u. The closed-loop controller is

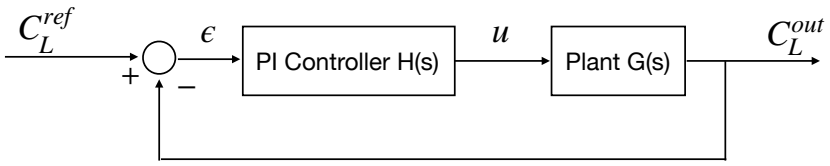

Figure 6.13: Depiction of controller $H(s)$ used to invert the plant $G(s)$.

shown in figure 6.13. The PI controller $H(s)$ gains are chosen as $K_p = 1.4$ and $K_i = 435.24$ based on MATLAB's **pidtune** function with 0dB open-loop crossover frequency of 50Hz.

The gust mitigation objective is to achieve 0 lift through the gust. Hence, the reference lift signal is $C_L^{ref} = 0$. The SIMO algorithm iteratively adjusts the reference signal, C_L^{ref}, to account for bias due to unmodeled dynamics. The algorithm is outlines below,

Algorithm 1 Simplified Iterative Maneuver Optimization

1: Initialize reference lift coefficient $C_{L,ref}^{(1)} = \mathbf{0}$
2: **while** $J[u^{(i)}] >$ tol **do**
3: Invert Theodorsen's model to find the kinematics $u^{(i)}$ that track $C_{L,ref}^{(i)}$.
4: Run experiment with kinematics $u^{(i)}$ and measure the gust lift transient $C_{L,test}^{(i)}$
5: Compute new reference lift coefficient as $C_{L,ref}^{(i+1)} = C_{L,ref}^{(i)} - C_{L,test}^{(i)}$
6: **end while**

The first two iterations are trivial. On the first iteration, the reference lift is $C_{L,ref}^{(1)} = 0$ and the kinematics retreived from inverting Theodorsen's model are $u^{(1)} = 0$. On the second iteration, the reference lift is $C_{L,ref}^{(2)} = -C_L^{gust}$, where C_L^{gust} is the transient induced by a gust encounter with no actuation. Theodorsen inversion in this case will result the kinematics profile required to cancel the gust transient using *potential flow dynamics*. Inevitably, the maneuver will cancel part of the transient

but not all. The key to the SIMO algorithm is then to adjust the lift reference, $C_{L,ref}^{(i)}$, to be the residual lift from the experiment. If the dynamics are linear the iteration is guaranteed to converge as discussed in [113], but for nonlinear dynamics there is no such guarantee. As will will see in the next section the algorithm works well for this flow.

6.3.2 Optimal kinematics

This section considers SIMO under pure pitch kinematics, ($\dot{h} = \ddot{h} = 0$). The actuation variable is the angle of attack, $u(t) = \alpha(t)$, and the procedure seeks to find the optimal angle of attack history, $\alpha^*(t)$, that minimizes the lift cost (6.23). Experiments are done at $GR = 0.7$ and $Re = 12000$.

Figure 6.14 summarizes the results of the optimization procedure. Five iterations were required before the procedure converged. Figure 6.14a depicts the lift transients for each iteration, figure 6.14b depicts the reference lift at its iteration, figure 6.14c depicts the angle of attack histories, and figure 6.14d depicts the pitch rate. In the initial iteration, the wing goes through the gust without any actuation. In the second iteration, the lift reference in figure 6.14b is the (negative) gust transient. In other words, Theodorsen's model is asked to produce an angle of attack history that cancels the gust transient. This results in a pitch-down pitch-up maneuver shown in figures 6.14c and 6.14d. The wing pitches down to approximately $-27°$ degrees and then back to small positive angle of attack. This results in the second iteration lift transient of figure 6.14a. While the maneuver achieved a significant reduction in lift, significant positive lift remained in the early phases of the gust encounter as well as the gust recovery region, while negative lift persisted in between. The reference lift update in figure 6.14b, reflects this trend and requires Theodorsen's model to track a more or

less aggressive transient depending on the residual lift. Significant reduction in lift takes place in the next few iterations until convergence at iteration five.

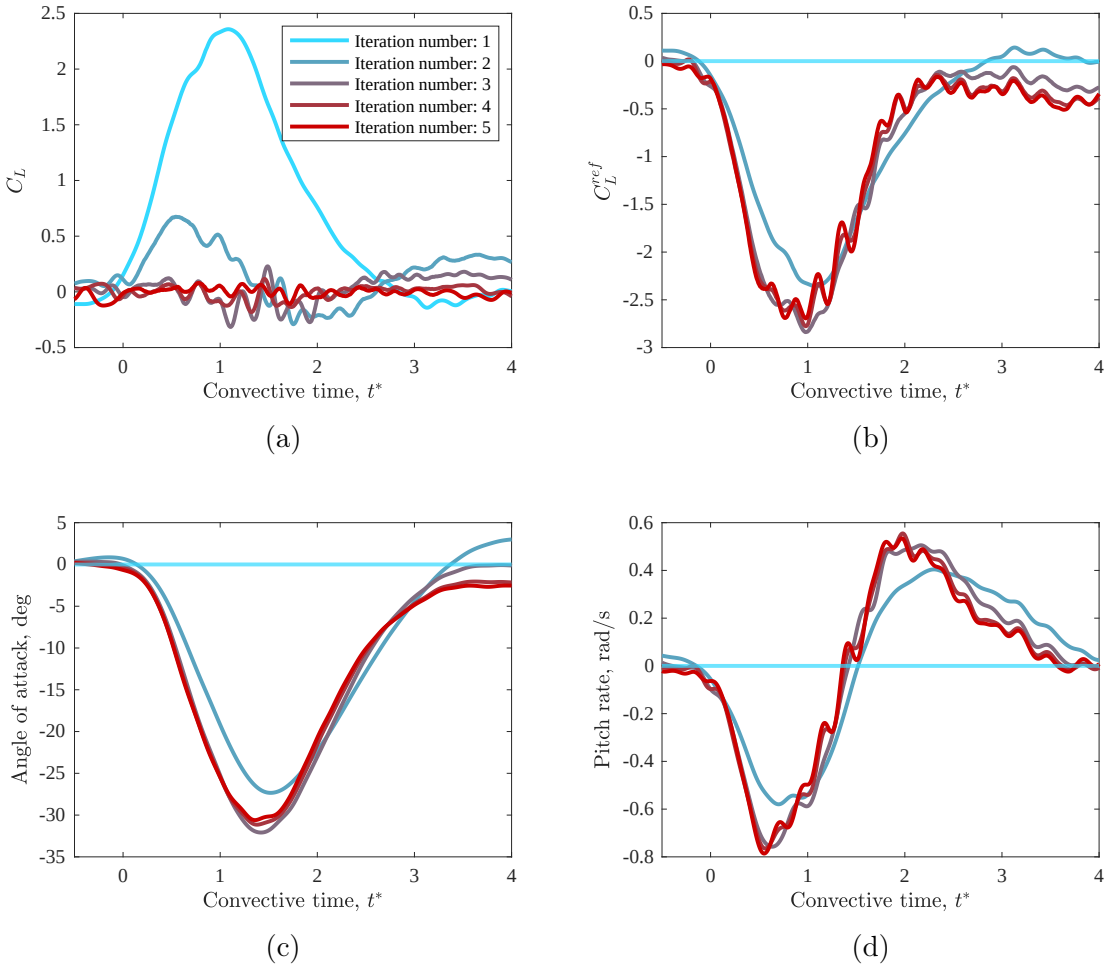

Figure 6.14: Generation of optimal gust mitigation pitch kinematics using the SIMO method.

An identical optimization procedure is carried for pure plunge kinematics ($\alpha = \dot{\alpha} = \ddot{\alpha} = 0$). The results are shown in figure 6.15. Again, the procedure converged to near optimal kinematics in five iterations. The optimal maneuver is an plunge up maneuver at approximately 90% of the gust velocity, as shown in figure 6.15d. Theodorsen's model is able reproduce a more effective maneuver on the second iteration. Effectively, the only part of the maneuver requiring more than two iterations

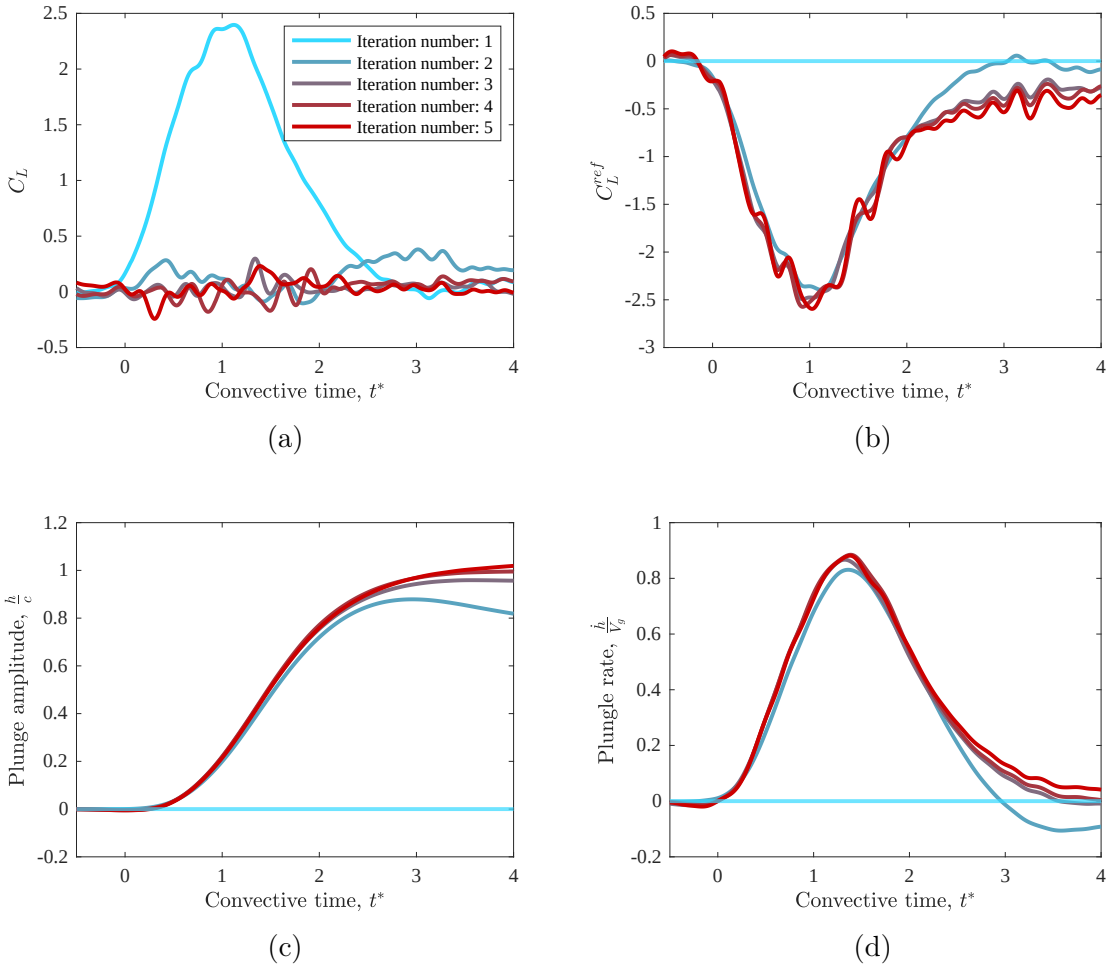

Figure 6.15: Generation of optimal gust mitigation plunge kinematics using the SIMO method.

is the gust exit.

By recovering the optimal pitch and plunge maneuvers, it is now possible to investigate what makes them aerodynamically optimal. Figure 6.16a depicts initial gust transient, the final reference lift coefficient, as well as the added mass and quasi-steady lift components of the final pitch maneuver. The difference between the gust transient and the final reference lift gives an estimate of the bias of Theodorsen's model in its prediction of negative lift generation in a gust. Initially, the reference lift coefficient is higher than the gust transient. This suggests that Theodorsen's linear

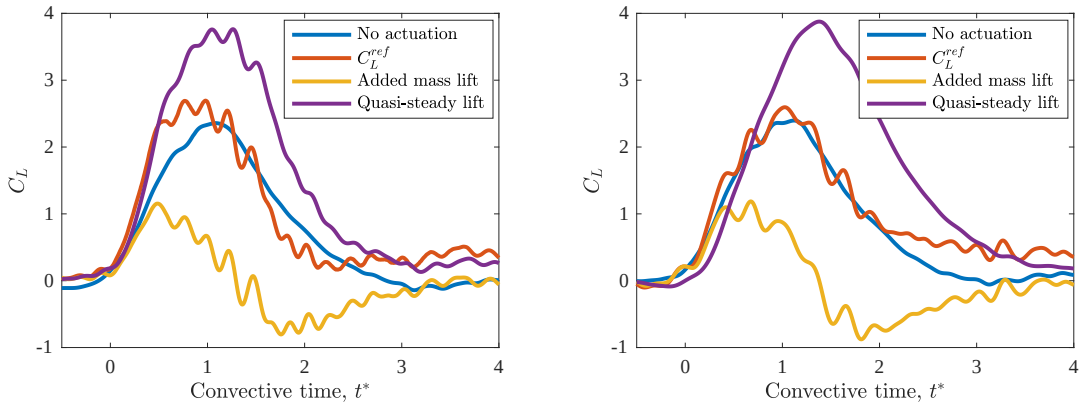

Figure 6.16: Lift decomposition for an optimal maneuver with (a) pitch kinematics, (b) plunge kinematics.

aerodynamics overpredict the amount of lift the wing can produce by pitching inside the gust. The trend reverses after the wing has entered the gust fully ($t^* > 1$) and then reverse again as the wing exits the gust. This highlights the nonlinear dynamics of highly vortical gust mitigation flows.

An important observation is that for the first 0.5 convective times of the gust encounter for both plunge and pitch maneuvers, most of the gust lift transient is canceled by added mass lift, as shown in figure 6.16. This is where typical gust mitigation controllers suffer in performance [48, 98]. Added mass lift responds to the commanded kinematics instantaneously. The SIMO procedure has demonstrated that the added mass effect is the key to effective gust mitigation early on in the gust.

6.4 Chapter summary

This chapter focuses on the development and application of three inviscid modeling methods to study the physics of separation and to develop effective flow sensing and control strategies. The first model is a numerical inviscid method that can compute

unsteady surface pressure distributions during gust encounters. The model is used to study the effects of separation on the unsteady pressure distribution during a gust encounter. It was shown that accounting for leading-edge separation and vortex formation affects both the suction side and pressure side pressures. In particular, the omission of separation resulted in consistent under-prediction of pressure on the pressure side of the wing. The inclusion of leading-edge separation recovered the pressures measured in experiment.

The second method is an an analytical model that relates the growth of a leading-edge vortex sheet to the pressure coefficient on the leading edge of a wing. The theory predicts that excess pressure beyond an empirically determined critical coefficient can be related to the formation of a leading-edge vortex sheet.

The third method discussed in this chapter is an iterative optimization procedure which experimentally determines optimal gust mitigation kinematic maneuvers. The pitch and plunge maneuvers computed were able to mitigate more than 95% of the lift transient during gust encounters. The Simplified Iterative Maneuver Optimization (SIMO), which was developed by Xu et al. [113], was employed to calculate these pitch and plunge maneuvers.

Chapter 7: Conclusions

This dissertation entails an experimental and theoretical investigation of gust encounter aerodynamics, and explores pathways to effective flow sensing and kinematic control during transverse gust encounters. Emphasis is placed on analyzing, extending, and utilizing the inviscid theory of unsteady aerodynamics, and on developing computationally inexpensive and analytically tractable models that provide physical insight into the aerodynamics of wing-gust encounters. The following sections include a summary of research, original contributions, and suggestions for future work.

7.1 Summary and conclusions

7.1.1 Role of shed vorticity in lift production

The first part of the dissertation investigates the role of vorticity distribution in the rise and fall of lift during transverse gust encounters. It also evaluates the effectiveness of indicial response methods, and particularly, Küssner's aerodynamic model, using PIV and load measurements. Emphasis is placed on comparing experimental lift transients and shed vorticity distributions with those predicted by the inviscid theory. The results show that Küssner's model provides a good first-order approximation of the lift transient experienced by wings with blunt leading edges during the initial stages of a transverse gust encounter.

The following concepts are applied to transverse gust encounters: (i) The notion

of optimal vortex formation time, and (ii) LEV growth prediction through the integration of shear layer fluxes. The timescale of optimal vortex formation is shown to be larger than the timescale of the gust encounters studied in this chapter. Thus, the LEV remains attached to the wing for the duration of the encounter and only detaches upon the wing's exit of the gust due to the rapid reduction of the effective angle of attack. The LEV flux model predicts that while the LEV is attached to the feeding shear layer, its circulation growth is proportional to $GR^2 + 1$ and area growth is proportional to $(GR^2 + 1)^{0.5}\ (a_0 c)^{-0.5}\ Re^{-0.5}$. For the gust ratios and Reynolds numbers examined in this chapter, fair agreement is seen between experiments and the flux model's predictions. The agreement deteriorates with increasing convective time. This could be attributed to the simplified calculation of the shear layer velocity made in the model, which only accounts for the gust vorticity. As the bound and LEV circulations become significant, they inevitably affect the shear layer velocity.

Comparison of the circulation shed in the wake of Küssner's model with the circulation shed in the wake during experiments leads to the following conclusion: Although the real viscous flow is separated, the bound circulation in Küssner's inviscid model captures the combined circulation of the bound vortex-LEV pair of the experiments, conditioned on an increasing quasi-steady circulation. This result, along with the fact that the vortex remains attached for the duration of the gust encounter, indicates that Küssner's model captures the vertical impulse of the separated flow. In other words, if the LEV is attached, its circulation can be incorporated as part of the bound circulation of the inviscid model, resulting in an accurate model for the lift during transverse gust encounters.

The performance of Küssner's model deteriorates once the quasi-steady circulation starts to decrease. This is because the lift-producing mechanisms between theory and experiment are fundamentally different, even though they produce similar values of

lift while the quasi-steady circulation is increasing. In the attached flow theoretical model, the positive circulation supplying the lift to the system is bound to the wing. In the real separated flow, the positive circulation supplying the lift is already shed and free to convect with the flow, while the bound circulation is in fact negative. Thus, when the quasi-steady circulation decreases in the model, the circulation shed into the wake from the trailing edge is positive and upwash inducing, while in the experiments it is negative and downwash inducing. The absence of upwash-inducing wake vorticity is the reason a much sharper lift drop-off is observed in experiments. In other words, the lift drop-off in the model is governed by delayed response to a (negative) change in its quasi-steady circulation, while in the experiments it is governed by the detachment of the LEV and the persistent shedding of negative circulation into the wake.

The above discussion presents a fundamental limitation on lift modeling using unsteady potential flow. *While potential flows might be able to capture the general circulatory characteristics of separated lifting flows, they can only do so while the quasi-steady circulation is increasing.* Once the quasi-steady circulation starts to decrease, the wake distribution will be of the wrong sign and the overall flow topology will be different. To improve lift prediction during the exit of the gust, the effect of the LEV on the bound circulation must be modelled. This can be done using a numerical vortex model that heuristically incorporates leading-edge separation.

7.1.2 Unsteady pressure distributions

The next part of the dissertation presented and analyzed simultaneous flowfield, load, and pressure distribution measurements of gust encounter flows. A surface pressure measurement wing model capable of simultaneous pressure and load measurements is developed and is validated using steady and unsteady test cases. The

validation study showed that sectional pressure integration can recover the overall wing loads for both steady and unsteady flows, given that the flow is attached at the leading edge and the spanwise load distributions are reasonably flat. For post-stall angles of attack, the pressure-integrated loads track the overall loads during the vortex formation stage of the dynamic stall process, i.e., while the lift is increasing, and undershoot the overall lift during the vortex separation stage, i.e., while the lift is decreasing. This phenomenon has direct implications for gust encounter pressure sensing and is reflected in the measured gust loads. The vortex remains attached for the duration of the gust encounters, and thus, the pressure integrated lift is able to capture the overall wing lift while the leading edge is inside the gust. However, as the wing exits the gust, the vortex detaches and sets in motion the aforementioned lift undershoot behavior.

Analysis of the transient flowfields and pressure distributions detailed the key events and flow structures associated with separation at the leading edge during a gust encounter. Initially, a suction peak develops, widens, and eventually splits into two distinct peaks. The first peak is associated with the acceleration of the flow around the leading edge and the second with the concentration of vorticity near the surface. Subsequently, the concentrated vorticity lifts off the surface and a coherent vortex forms. The timing of these events is found to be independent of gust ratio. The initial location of the secondary peak is also found to be independent of gust ratio and its strength is found to be proportional to the gusting flow dynamic pressure, i.e., $\mathrm{GR}^2 + 1$. After its formation, the vortex convects in the chordwise direction at a rate that is proportional to the gust ratio and the suction peak decays at a rate that is also proportional to gust ratio.

Flow sensing techniques for gust encounters were also investigated. Specifically, the behavior of the leading-edge suction coefficient and the leading-edge pressure

gradient were analyzed. The onset of stall was found to take place when the leading-edge suction reached an inflection point, i.e., when its growth rate began diminishing. Peak leading-edge suction was found to occur when the vorticity roll-up lifts off the surface. Subsequently, suction at the leading edge was found to decrease as the vortex begins its chordwise convection. The pressure gradient computed at the leading edge was found to contain useful signatures for each of the events during the gust encounter. The initiation of stall causes the pressure gradient to decrease. The formation of the secondary suction peak takes place when the pressure gradient crosses the x-axis, and the detachment of the vortex causes an increase in leading-edge pressure gradient. In contrast to the leading-edge suction, the variation of leading-edge pressure gradient between different gust ratios was found to be only a small percentage of the overall variation during a gust encounter. In other words, each case takes a similar pressure gradient trajectory through the gust encounter. Thus, the leading-edge pressure gradient can provide gust ratio invariant information to a gust alleviation controller.

7.1.3 Inviscid modeling applications

The last part of the dissertation focused on the application of inviscid modeling methods to study the physics of separation and to develop effective flow sensing and control strategies. A numerical inviscid method that can compute unsteady surface pressure distributions during gust encounters was developed and validated. The method was based on connected doublet and vortex sheets and solves the thin-airfoil problem on the wing camber line as well as the thick-airfoil problem on the wing's surface. The effects of two different gust models on the pressure distribution were investigated. It was shown that modeling the gust using rigid shear layers creates unrealistic surface gradients that induce erroneous pressure distributions, a charac-

teristic that can be avoided by modeling the gust using non-rigid shear layers. The model was used to study the effects of separation on the unsteady pressure distribution during a gust encounter. It was shown that *accounting for leading-edge separation and vortex formation affects both the suction side and pressure side pressures*. In particular, the omission of separation resulted in consistent under-prediction of pressure on the pressure side of the wing. The inclusion of leading-edge separation recovered the pressures measured in experiment.

An analytical model for the growth of the LEV as a function of the leading-edge pressure coefficient was developed and used to predict the growth of the LEV during gust encounters. In the theory, the wing is represented as a bound vortex sheet, which is connected to two free vortex sheets on either end to represent the leading and trailing edge shed vorticity distributions. The singularity at the sharp leading-edge of the bound vortex sheet is removed by asymptotically matching thin-airfoil theory to the potential flow over a parabola representing the leading-edge. This translates the critical leading-edge suction coefficient to a critical leading-edge pressure coefficient. The theory predicts that excess pressure beyond this critical coefficient is the result of the formation of a leading-edge vortex sheet. There is fair agreement between the experimental and predicted values. Notable shortcomings of the theory are its tendency to overestimate LEV circulation by $\approx 15\%$ while also predicting LEV formation and growth earlier than what is observed in experiments.

The last part of this dissertation experimentally determined optimal gust mitigation kinematic maneuvers. These maneuvers were able to mitigate more than 95% of the lift transient during gust encounters. The Simplified Iterative Maneuver Optimization (SIMO) was employed to calculate these pitch and plunge maneuvers. The procedure uses Theodorsen's model to track a reference lift coefficient, which is iteratively updated to account for bias and unmodeled dynamics. The procedure was

shown to correctly account for error in Theodorsen's model in various parts of the gust encounter. An important observation is that for the first 0.5 convective times of the gust encounter for both plunge and pitch maneuvers, most of the gust lift transient is canceled by added mass lift. Added mass lift responds to the commanded kinematics instantaneously. Thus, the SIMO procedure has demonstrated that the added mass effect is key to effective gust mitigation early on in the gust.

7.2 Original contributions

1. This work provides an improved understanding of the role of bound and shed vorticity distributions in the rise of fall of lift during transverse gust encounters. The lift and circulation production of wings encountering gusts were studied across different Reynolds numbers and gust ratios.

2. The success of Küssner's inviscid gust model in capturing the early lift transients of separated gust flows is explained on the basis of overall circulation production. A decomposition of lift into circulatory and non-circulatory components shows that the bound circulation in Küssner's model is approximately equal the sum of bound and LEV circulations in separated gust encounter flows. Küssner's over-prediction of lift during gust exit is shown to be due to the shedding of upwash-inducing wake vorticity – a characteristic not observed in experiments.

3. Novel surface pressure distribution measurements are presented for a variety of unsteady flows. The evolution of surface pressure on the leading edge provides insight into the key events leading to flow separation and vortex formation during a gust encounter. Specifically, the criticality of the suction and pressure gradient coefficients on the leading edge are investigated and shown to provide

key information into separation timing and evolution. Integration of surface pressure leads to an understanding of the effects of separation on loads estimation using pressure.

4. A low-order inviscid model that predicts unsteady surface pressure in LEV flows is developed and validated. This leads to an improved understanding of the effects of separation on unsteady surface pressure distributions. Notably, it is shown that proper separation modeling is required to recover the experimentally observed pressure side pressures.

5. Inviscid models are used to develop tools for flow sensing and gust mitigation control. A connected vortex sheet model is used to relate the pressure coefficient at the leading edge to the growth of the leading-edge vortex sheet, demonstrating that a single sensor can be used to recover first order estimates of the leading-edge vortex strength. Theodorsen's model is incorporated in iterative optimization procedure to compute the optimal gust mitigating kinematic maneuvers.

7.3 Suggestions for future work

The experiments conducted as well as the models developed as part of this dissertation have several limitations which can be addressed in future research.

1. This dissertation mainly develops and uses inviscid tools to achieve its objectives. In many cases, this provides inaccurate estimates of flow characteristics. For example, the surface pressure associated with secondary vorticity formation is poorly predicted in chapter 6. Further, the inviscid theory presented in section 6.2.3 overestimates the strength and formation time of the leading-

edge vortex. It would be an important contribution to include viscous-inviscid coupling in these estimates, which would likely improve the results.

2. The relation of surface pressure to leading-edge vortex strength was purely based on fluid mechanical considerations. An alternate route to vortex estimation is the theory of state estimation, developed by the control theory community. This method requires the derivation of an analytical observation equation which relates the vorticity field to the surface pressure distribution. This equation can then be inverted using principles from estimation theory. Unfortunately, Bernoulli's equation is not a satisfactory observation equation. This is because in unsteady flows, the strength of the bound vortex varies with time, and time varying vortices are not physically admissible in potential flows (see Helmholtz's theorems). This does not pose any difficulties in velocity and force computations, but it does for pressure as it requires the evaluation of the unsteady potential.

3. The SIMO procedure was shown to be successful in computing optimal gust mitigating maneuvers. These maneuvers were experimentally computed and implemented as open-loop controllers. A logical next step is to combine these results with the work of Sedky et al. [98], who developed and tested closed-loop mitigation controllers. One way to achieve this is to design and tune a controller which produces maneuvers similar to the optimal ones computed 6.3.2. These controllers should be designed with the knowledge obtained from studying the optimal maneuvers.

Bibliography

[1] James M Akkala and James HJ Buchholz. Vorticity transport mechanisms governing the development of leading-edge vortices. *Journal of Fluid Mechanics*, 829:512–537, 2017.

[2] Xuanhong An, David R Williams, Jeff D Eldredge, and Tim Colonius. Lift coefficient estimation for a rapidly pitching airfoil. *Experiments in Fluids*, 62: 1–12, 2021.

[3] John Anderson. *Fundamentals of Aerodynamics*. McGraw hill, 2011.

[4] John D Anderson Jr, Stephen Corda, and David M Van Wie. Numerical lifting line theory applied to drooped leading-edge wings below and above stall. *Journal of Aircraft*, 17(12):898–904, 1980.

[5] Ignacio Andreu-Angulo and Holger Babinsky. Mitigation of airfoil gust loads through pitch. *AIAA Journal*, 60(9):5273–5285, 2022.

[6] Ignacio Andreu-Angulo, Holger Babinsky, Hülya Biler, Girguis Sedky, and Anya R Jones. Effect of transverse gust velocity profiles. *AIAA Journal*, 58 (12):5123–5133, 2020.

[7] Holger Babinsky, Robbie J Stevens, Anya R Jones, Luis P Bernal, and Michael V Ol. Low order modelling of lift forces for unsteady pitching and surging wings. In *54th AIAA aerospace sciences meeting*, page 0290, 2016. doi: 10.2514/6.2016-0290.

[8] Camli Badrya, Hülya Biler, Anya R Jones, and James D Baeder. Effect of gust width on flat-plate response in large transverse gust. *AIAA Journal*, 59(1): 49–64, 2021.

[9] Camli Badrya, Anya R Jones, and James D Baeder. Unsteady aerodynamic response of a flat plate encountering large-amplitude sharp-edged gust. *AIAA Journal*, 60(3):1549–1564, 2022. doi: 10.2514/1.J060683.

[10] Yeon Sik Baik, Luis P Bernal, Kenneth Granlund, and Michael V Ol. Unsteady force generation and vortex dynamics of pitching and plunging aerofoils. *Journal of Fluid Mechanics*, 709:37–68, 2012.

[11] George Keith Batchelor. *An introduction to fluid dynamics*. Cambridge university press, 2000.

[12] RMH Beckwith and Holger Babinsky. Impulsively started flat plate flow. *Journal of aircraft*, 46(6):2186–2189, 2009.

[13] H Bergh and Hendrik Tijdeman. Theoretical and experimental results for the dynamic response of pressure measuring systems. 1965.

[14] Hülya Biler, Camli Badrya, and Anya R Jones. Experimental and computational investigation of transverse gust encounters. *AIAA Journal*, 57(11): 4608–4622, 2019.

[15] Hugh JA Bird, Kiran Ramesh, Shūji Ōtomo, and Ignazio Maria Viola. Usefulness of inviscid linear unsteady lifting-line theory for viscous large-amplitude problems. *AIAA Journal*, 60(2):598–609, 2022.

[16] Louis A Burelle, Wenchao Yang, Frieder Kaiser, and David E Rival. Exploring the signature of distributed pressure measurements on non-slender delta wings during axial and vertical gusts. *Physics of Fluids*, 32(11), 2020.

[17] Dashuai Chen, Frieder Kaiser, JiaCheng Hu, David E Rival, Kai Fukami, and Kunihiko Taira. Sparse pressure-based machine learning approach for aerodynamic loads estimation during gust encounters. *AIAA Journal*, 62(1):275–290, 2024.

[18] Simon J Corkery and Holger Babinsky. Force production mechanisms for a flat plate wing at low reynolds numbers. In *2018 AIAA Aerospace Sciences Meeting*, page 0816, 2018. doi: 10.2514/6.2018-0816.

[19] Simon J Corkery and Holger Babinsky. An investigation into gust shear layer vorticity and the added mass force for a transverse wing-gust encounter. In *AIAA Scitech 2019 Forum*, page 1145, 2019. doi: 10.2514/6.2019-1145.

[20] Simon James Corkery. *Unsteady aerodynamics of wing-gust encounters*. PhD thesis, University of Cambridge, 2019.

[21] SJ Corkery, H Babinsky, and JK Harvey. On the development and early observations from a towing tank-based transverse wing–gust encounter test rig. *Experiments in Fluids*, 59:1–16, 2018.

[22] SJ Corkery, Holger Babinsky, and WR Graham. Quantification of added-mass effects using particle image velocimetry data for a translating and rotating flat plate. *Journal of Fluid Mechanics*, 870:492–518, 2019. doi: 10.1017/jfm.2019.231.

[23] John O Dabiri. Optimal vortex formation as a unifying principle in biological propulsion. *Annual review of fluid mechanics*, 41:17–33, 2009. doi: 10.1146/annurev.fluid.010908.165232.

[24] Julien Deparday and Karen Mulleners. Modeling the interplay between the shear layer and leading edge suction during dynamic stall. *Physics of Fluids*, 31(10), 2019.

[25] Julien Deparday, Xiaowei He, Jeff D Eldredge, Karen Mulleners, and David R Williams. Experimental quantification of unsteady leading-edge flow separation. *Journal of Fluid Mechanics*, 941:A60, 2022.

[26] Adam C DeVoria and Kamran Mohseni. On the mechanism of high-incidence lift generation for steadily translating low-aspect-ratio wings. *Journal of Fluid Mechanics*, 813:110–126, 2017.

[27] Levi DeVries, Francis D Lagor, Hong Lei, Xiaobo Tan, and Derek A Paley. Distributed flow estimation and closed-loop control of an underwater vehicle with a multi-modal artificial lateral line. *Bioinspiration & biomimetics*, 10(2):025002, 2015.

[28] Norbert Didden. On the formation of vortex rings: rolling-up and production of circulation. *Zeitschrift für angewandte Mathematik und Physik ZAMP*, 30 (1):101–116, 1979. doi: 10.1007/BF01597484.

[29] Mark Drela. Xfoil: An analysis and design system for low reynolds number airfoils. In *Low Reynolds Number Aerodynamics: Proceedings of the Conference Notre Dame, Indiana, USA, 5–7 June 1989*, pages 1–12. Springer, 1989.

[30] Mark Drela. *Flight vehicle aerodynamics*. MIT press, 2014.

[31] Jeff D Eldredge. *Mathematical modeling of unsteady inviscid flows*, volume 50. Springer, 2019.

[32] Jeff D Eldredge and Anya R Jones. Leading-edge vortices: mechanics and modeling. *Annual Review of Fluid Mechanics*, 51(1):75–104, 2019.

[33] Jeff D Eldredge and Mathieu Le Provost. Bayesian inference of vorticity in unbounded flow from limited pressure measurements. *Journal of Fluid Mechanics*, 986:A18, 2024.

[34] Charles P Ellington. The aerodynamics of flapping animal flight. *American Zoologist*, 24(1):95–105, 1984. doi: 10.1093/icb/24.1.95.

[35] Brenden P Epps and Bernard T Roesler. Vortex sheet strength in the sears, küssner, theodorsen, and wagner aerodynamics problems. *AIAA Journal*, 56 (3):889–904, 2018. doi: 10.2514/1.J056399.

[36] Arthur Fage and FC Johansen. On the flow of air behind an inclined flat plate of infinite span. *Proceedings of the Royal Society of London. Series A, Containing Papers of a Mathematical and Physical Character*, 116(773):170–197, 1927. doi: 10.1098/rspa.1927.0130.

[37] CW Pitt Ford and Holger Babinsky. Lift and the leading-edge vortex. *Journal of fluid mechanics*, 720:280–313, 2013.

[38] Pascal Gehlert and Holger Babinsky. Linking the unsteady force generation to vorticity for a translating and rotating cylinder. In *AIAA Scitech 2019 Forum*, page 0347, 2019. doi: 10.2514/6.2019-0347.

[39] Pascal Gehlert and Holger Babinsky. Boundary layer vortex sheet evolution around an accelerating and rotating cylinder. *Journal of Fluid Mechanics*, 915, 2021. doi: 10.1017/jfm.2021.121.

[40] Pascal Gehlert and Holger Babinsky. Noncirculatory force on a finite thickness body encountering a gust. *AIAA Journal*, 59(2):719–730, 2021. doi: 10.2514/1.J059686.

[41] Antonios Gementzopoulos, Girguis Sedky, and Anya Jones. Role of vorticity distribution in the rise and fall of lift during a transverse gust encounter. *Physical Review Fluids*, 9(1):014701, 2024.

[42] Morteza Gharib, Edmond Rambod, and Karim Shariff. A universal time scale for vortex ring formation. *Journal of Fluid Mechanics*, 360:121–140, 1998. doi: 10.1017/S0022112097008410.

[43] Daniel F Gomez, Francis D Lagor, Phillip B Kirk, Andrew H Lind, Anya R Jones, and Derek A Paley. Data-driven estimation of the unsteady flowfield near an actuated airfoil. *Journal of Guidance, Control, and Dynamics*, 42(10): 2279–2287, 2019.

[44] Laurent Graftieaux, Marc Michard, and Nathalie Grosjean. Combining piv, pod and vortex identification algorithms for the study of unsteady turbulent swirling flows. *Measurement Science and technology*, 12:1422, 2001.

[45] Amanda L Grubb, Alex Moushegian, Daniel J Heathcote, and Marilyn J Smith. Physics and computational modeling of nonlinear transverse gust encounters. In *AIAA Scitech 2020 Forum*, page 0080, 2020. doi: 10.2514/6.2020-0080.

[46] Guosheng He, Julien Deparday, Lars Siegel, Arne Henning, and Karen Mulleners. Stall delay and leading-edge suction for a pitching airfoil with trailing-edge flap. *AIAA Journal*, 58(12):5146–5155, 2020.

[47] Xiaowei He and David R Williams. Pressure feedback control of aerodynamic loads on a delta wing in transverse gusts. *AIAA Journal*, 61(4):1659–1674, 2023.

[48] Benjamin Herrmann, Steven L Brunton, Johannes E Pohl, and Richard Semaan. Gust mitigation through closed-loop control. ii. feedforward and feedback control. *Physical Review Fluids*, 7(2):024706, 2022.

[49] Karl Hiemenz. Die grenzschicht an einem in den gleichformigen flussigkeitsstrom eingetauchten geraden kreiszylinder. *Dinglers Polytech. J.*, 326:321–324, 1911.

[50] Marvin Jentzsch, H J Schmidt, René Woszidlo, Christian Navid Nayeri, and Christian Oliver Paschereit. Challenges and procedures for experiments with steady and unsteady model velocities in a water towing tank. *Experiments in Fluids*, 62:1–20, 2021.

[51] Anya R Jones, Oksan Cetiner, and Marilyn J Smith. Physics and modeling of large flow disturbances: Discrete gust encounters for modern air vehicles. *Annual Review of Fluid Mechanics*, 54, 2021.

[52] Anya R Jones, Oksan Cetiner, and Marilyn J Smith. Physics and modeling of large flow disturbances: discrete gust encounters for modern air vehicles. *Annual Review of Fluid Mechanics*, 54:469–493, 2022.

[53] Robert Thomas Jones. *Classical aerodynamic theory*. Number 1050. National Aeronautics and Space Administration, 1979.

[54] Chang-kwon Kang, Yeon Baik, Luis Bernal, Michael Ol, and Wei Shyy. Fluid dynamics of pitching and plunging airfoils of reynolds number between $1\times 10\hat{}\ 4$ and $6\times 10\hat{}\ 4$. In *47th AIAA aerospace sciences meeting including the new horizons forum and aerospace exposition*, page 536, 2009. doi: 10.2514/6.2009-536.

[55] Joseph Katz and Allen Plotkin. *Low-speed aerodynamics*, volume 13. Cambridge university press, 2001.

[56] Philip B Kirk and Anya R Jones. Vortex formation on surging aerofoils with application to reverse flow modelling. *Journal of fluid mechanics*, 859:59–88, 2019.

[57] Johannes Kissing, Jochen Kriegseis, Zhenyao Li, Lihao Feng, Jeanette Hussong, and Cameron Tropea. Insights into leading edge vortex formation and detachment on a pitching and plunging flat plate. *Experiments in Fluids*, 61(9):1–18, 2020. doi: 10.1007/s00348-020-03034-1.

[58] Max Kramer. Increase in the maximum lift of an airplane wing due to a sudden increase in its effective angle of attack resulting from a gust. Technical report, 1932.

[59] Herbert G Küssner. Zusammenfassender bericht über den instationären auftrieb von flügeln. *Luftfahrtforschung*, 13(12):410–424, 1936.

[60] Francis D Lagor, Levi D DeVries, Kathryn M Waychoff, and Derek A Paley. Bio-inspired flow sensing and control: Autonomous rheotaxis using distributed pressure measurements. *Journal of Unmanned System Technology*, 1(3):78–88, 2013.

[61] Horace Lamb. *Hydrodynamics*. University Press, 1924.

[62] Sébastien Le Fouest and Karen Mulleners. The dynamic stall dilemma for vertical-axis wind turbines. *Renewable Energy*, 198:505–520, 2022.

[63] Sébastien Le Fouest and Karen Mulleners. Optimal blade pitch control for enhanced vertical-axis wind turbine performance. *Nature Communications*, 15 (1):2770, 2024.

[64] Sébastien Le Fouest, Julien Deparday, and Karen Mulleners. The dynamics and timescales of static stall. *Journal of Fluids and Structures*, 104:103304, 2021. doi: 10.1016/j.jfluidstructs.2021.103304.

[65] Gordon J Leishman. *Principles of helicopter aerodynamics*. Cambridge university press, 2006.

[66] James Lighthill. An informal introduction to theoretical fluid mechanics. 1986.

[67] MJ Lighthill. A new approach to thin aerofoil theory. *Aeronautical Quarterly*, 3(3):193–210, 1951.

[68] Eric Limacher, Chris Morton, and David Wood. Generalized derivation of the added-mass and circulatory forces for viscous flows. *Physical Review Fluids*, 3 (1):014701, 2018. doi: 10.1103/PhysRevFluids.3.014701.

[69] Ethan Loewenthal and Ashok Gopalarathnam. Low-order modeling of wingtip vortices in a vortex lattice method. *AIAA Journal*, 60(3):1708–1720, 2022.

[70] Field Manar and Anya R Jones. Evaluation of potential flow models for unsteady separated flow with respect to experimental data. *Physical Review Fluids*, 4(3):034702, 2019. doi: 10.1103/PhysRevFluids.4.034702.

[71] Peter Mancini, Field Manar, Kenneth Granlund, Michael V Ol, and Anya R Jones. Unsteady aerodynamic characteristics of a translating rigid wing at low reynolds number. *Physics of Fluids*, 27(12), 2015.

[72] Peter Mancini, Albert Medina, and Anya R Jones. Experimental and analytical investigation into lift prediction on large trailing edge flaps. *Physics of Fluids*, 31(1):013106, 2019. doi: 10.1063/1.5063265.

[73] Barnes W McCormick. *Aerodynamics, aeronautics, and flight mechanics*. John Wiley & Sons, 1994.

[74] William J McCroskey. Unsteady airfoils. *Annual review of fluid mechanics*, 14 (1):285–311, 1982. doi: 10.1146/annurev.fl.14.010182.001441.

[75] JCPJ Morgado, R Vizinho, MAR Silvestre, and JC Páscoa. Xfoil vs cfd performance predictions for high lift low reynolds number airfoils. *Aerospace Science and Technology*, 52:207–214, 2016.

[76] Bruce R Morton. The generation and decay of vorticity. *Geophysical & Astrophysical Fluid Dynamics*, 28(3-4):277–308, 1984.

[77] Karen Mulleners and Markus Raffel. The onset of dynamic stall revisited. *Experiments in fluids*, 52:779–793, 2012.

[78] Karen Mulleners and Markus Raffel. Dynamic stall development. *Experiments in fluids*, 54:1–9, 2013.

[79] Shreyas Narsipur, Pranav Hosangadi, Ashok Gopalarathnam, and Jack R Edwards. Variation of leading-edge suction during stall for unsteady aerofoil motions. *Journal of Fluid Mechanics*, 900:A25, 2020.

[80] Robert L Nudds, Graham K Taylor, and Adrian LR Thomas. Tuning of strouhal number for high propulsive efficiency accurately predicts how wingbeat frequency and stroke amplitude relate and scale with size and flight speed in birds. *Proceedings of the Royal Society of London. Series B: Biological Sciences*, 271 (1552):2071–2076, 2004.

[81] Michael V Ol, Luis Bernal, Chang-Kwon Kang, and Wei Shyy. Shallow and deep dynamic stall for flapping low reynolds number airfoils. In *Animal Locomotion*, pages 321–339. Springer, 2010. doi: 10.1007/s00348-009-0660-3.

[82] Shūji Ōtomo, Sabrina Henne, Karen Mulleners, Kiran Ramesh, and Ignazio Maria Viola. Unsteady lift on a high-amplitude pitching aerofoil. *Experiments in Fluids*, 62(1):1–18, 2021. doi: 10.1007/s00348-020-03095-2.

[83] Gino Perrotta and Anya R Jones. Unsteady forcing on a flat-plate wing in large transverse gusts. *Experiments in Fluids*, 58:1–11, 2017.

[84] Delyle T Polet, David E Rival, and Gabriel D Weymouth. Unsteady dynamics of rapid perching manoeuvres. *Journal of Fluid Mechanics*, 767:323–341, 2015. doi: 10.1017/jfm.2015.61.

[85] Naresh Poudel, Meilin Yu, and John T Hrynuk. Gust mitigation with an oscillating airfoil at low reynolds number. *Physics of Fluids*, 33(10), 2021.

[86] Ludwig Prandtl. Über flussigkeitsbewegung bei sehr kleiner reibung. *Verhandl. III, Internat. Math.-Kong., Heidelberg, Teubner, Leipzig, 1904*, pages 484–491, 1904.

[87] Kiran Ramesh. On the leading-edge suction and stagnation-point location in unsteady flows past thin aerofoils. *Journal of Fluid Mechanics*, 886:A13, 2020.

[88] Kiran Ramesh, Ashok Gopalarathnam, Kenneth Granlund, Michael V Ol, and Jack R Edwards. Discrete-vortex method with novel shedding criterion for unsteady aerofoil flows with intermittent leading-edge vortex shedding. *Journal of Fluid Mechanics*, 751:500–538, 2014.

[89] David Rival, Roland Manejev, and Cam Tropea. Measurement of parallel blade–vortex interaction at low reynolds numbers. *Experiments in Fluids*, 49(1):89–99, 2010. doi: 10.1007/s00348-009-0796-1.

[90] David E Rival, Jochen Kriegseis, Pascal Schaub, Alexander Widmann, and Cameron Tropea. Characteristic length scales for vortex detachment on plunging profiles with varying leading-edge geometry. *Experiments in fluids*, 55:1–8, 2014.

[91] Philip G Saffman. *Vortex dynamics*. Cambridge university press, 1995. doi: 10.1017/CBO9780511624063.

[92] Pooria Sattari, David E Rival, Robert J Martinuzzi, and Cameron Tropea. Growth and separation of a start-up vortex from a two-dimensional shear layer. *Physics of Fluids*, 24(10):107102, 2012. doi: 10.1063/1.4758793.

[93] Herrmann Schlichting and Klaus Gersten. *Boundary-layer theory*. Springer Science & Business Media, 2003.

[94] Andrea Sciacchitano and Bernhard Wieneke. Piv uncertainty propagation. *Measurement Science and Technology*, 27(8):084006, 2016. doi: 10.1088/0957-0233/27/8/084006.

[95] Girguis Sedky, Anya R. Jones, and Francis D. Lagor. Lift regulation during transverse gust encounters using a modified goman–khrabrov model. *AIAA Journal*, 58(9):3788–3798, apr 2020. ISSN 00011452. doi: 10.2514/1.J059127. URL `https://arc.aiaa.org/doi/abs/10.2514/1.J059127`.

[96] Girguis Sedky, Hülya Biler, and Anya R Jones. Experimental comparison of a sinusoidal and trapezoidal transverse gust. *AIAA Journal*, 60(5):3347–3351, 2022. doi: 10.2514/1.J061365.

[97] Girguis Sedky, Antonios Gementzopoulos, Ignacio Andreu-Angulo, Francis D Lagor, and Anya R Jones. Physics of gust response mitigation in open-loop pitching manoeuvres. *Journal of Fluid Mechanics*, 944:A38, 2022.

[98] Girguis Sedky, Antonios Gementzopoulos, Francis D Lagor, and Anya R Jones. Experimental mitigation of large-amplitude transverse gusts via closed-loop pitch control. *Physical Review Fluids*, 8(6):064701, 2023.

[99] PRRJ Stevens and Holger Babinsky. Experiments to investigate lift production mechanisms on pitching flat plates. *Experiments in Fluids*, 58(1):1–17, 2017.

[100] Arun Vishnu Suresh Babu, Shreyas Narsipur, and Ashok Gopalarathnam. Lift tailoring on unsteady airfoils with leading-edge vortex shedding using an inverse aerodynamic approach. *Physics of Fluids*, 36(5), 2024.

[101] ArunVishnu SureshBabu, Albert Medina, Matthew Rockwood, Matthew Bryant, and Ashok Gopalarathnam. Theoretical and experimental investigation of an unsteady airfoil in the presence of external flow disturbances. *Journal of Fluid Mechanics*, 921:A21, 2021.

[102] Theodore Theodorsen. General theory of aerodynamic instability and the mechanism of flutter. Technical report, 1949.

[103] William Thomson. Vi.—on vortex motion. *Earth and Environmental Science Transactions of the Royal Society of Edinburgh*, 25(1):217–260, 1868.

[104] Milton Van Dyke. Perturbation methods in fluid mechanics/annotated edition. *NASA STI/Recon Technical Report A*, 75:46926, 1975.

[105] Th H von Karman and William R Sears. Airfoil theory for non-uniform motion. *Journal of the Aeronautical Sciences*, 5(10):379–390, 1938.

[106] Herbert Wagner. Über die entstehung des dynamischen auftriebes von tragflügeln. 1924.

[107] PB Walker. Growth of circulation about a wing and an apparatus for measuring fluid motion. *ARC report*, 1931.

[108] A Widmann and C Tropea. Parameters influencing vortex growth and detachment on unsteady aerodynamic profiles. *Journal of Fluid Mechanics*, 773: 432–459, 2015. doi: 10.1017/jfm.2015.259.

[109] Bernhard Wieneke. Piv uncertainty quantification from correlation statistics. *Measurement Science and Technology*, 26(7):074002, 2015. doi: 10.1088/0957-0233/26/7/074002.

[110] Jaime G Wong and David E Rival. Determining the relative stability of leading-edge vortices on nominally two-dimensional flapping profiles. *Journal of Fluid Mechanics*, 766:611–625, 2015. doi: 10.1017/jfm.2015.39.

[111] James C Wu. Theory for aerodynamic force and moment in viscous flows. *AIAA Journal*, 19(4):432–441, 1981. doi: 10.2514/3.50966.

[112] Z Wu, Y Cao, and M Ismail. Gust loads on aircraft. *The Aeronautical Journal*, 123(1266):1216–1274, aug 2019.

[113] Xianzhang Xu, Antonios Gementzopoulos, Girguis Sedky, Anya R Jones, and Francis D Lagor. Design of optimal wing maneuvers in a transverse gust encounter through iterated simulation or experiment. *Theoretical and Computational Fluid Dynamics*, 37(4):465–484, 2023.